# HYBRID NANOPLASMONIC-NANOPHOTONIC DEVICES FOR ON-CHIP BIOCHEMICAL SENSING AND SPECTROSCOPY

A Thesis
Presented to
The Academic Faculty

by

Maysamreza Chamanzar

In Partial Fulfillment
of the Requirements for the Degree
Doctor of Philosophy in
Electrical and Computer Engineering

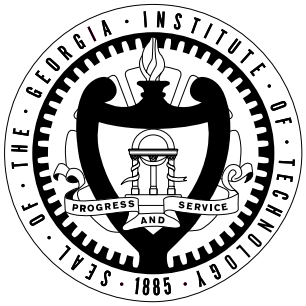


Georgia Institute of Technology
December 2012

# HYBRID NANOPLASMONIC-NANOPHOTONIC DEVICES FOR ON-CHIP BIOCHEMICAL SENSING AND SPECTROSCOPY

Approved by:

Professor Ali Adibi, Advisor

*Georgia Institute of Technology*

Professor Stephen E. Ralph

*Georgia Institute of Technology*

Professor John A. Buck

*Georgia Institute of Technology*

Professor Oliver Brand

*Georgia Institute of Technology*

Professor Mostafa A. El-Sayed

*Georgia Institute of Technology*

Date Approved: 17 Aug 2012

*To my wife, Zainab, for all her love and support.*

*To my parents, for their true love.*

# ACKNOWLEDGEMENTS

I would like to thank Prof. Ali Adibi for his support, guidance, and encouragement throughout my Ph.D. research and for providing me with the freedom to explore my ideas and research interests. I have learned a lot from his benevolence and vigorous attitude. I would also like thank his family for their great hospitality.

I am very grateful to my Ph.D. committee, Professor Stephen E. Ralph, Professor John A. Buck, Professor Oliver Brand, and Professor Mostafa A. El-Sayed, for their dedication and all the invaluable things that I have learned from them.

I am very thankful of Prof. Mostafa A. El-Sayed for providing me the opportunity to carry out part of my research in collaboration with his group at the laser dynamics laboratory (LDL) in the school of chemistry and biochemistry. I am very delighted that I could have worked with great scholars at LDL, including Dr. Mahmoud A. Mahmoud. He is a knowledgeable scientist, and a caring and kind friend. He was very patient to let me try my ideas freely in a chemistry lab, without being a chemist by education. I enjoyed endless scientific discussions with him, and I hope to continue collaborating with him.

I would like to thank great scholars at Georgia Tech, from whom I have learned a great deal about science and engineering, and they have served as a source of encouragement and inspiration for me. Specially, I would like to thank Professor Glen Smith, Professor Thomas Gaylord, Professor Jennifer Curtis, Professor Rick Trebino, and Professor Alex Kuzmich.

During the course of this endeavor, I had the opportunity to be mentored by Dr. Siva Yegnanarayanan. I am very grateful for all the valuable things in my research

and my life that I have learned from him.

I would like to extend my gratitude to my friends, Dr. Babak Momeni and Dr. Mohammad Soltani for all the useful discussions and helpful collaborations that we have had together. I have learned a lot from them, specially on how to have dedication to my research and academic pursuits.

During my research at Georgia , I have learned how to effectively collaborate with other researchers to carry out different aspects of a project. I have had the opportunity to collaborate with talented people such as Ye lou, Zhixuan Xia, Dr. Murtaza Askari, Dr. Ehsan Shah Hosseini, Farshid Ghasemi, Qing Li, Reza Abbaspour, Dr. Charles C. Camp, and Dr. Jie Xu. I am very thankful of all their helps and contributions.

I would like to thank Dr. Arash Karbaschi and Dr. Chaoray Hsieh for always being there to help. They are very knowledgeable experts in optics, specially in experimental aspects of it.

Working in the Georgia Tech Nanotechnology Research Center (NRC) cleanroom facilities has been an exceptional opportunity for me to be able to make my devices. I sincerely thank the NRC staff, specially Gary Spinner, Devin Brown, Eric Woods, Tran-Vinh Nguyen, Walter Henderson, and Charlie Suh. They have always been welcoming and ready to help. I would also like to particularly thank Devin Brown, the head of nanolithography facilities, for always being patient to help with the details of the fabrication processes that I have developed. I am very grateful that I could have found nice friends among dedicated researchers working at NRC, specially Ian, Jeremy, Jenna, Jamie, Amir, Roozbeh, and late Ashish, without whom the endless hours of working in the cleanroom would have not been that pleasant.

I am very thankful of Dr. Saeed Mohammadi, my best friend and colleague for always being there to help and support. I have spent the joyful moments of my time at Georgia Tech with him. I am also very grateful to have caring friends such

as Dr. Majid Badie and Dr. Amir Atabaki for their support and helpful advices.

I would also like to acknowledge the former and the current members of the photonic research group at Georgia Tech, specially Omid, Saman, Fengtao, Pouyan, Reza, James, Hossein, Majid, Reza, Hesam, Hamed, Amirhossein, Ali Behrooz, Ali Hashmi, Charles, Mehdi, and Payam.

Life has become very pleasant during my stay at Georgia Tech, specially when I found incredibly nice friends with whom I have spent the joyful moments of my life outside the lab environment. I would like to thank all of them specially Sam, Kevin, Hossein, Hamidreza, Saeed, Javad, Esmaeil, Hadi, Mojtaba, Mehdi, Ehsan, Hamid, and Parsa.

I started my research in Optics, when I carried out my M.Sc. studies in Professor Bizhan Rashidian's group in Sharif University. I am very thankful of him and all the exceptionally talented people that I met during my stay in his lab, specially Dr. Sina Khorasani and Dr. Khashayar Mehrany.

I would like to thank Georgia Tech staff members Rod Sefton and Paul Turgeon for always being supportive.

I am very thankful of Hossein, Zhixuan, Farshid, Qing, and Reza Abbaspour for carefully reviewing and proofreading my thesis chapters.

I would like to express my sincere gratitude to my wife, Zainab for all her unwavering love and support. She came to my life just before the onset of my graduate studies, and her patience, support, and wisdom have made this long journey very pleasant for me.

Last but certainly not least, I am very grateful of my family, specially my parents and my sister, Zahra, and my brother, Alireza for all their support and encouragement. I owe my success to my parents for their wholehearted and sincere support and encouragements throughout my life.

Hereby, I would like to dedicate this dissertation to my wife, and to my parents.

# TABLE OF CONTENTS

# LIST OF TABLES

# LIST OF FIGURES

# SUMMARY

Optical molecular sensing, being a non-invasive interrogation method to probe molecular-level interactions, has found intriguing applications in biosensing for diagnostics and therapeutics, and also in chemical sensing to detect chemical species and their interactions. Efficient optical sensing requires strong light-matter interaction. Plasmonic nanostructures can localize light in very small scales, resulting in ultra-high light intensities suitable for molecular-level light-matter interaction. Plasmonic nanoresonators synthesized in different shapes and different material platforms have been widely used in different sensing scenarios such as localized surface plasmon resonance (LSPR) sensing and surface enhanced Raman scattering (SERS) spectroscopy due to their ultra-high sensitivities and very high field enhancements. Surface plasmon polaritons have also been employed for molecular interactions detection, and real-time monitoring of binding kinetics. Although the very small mode volume of plasmonic structures makes them suitable for efficient interaction with molecules, it hinders efficient coupling of light from free-space to their localized modes. On the other hand, the recent advances in nanotechnology has enabled the realization of miniaturized on-chip integrated photonic structures in high-index-contrast material platforms such as silicon on insulator (SOI) and silicon nitride on insulator to guide and trap light. Integrated photonic waveguides can be used to steer light on a chip with minimal loss; and photonic microresonators with their ultra-high quality factors ($Q$) can be used to trap and enhance light on the chip. Despite their low propagation losses and ultra-high $Q$s, integrated photonic waveguides and microresonators have large mode volumes compared to the size scales required to obtain molecular specific information.

In this dissertation, I present the design, implementation, and experimental

demonstration of hybrid plasmonic-photonic structures for lab-on-chip biochemical sensing applications. Novel plasmonic nanostructures and integrated photonic structures are combined in the hybrid architecture to bring about unique performance advantages for efficient on-chip sensing. The hybrid plasmonic-photonic platform benefits from the best features of integrated photonic platform such as the low propagation loss, ultra-high $Q$ modes, and robustness, as well as the advantages of nanoplasmonics such as extreme light localization, large sensitivities, and ultra-high field enhancements. I discuss the developed semi-analytical models and simulation tools to design and analyze such hybrid plasmonic-photonic structures. The design goal is to achieve robust, highly efficient, and high-throughput devices for on-chip biochemical sensing. The sensing scenarios of interest are label-free refractive index sensing and SERS. I present the developed nanofabrication processes to realize these hybrid plasmonic-photonic structures. Since the desired sensing scenarios are best carried out in the visible and the near infrared range of spectrum, silicon nitride ($Si_3N_4$) is used as the material platform to realize the integrated photonic structures, and gold is used to realize plasmonic nanostructures. Furthermore, I discuss the designed and implemented optical characterization setups to test the performance of these hybrid structures. The integration of the hybrid plasmonic-photonic structures with microfluidics is also discussed, where the performance of the developed sensors to detect different analytes is demonstrated. The hybrid plasmonic-photonic structures developed in this research can open up new potentials for biochemical sensors with advanced on-chip functionalities and enhanced performances.

# CHAPTER I

# INTRODUCTION

In this chapter, the importance of light-matter interaction for molecular sensing applications will be discussed. Then the progress in developing lab-on-a-chip systems and the pertinent requirements, challenges, and state of the art will be reviewed. A brief description of plasmonic and photonic integrated devices along with their properties will follow. The advantages and the shortcomings of plasmonic and also photonic platforms will be reviewed. Finally, a review of the recent research progress in combining plasmonics and photonics will be discussed. The need for implementing a hybrid plasmonic-photonic platform for enhanced light-matter interaction on a chip is revealed in this chapter.

## *1.1 Optical Molecular Sensing*

Optical sensing is a non-invasive method that has been used for detection of molecular signatures through the change of refractive index [1], absorption [2], an inelastic scattering, or a nonlinear process such as Raman scattering [3] or fluorescence emission [4]. High-throughput optical sensing is a critical emerging technology in biology and environmental studies, which impacts several key scientific and technical research areas such as understanding of biomolecule fine structures, early cancer detection and treatment, study of biological system dynamics, drug screening, veterinary testing and diagnostics, environmental and agricultural testing, and enhanced bioremediation [5–8]. Generally, molecular sensing can be categorized into labeling techniques and label-free techniques. Labeling strategies involve a variety of schemes including electrochemical changes

[9], enzymatic transformation [10], fluorescence [11, 12], chemiluminescence [13], or quantum dot biolabeling [14]. Most labeling detection schemes have synthetic challenges, multiple label issues, may exhibit interference with the binding site, and involve long sample preparation times. Label-free optical detection techniques can be carried out using different schemes such as refractive index sensing [15], surface enhanced Raman spectroscopy (SERS) [3], and absorption sensing [2]. Such label-free methods can reduce complexity and increase accuracy of molecular sensing. These methods do not involve the tedious preparation process for labeling the molecules and make the sensing process fast and simple. Development of sensitive, reliable, and high-throughput label-free optical sensing schemes is a subject of recent research.

The principle of operation of index sensing is based on the detection of small refractive index changes caused by target molecules through detection of a phase change or a resonance shift. Different devices have been used to implement label-free optical refractive index sensing, such as surface plasmon resonance (SPR) sensors [16], photonic waveguide and fiber-based sensors [17, 18], photonic traveling-wave resonator sensors [19, 20], and photonic crystal resonance based sensors [21]. Each of these devices is best suited for a particular set of applications. SPR-based sensors have been widely used for label-free biomolecule refractive index sensing with detection limits of about $10^{-6} - 10^{-8} RIU$ [16, 22] , where $RIU$ stands for refractive index unit. Surface plasmon wave is formed through coherent oscillations of free electrons at a metal-dielectric interface. The electromagnetic energy of a surface plasmon polariton (SPP) mode is highly confined at the metal-dielectric interface. Thus, these modes are very sensitive to the refractive index changes of the dielectric medium. However, conventional SPR sensor systems are usually large and bulky since the excitation and interrogation is usually done through prism coupling and angle interrogation [16, 22]. There have been

some efforts to excite SPRs through coupling from a photonic planar waveguide [23] or fiber optics [24]. The waveguide-based SPR sensors can be interrogated through monitoring the transmittance spectrum [23], or through monitoring the coupling spectrum [25]. The fiber based SPR sensors are formed typically by side polishing the fiber to remove the fiber cladding and depositing a thin metallic layer. This type of structure suffers from cross-polarization interference, and different techniques have been introduced to alleviate this problem [24]. The photonic resonator-based sensors operate based on the spectral shift of high-Q resonance features with the adsorption of target molecules. These refractive index sensors have usually narrow resonance lineshapes, and they can provide extremely small detection limits. Practical implementation of such structures is a subject of an ongoing research, and there are some challenges that yet need to be addressed, such as high sensitivity to temperature changes and fabrication imperfections. Refractive index sensing inherently lacks specificity since different target molecules that cause the same index change cannot be distinguished. To address this issue, specific surface coatings consisting of different receptor molecules such as antibodies, glycans, oligonucleotides, aptamers, and phages are immobilized on the sensor surface so that the target molecules of interest specifically bind to the sensor surface [1, 16].

SERS is a sensing technique with high specificity, which reveals the Raman signature of molecules [3]. In this sensing scheme,the localized surface plasmon resonance (LSPR) of plasmonic nanostructures is used for enhancing the Raman signal emission. SERS has been used for detection of different pathogens such as viruses and bacteria [26], where the power of this sensing method for distinguishing different virus types has been demonstrated [27]. SERS has also been used to detect different conformational states of $\beta$-Amyloid peptide [28], which helps with the understanding and diagnosing of Alzheimer disease. This method has also

been used in differentiating cancer cells from normal cells [29]. SERS is sensitive to molecules orientations and the distance of the analyte from the sensor surface [30]. It is therefore well-suited for biomolecular studies in which the structure and orientation of the molecules are important. The Raman scattering cross section of molecules are usually very small. Therefore, the Raman signal emitted from them is very weak. Plasmonic nanoparticles are usually used on a substrate to bind to target molecules and enhance the weak Raman emission of target molecules [30]. A key challenge has been in realizing robust SERS substrates and there is an ongoing effort in making uniform, reproducible, and sensitive SERS substrates [3].

Different molecules have absorption in the infrared (IR) range, and IR-absorption can also be used to detect target molecules. The IR-absorption is another label-free sensing technique, which has been extensively used for chemical sensing [31]. Water has strong absorption bands in IR. Thus, the IR-absorption has a limited application when the sample of interest contains water, which is the case for most of biological samples. All these sensing techniques provide complementary information; nevertheless, they can be used together to increase the accuracy and reduce the errors.

## *1.2 Lab-on-a-chip Systems*

Different technologies and sciences are interfacing with each other to bring about the new concept of lab-on-a-chip or micro total analysis systems ($\mu TAS$) in analytical chemistry and biomedical diagnosis. Advances in biology, surface chemistry, mechanics, fluidics, optics, electronics, and nanofabrication have resulted in the possibility of realizing a ”lab” on a very small footprint in an integrated platform for detection, analysis, and manipulation of binding kinetics, chemical reactions, and molecular structures. Lab-on-a-chip systems are not merely miniaturized versions of conventional systems, but they also open up new potentials for

much more accurate and more sensitive analysis. lab-on-a-chip systems have found applications in point-of-care diagnostic testing [5], DNA analysis [32], drug screening [7], forensic analysis [11], and environmental monitoring [33]. Point-of-care diagnostic testing can help in diagnosis and treatment of diseases in the areas of the world with limited resources, and also early detection of cancers and diseases [5]. Prior to any observable symptoms, biochemical changes in the blood or other bodily serums can be used for identifying organ dysfunctions or diseases. Different diseases can be identified at an early stage by detecting the relevant proteins, peptides, or nucleotides that act as disease indicators [5]. As discussed in the previous section, optical sensing is a non-invasive and efficient method for analysis and sensing of molecules. Label-free optical sensing schemes can be realized on a chip to address the requirements of lab-on-a-chip sensing systems such as compactness, portability, small analyte volume, low power consumption, mass production capability, integrability, multi-analyte detection capability, and low cost [34–36]. Implementation of compact and portable photonic integrated sensors and microspectrometers is a subject of recent research endeavor.

## *1.3 Plasmonic Structures*

Surface plasmon polaritons (SPPs) form as a result of collective oscillations of electrons at a conductor-dielectric interface in resonance with lightwaves. Surface plasmons were first studied in the pioneering work of Ritchie in 1957 [37]. With the advent of nanofabrication and the progress in nanoscale patterning of materials, novel applications for SPPs have emerged. SPPs can help localize and guide the lightwave in subwavelength range, and therefore, they can be used to realize miniaturized circuits. By concentrating the lightwave in a very small footprint, ultrahigh field enhancements can be achieved. The ultrahigh field enhancement can be used to enhance light-matter interaction, alleviating

the requirement on using high optical powers. In other words, plasmonic structures can be used to achieve large field enhancements with low optical power levels. Therefore, plasmonic structures have been used for sensing applications, nonlinear optics, waveguiding, interconnection, modulation, and trapping and optical tweezing. Because of their extremely small sizes and very low power consumptions, plasmonic devices can be used to interface the two worlds of electronics and optics [38, 39], and in a hybrid platform they can be used for fast and efficient interconnecting of photonics and plasmonics. Generally, we can categorize plasmonic structures into propagating SPP devices and localized resonance-based plasmonic devices. The propagating SPP devices work based on the excitation of surface plasmon polaritons that propagate along the surface of a conductor-dielectric interface. To excite the propagating SPPs, energy and momentum matching conditions must be satisfied. The conservation of energy dictates the matching of the excitation frequency with the SPP frequency and the conservation of momentum imposes the matching of the excitation momentum along the surface with the propagating SPP momentum. The excitation of propagating SPPs is schematically shown in Figure 1(a). Propagating SPP devices have been used in the form of strip waveguides [40], slot waveguides [41], grove waveguides [42], and dielectric-loaded waveguides [43] to realize integrated circuit elements such as waveguides, interferometers, traveling-wave resonators, and filters [42] for a variety of applications ranging from communications to sensing. A key issue in these devices is the large propagation loss of SPPs. Some efforts have been dedicated to realizing long-range SPP propagating modes [44]. Still the propagation losses are on the order of a fraction of a dB per micrometer length, which limits the use of these devices for short distances. Localized surface plasmon resonance (LSPR) modes are excited in plasmonic nanoresonators in the form of dipole, quadrapole, or multipole resonances. The free electrons on the

surface of these plasmonic nanoresonators oscillate in resonance with the incident lightwave at certain resonance frequencies. The very localized surface plasmons in these structures result in ultrahigh field enhancements. The mode volume of these plasmonic nanoresonators can be extremely small. To excite the localized surface plasmon resonances, the energy (frequency) of excitation must coincide with the energy(frequency) of the LSPR mode. Since plasmonic nanoresonators are confined in space, the extent of momentums that are required to excite these modes is fairly broad, and therefore, there is no stringent requirement on the momentum matching. The excitation of plasmonic localized resonance modes is schematically shown in Figure 1(b). The resonance properties of plasmonic nanoresonators depend on their size, shape, and the material properties [45]. It should be noted that in the nanoscale, the properties of materials differ from the bulk material properties, and strongly depend on the surface area to volume ratio. The resonance wavelength of LSPR modes can be tuned over the entire visible range to near infrared range of the spectrum by designing the shape and the size of plasmonic nanoresonators. Plasmonic nanoresonators have been used in a broad range of applications ranging from sensing, surface enhanced Raman spectroscopy (SERS), nonlinear optics, photothermal therapy, nanofocusing, and imaging [46–50]. Since the sizes of plasmonic nanoresonators are comparable to the size of many biological molecules such as proteins with 10's of nanometer dimensions, they have been proven to be useful for probing biomolecules and studying their functionalities [51].

## *1.4 Integrated Photonic Structures*

Integrated photonic devices can be used to guide, trap, filter, and amplify lightwave on a chip. Passive and active structures can be realized in a photonic integrated platform. Different types of waveguides such as ridge and rib waveguides

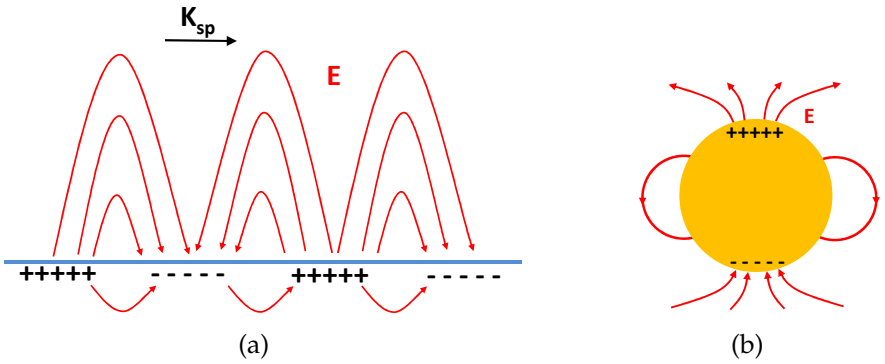


**Figure 1:** (a) Surface plasmon polariton (SPP) modes excited at the interface of a conductor and a dielectric. Excitation of SPPs requires momentum matching. (b) Localized surface plasmon resonance (LSPR) mode of a plasmonic nanoresonator can be excited. Electric field lines show the confinement of electromagnetic fields to the collective oscillations of electrons in the conduction band.

have been introduced for guiding of the lightwave [52]. Photonic microresonators such as traveling-wave resonators, photonic crystal cavities, and Fabry-Perots with high quality factors have been used to resonantly trap the lightwave [53]. Dispersive elements such as gratings [54], photonic crystals [55], and arrayed waveguide gratings (AWGs) [56] are used on a chip to realize demultiplexers, microspectrometers, and interferometers [57–59]. Photonic devices can be implemented in different material platforms such as $SiO_2$, $Si$, and $Si_3N_4$. The higher the contrast between the core and the surrounding medium, the more compact will be the photonic device. Therefore, silicon-on-insulator (SOI) platform is an appropriate material platform for implementing photonic devices since the index contrast between $Si$ and $SiO_2$, used as the insulating layer, is large, i.e., $\Delta n \sim 2$. $Si$ is well-suited for infrared range of spectrum, and has large absorption in the visible range. For visible and near infrared ranges, transparent materials such as $Si_3N_4$ must be used [60]. It has been shown that low loss and high quality photonic devices can be realized in $Si_3N_4$ on a $SiO_2$ substrate, where an index contrast of $\Delta n \sim 0.6$ can be achieved. Different photonic devices can be integrated in the form of a fully functional system, specially when combined with a tuning

mechanism such as thermal tuning [61] and carrier injection [62]. The sizes of photonic integrated devices are usually large and limited by diffraction laws. The two key photonic building blocks used in this research are ridge waveguides and traveling-wave microresonators shown in Figure 2(a) and Figure 2(b), respectively.

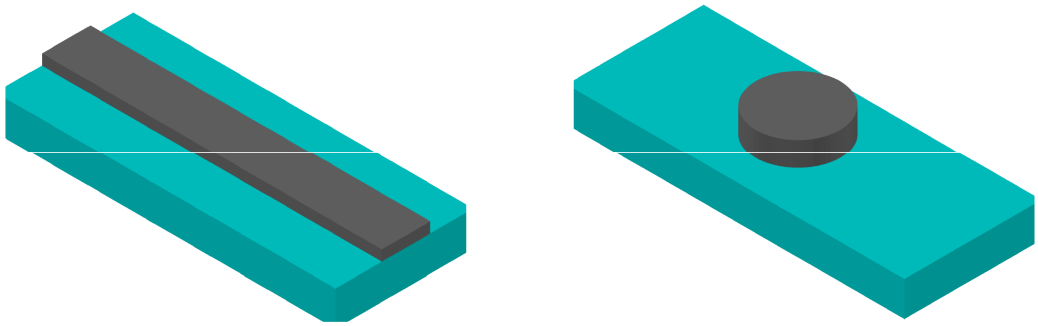

(a) (b)

**Figure 2:** (a) Schematic of a ridge photonic waveguide on a substrate. (b) Schematic of a photonic microdisk resonator on a substrate.

## *1.5 Hybrid Plasmonic-photonic Structures*

So far, we have discussed the advantages and limitations of plasmonic and photonic device platforms in sections 1.3 and 1.4. Also, we have learned about the requirements of lab-on-a-chip sensing systems in section 1.2. If the best of photonics and plasmonics worlds are combined in a hybrid plasmonic-photonic platform, then efficient lab-on-a-chip devices can be realized, which can meet the requirements of enhanced on-chip light-matter interaction for molecular sensing applications.

Some recent efforts have been devoted to combining plasmonics and photonics. In 2006, Ian M. White et al. showed that if a silica microsphere is immersed in a solution consisting of a mixture of silver nanoparticles and Rhodamine 6G (R6G) molecules, then the Raman emission of R6G molecules attached to

silver nanoparticles can be enhanced [63]. This experiment has shown that the whispering gallery modes of a microsphere can excite the near field plasmonic resonance of the silver nanoparticles attached to the surface of the microsphere. In this experiment, silver nanoparticles randomly attach to the surface of the microsphere and form clusters. A plasmonic nanoantenna with an ogival-shape tip combined with a planar photonic crystal cavity was also demonstrated by Francesco De Angelis in 2008 [64]. This structure was used to sense a few molecules on the plasmonic nanoantenna tip. The nanoantenna focuses the incident light into a nanoscale region to interact with the molecules and the photonic crystal cavity couples the intrinsically evanescent surface plasmon polariton (SPP) mode of the nanoantenna to a propagating mode that can be detected as far-field scattering. This device is excited using out of plane incidence and can be used as a near field probe. A nanoassembled plasmonic-photonic hybrid cavity was demonstrated by Michael Barth et al. in 2009 [65]. The structure consists of a planar photonic crystal cavity and plasmonic nanostructures that are placed inside the cavity by using an AFM tip. It has been shown that the Purcell factor of this hybrid cavity is one order of magnitude larger than that of a bare photonic crystal cavity. The plasmonic nanoparticles can be accurately placed on top of the photonic crystal cavity. However, this method of hybridization cannot be easily used for making practical devices. In each of the last two examples, a planar photonic crystal cavity was used as the photonic structure that is excited using out of plane incidence. Although planar photonic crystal cavities have shown large Purcell factors, the lack of an efficient on-chip excitation mechanism has limited their application.

In this research, I have focused on the design, implementation, and experimental demonstration of plasmonic and photonic hybrid structures with enhanced properties and capabilities for on-chip biochemical sensing and spectroscopy.

Photonic dielectric waveguides with low propagation losses are employed to steer the lightwave on the chip and to couple the lightwave to the surface plasmon polariton (SPP) modes of plasmonic waveguides and to excite the localized surface plasmon resonance (LSPR) modes of plasmonic nanoresonators. Photonic microresonators with high quality factors are employed to trap the lightwave on the chip and to excite the plasmonic modes of integrated plasmonic structures efficiently. It will be shown that by properly designing the hybrid structures, ultrahigh field enhancements can be achieved, enhancing light-matter interaction. Also, on-chip sensing devices with high sensitivity in the hybrid plasmonic-photonic platform can be realized. It will also be shown that plasmonic structures can be efficiently excited with low loss in the hybrid platform. Combining plasmonics and photonics on a chip brings about new potentials for device design concepts.

Chapter 2 is devoted to the design and experimental demonstration of plasmonic nanoresonators and their applications in sensing. Hybrid plasmonic-photonic waveguide structures are discussed in chapter 3. The experimental demonstration of hybrid plasmonic-photonic waveguide structures is discussed in chapter 4, where the details of the developed fabrication processes and the implemented optical characterization setup are presented. The application of hybrid waveguide structures for on-chip LSPR sensing is also demonstrated in this chapter. In chapter 5, the design and experimental demonstration of hybrid plasmonic-photonic resonator structures are discussed, where the developed theoretical model, numerical simulations, and the experimental demonstration are discussed. The implementation and integration of microfluidic channels with the hybrid plasmonic-photonic structures are discussed in chapter 6. Finally conclusion is given in chapter 8.

# CHAPTER II

# PLASMONIC NANORESONATOR DESIGN AND EXPERIMENTAL DEMONSTRATION

The integration of plasmonic nanoresonators with photonic waveguide and microresonator structures will be discussed in chapters 3 and 5, respectively. These structures consist of plasmonic nanoresonators and photonic integrated structures. When plasmonic nanoresonators are integrated with photonic structures, their LSPR modes are affected and the electromagnetic field profiles and the resonant properties change. However, separate design and test of plasmonic nanoresonators can serve as a reasonable starting point in the design of the hybrid structures. Also, the experimental characterization of plasmonic nanoresonators in the absence of photonic structures ensures the reliability of the fabrication steps for implementing plasmonic nanoresonators in a hybrid platform. In this chapter, the design, fabrication, and experimental characterization of plasmonic nanoresonators is discussed, where the simulation methods, the developed fabrication processes, and the implemented optical characterization setup will be discussed.

## *2.1 Analysis and Design of Plasmonic Nanoresonators*

Plasmonic nanoresonators or plasmonic nanoparticles have been the subject of intensive research for decades. As discussed earlier in section 1.3, plasmonic nanoresonators usually made of nobel metals interact with the lightwave and the electrons on the surface of such plasmonic nanoparticles collectively oscillate at certain frequencies in resonance with the incoming lightwave. This process results in localized surface plasmon resonance (LSPR) modes that confine electromagnetic

energy in a very small scale, near the surface of the plasmonic nanoresonators. The intensity of light in the nearfield of plasmonic nanoparticle LSPR modes is very high, making them suitable for efficient light-matter interaction. The LSPR modes can be in the form of dipoles, quadrapoles, and multipoles [45]. The resonance wavelengths of LSPR modes depends on the nanoparticle material, shape, size, and the surrounding dielectric environment [45]. Different shapes of plasmonic nanoresonators have been introduced to tailor the LSPR modes, covering different wavelength ranges from visible to nearinfrared.

To analyze and design plasmonic nanoresonators, Maxwell's equations need to be solved to obtain the electromagnetic solution to the scattering and absorption by plasmonic nanoresonators. Different analytic and semi-analytic methods have been used to study and analyze the properties of plasmonic nanoresonator modes. For example, Mie theory [66] can be used to solve the problem of scattering from a gold sphere in the form of an infinite series. The analytic and semi-analytic methods provide more insight into the problem; however, they are limited to certain shapes of structures. Numerical methods such as FEM [67], DDA [68], and FDTD [69] can be used for the analysis of plasmonic nanoresonators of arbitrary shape. Here, FDTD is used to analyze the plasmonic nanoresonators. To obtain the LSPR modes of plasmonic nanoresonators, a pulsed plane excitation source is used, and then the electromagnetic waves at different points are recorded over time. The Fourier transform of the electromagnetic waves reveals the resonance modes. As the first example, two gold nanorods of dimensions $100 \times 56 \times 30$ $nm$ and $120 \times 56 \times 30$ $nm$ embedded in a medium with a refractive index of $n = 2$ are analyzed using FDTD. The normalized amplitude of the electric field probed at a location 2 $nm$ away from the gold nanorod tip is plotted versus wavelength for each of these gold nanorods in Figure 3, where it can be seen that the larger gold nanorod has a higher resonance wavelength, and larger bandwidth. In these

simulatiions, the source polarization is along the $z$ axis and propagation is in $x$ direction. The gold nanorod is defined in the simulation domain with its longer dimension along the $z$ direction.

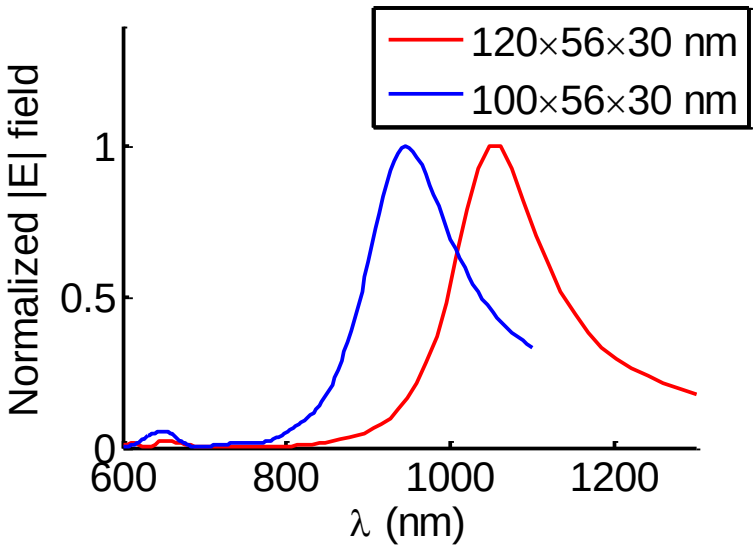


**Figure 3:** The normalized electric field amplitude for two gold nanorods of dimensions $100 \times 56 \times 30$ $nm$ and $120 \times 56 \times 30$ $nm$ embedded in a medium with a refractive index of $n = 2$.

The nearfield electric field amplitude profiles of the LSPR mode of $120 \times 56 \times 30$ $nm$ gold nanorod at $xz$ and $yz$ cross sections of the nanoparticle are plotted in Figure 4(a) and 4(b), respectively. It can be seen that the light is highly concentrated at the two ends of the gold nanorod, and is very intense.

It should be noted that the behavior of the plasmonic nanoresonators highly depends on their surrounding environment. To study the effect of the surrounding environment on the LSPR properties of gold nanorods, the electric field intensity spectrum of a $100 \times 56 \times 30$ $nm$ gold nanorod is shown in Figure 5 for the three cases of different surrounding medium environments.

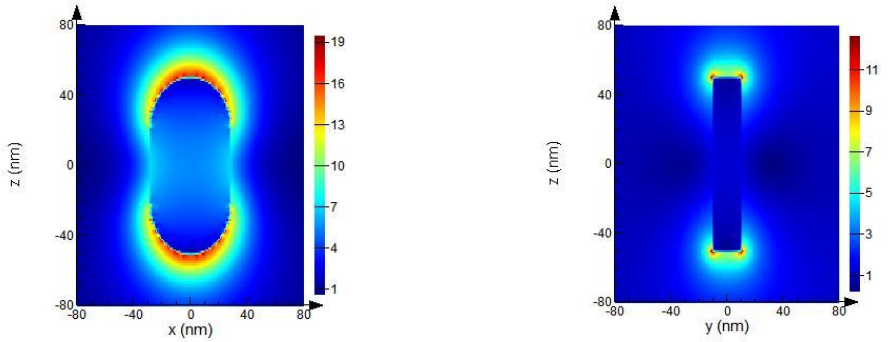


(a) (b)

**Figure 4:** The nearfield electric field amplitude profiles of a $120 \times 56 \times 30\ nm$ gold nanorod at $xz$ and $yz$ cross sections of the nanoparticle.

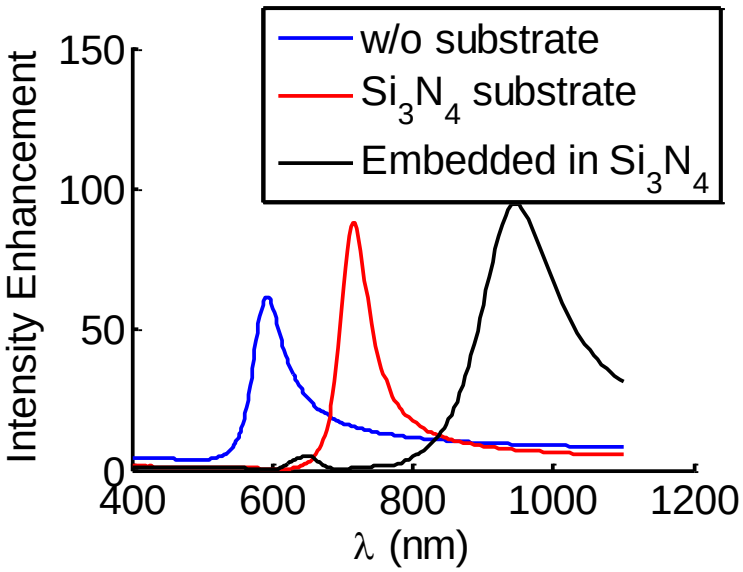


**Figure 5:** The electric field intensity spectrum of a $100 \times 56 \times 30\ nm$ gold nanorod for the three cases of different surrounding medium environments, i.e., air, $Si_3N_4$ substrate, and $Si_3N_4$ surrounding medium.

When the surrounding environment is air, the longitudinal LSPR resonance wavelength is $\lambda_0 = 593\ nm$. When the surrounding environment is changed to a medium with a refractive index of $n = 2$, then the LSPR mode redshifts to $\lambda_0 = 950.5\ nm$, and the resonance linewidth broadens. When the gold nanorod is placed on a $Si_3N_4$ substrate with a refractive index of $n = 2$, then the LSPR wavelength is $\lambda_0 = 715.5\ nm$, which is in between the two previous cases. This is

somewhat expected, since in this case, the nanoparticle is exposed to a half air and half $Si_3N_4$ medium. The other interesting observation is that the LSPR lineshape of the gold nanorod sitting on a $Si_3N_4$ substrate is narrower than the LSPR lineshape of the gold nanorod when completely exposed to air. This can be understood from the interference effects arising from the reflection of light from the surface of $Si_3N_4$.

## *2.2 Fabrication and Experimental Characterization of Plasmonic Nanoresonators*

Plasmonic nanoresonators or nanoparticles investigated in this thesis are either fabricated using the top-down procedure using EBL and lift-off procedure, or chemical synthesis methods [70]. To fabricate plasmonic nanoparticle arrays, first a layer of PMMA resist is spun on the substrate and then it is baked according to the procedure that is outlined in section 4.1. Then the patterns of plasmonic nanoparticles are exposed on the sample using a JEOL JBX-9300FS EBL System. The electron beam energy is 100 $keV$ and the beam current is 2 $nA$. The dosage is optimized in each case according to the size and density of the nanoparticles. For the transparent substrate the height of the sample is manually measured in the SEM mode of the EBL machine to focus the electron beam. The exposed resist is then developed in a mixture of MIBK:IPA $(1:1)$ for 90 $sec$. The patterns of an array of nanodisks and an array of nanorods formed in PMMA are shown in the scanning electron micrographs (SEMs) of Figure 6(a) and Figure 6(b), respectively. It can be seen that almost identical array elements can be obtained. It should be noted that since the substrate is insulating, the surface is heavily charged up due to the accumulation of the electrons on the surface of the resist. Therefore, a thin layer of chromium is deposited on the sample to prevent charge up. The roughness of the edges of the features is because of the grains of chromium.

In the next step, appropriate metals are deposited and then a lift-off procedure

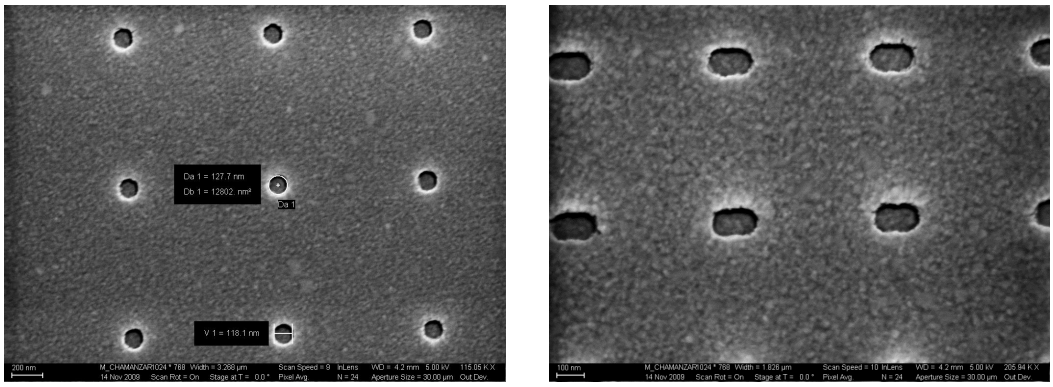

(a) (b)

**Figure 6:** SEM of (a) nanodisk and (b) nanorod array patterns formed in PMMA using EBL. The surface is coated with chromium to prevent charge up.

is carried out. For the silver nanoparticles, a thin layer of chromium ( $3nm$) is used and for the gold a thin layer of titanium is used as the adhesion layer. After the lift-off, arrays of nanoparticles are formed. As an example, the SEM of an array of gold nanodisks on a quartz substrate is shown in Figure 7.

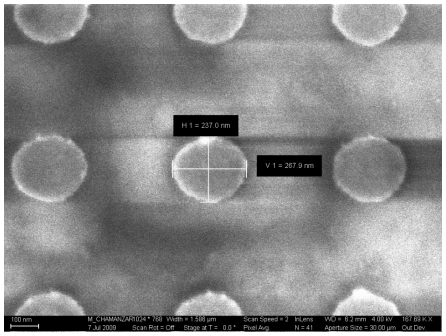

**Figure 7:** SEM of a nanodisk array on a quartz substrate.

It should be noted that since the quartz substrate is insulating, the SEM imaging is challenging as the electrons accumulate on the substrate resulting in the charge-up problem that affects the image quality. To prevent this issue, the imaging is carried out very carefully at high scan rates.

To investigate the properties of such plasmonic nanoparticles in the absence of photonic structures, they are characterized either in solution or assembled on a transparent substrate such as a glass or quartz slide.

A transmission microabsorption setup is designed and implemented to characterize the plasmonic nanoparticle arrays. The schematic of this characterization setup is shown in Figure 8.

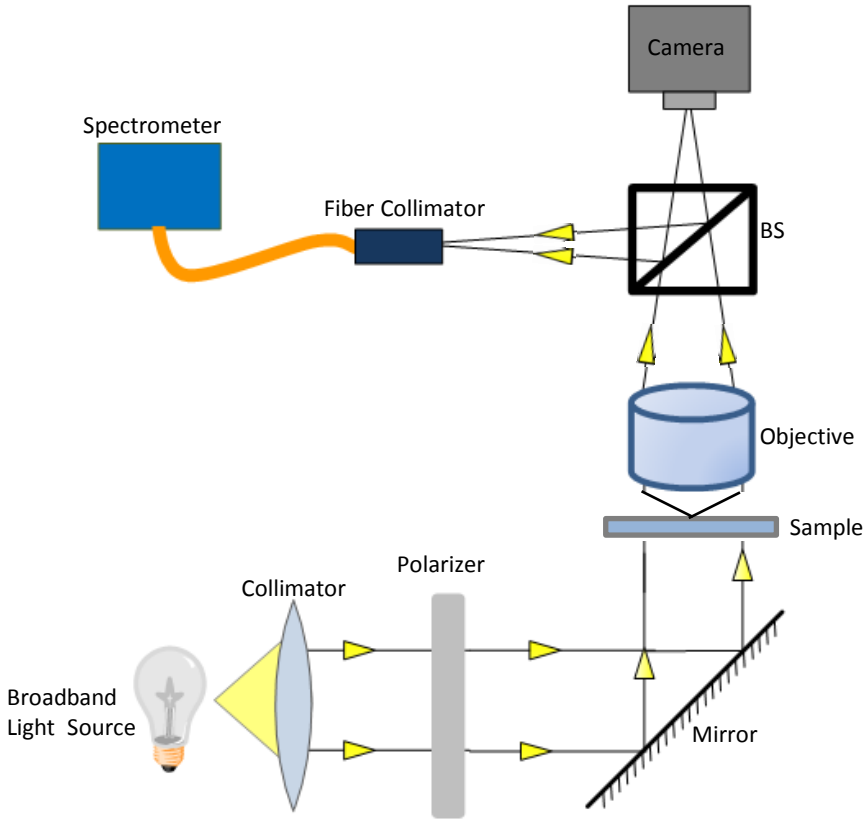


**Figure 8:** Schematic of a free-space microabsorption microscope setup with polarization control.

Light from a broadband light source is collimated and is passed through a polarizer. Then the beam is deflected by using a 45° mirror to pass through the sample. An objective lens is designed to image the surface of the sample and direct light to the upper column of the microscope. The microscope column consists of a beam splitter that splits the incoming light between a camera and a fiber input to a spectrometer. Light is coupled to the fiber through a collimator. Using this setup, the extinction and the transmission spectrum of the sample at different locations can be precisely measured with a resolution of a few microns depending

on the type of objective lens used. The spectrometer used in this setup is an Ocean Optics USB 2000+ with a spectral resolution of 0.3 $nm$. To measure the extinction spectrum, first a reference is measured on a location of the sample, where there is no nanoparticle. Also, the background is measured by blocking the light source. Then the transmission of the sample is measured at the location of interest. Post analysis codes are developed in MATLAB to calculate the extinction spectrum from the measurement data according to the following equation,

$$Extinction \; = \; -10log(\frac{Trans_{Sample}(\lambda) - D}{Trans_{Ref}(\lambda) - D}), \tag{1}$$

where $Trans_{Sample}$ is the sample transmission, $Trans_{Ref}$ is the reference transmission , and $D$ is the dark measurement. The image of the microabsorption setup is shown in Figure 9 with different components labeled.

This characterization setup can generally be used for measuring the extinction or transmission spectrum of any sample at different input polarization states.

The normalized extinction spectra measured for four different plasmonic nanorod arrays of dimensions $114 \times 57 \times 30$ $nm$, $124 \times 57 \times 30$ $nm$, $133 \times 57 \times 30$ $nm$, and $142 \times 57 \times 30$ $nm$ are plotted in Figure 10. In this figure, the post-processed measurement results according to the method that is outlined in Appendix A are shown. The nanoparticles are fabricated using the top-down method involving the EBL and lift-off procedure. A 3 $nm$ titanium is used as the adhesion layer under the gold nanorods. In these measurements, the input polarization is set to be along the longer dimension of the gold nanorods. The longitudinal LSPR wavelengths are listed in Table 1. As the aspect ratio of the plasmonic nanorod is increased, the longitudinal LSPR mode wavelength redshifts.

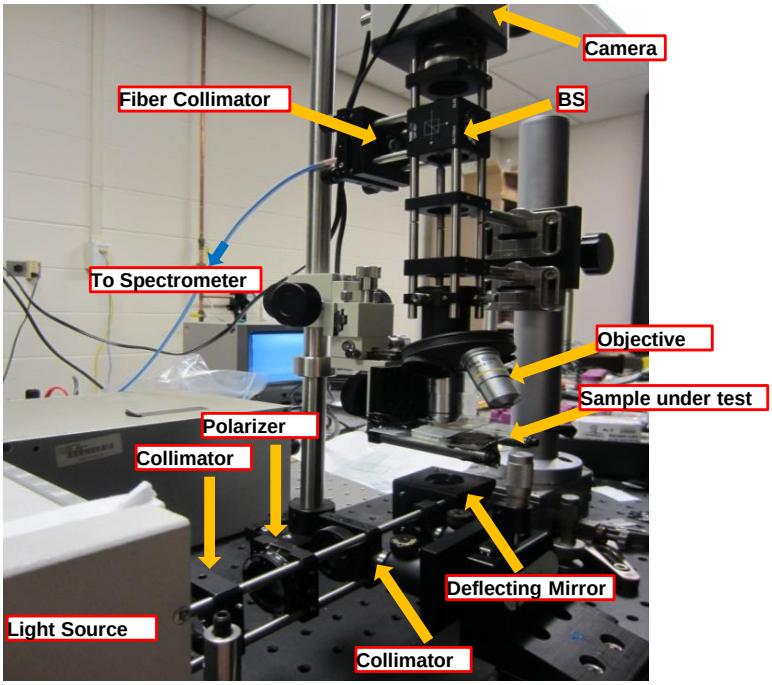


**Figure 9:** Image of the free-space microabsorption microscope setup with polarization control to measure plasmonic nanoresonator arrays.

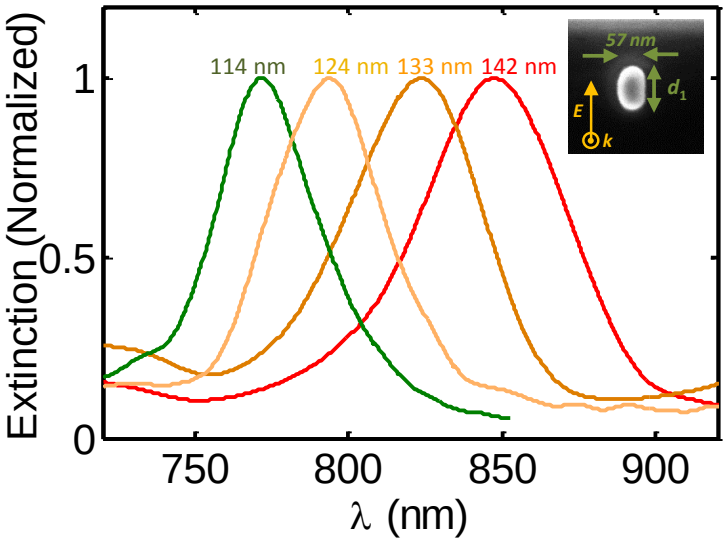


**Figure 10:** The extinction spectrum of the longitudinal LSPR mode for four different gold nanorods of dimensions $114 \times 57 \times 30\ nm$, $124 \times 57 \times 30\ nm$, $133 \times 57 \times 30\ nm$, and $142 \times 57 \times 30\ nm$. It can be seen that the longitudinal LSPR wavelength redshifts as the length of the nanorod is increased.

**Table 1:** Gold nanorod arrays longitudinal LSPR mode wavelengths

| Gold NanoRods | longitudinal LSPR wavelength ($\lambda_0$) |
|---|---|
| $114 \times 57 \times 30\ nm$ | $771.2\ nm$ |
| $124 \times 57 \times 30\ nm$ | $793.5\ nm$ |
| $133 \times 57 \times 30\ nm$ | $824\ nm$ |
| $142 \times 57 \times 30\ nm$ | $847\ nm$ |

The polarization is then changed by $90^\circ$ so that the lateral LSPR modes are excited. The extinction spectrum corresponding to the lateral LSPE mode is measured for each of the above mentioned gold nanorod arrays, and the results is shown in Figure 11. It can be seen that the resonance wavelengths are almost the same. This is expected since the lateral dimensions of these nanorods are all the same. The slight differences in the resonance wavelengths as well as the lineshapes arise from the fact that the limited length of the nanorods affect the lateral resonance modes. Also, there would exist slight variations in similarly designed dimensions from one array to the other, due to fabrication imperfections.

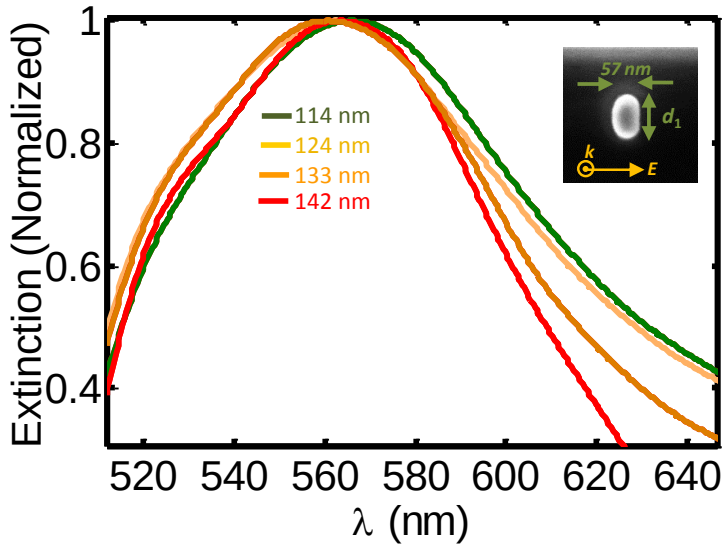


**Figure 11:** The extinction spectrum of the lateral LSPR mode for four different gold nanorods of dimensions $114 \times 57 \times 30\ nm$, $124 \times 57 \times 30\ nm$, $133 \times 57 \times 30\ nm$, and $142 \times 57 \times 30\ nm$. It can be seen that the lateral LSPR mode wavelengths are almost identical.

Another type of plasmonic nanoresonator that has been the subject of recent research attention is bowtie nanoantenna [71]. It consists of two identical plasmonic triangles, as shown in Figure 12, that focus the incoming light at their tips. In the gap between the two tips, a strong field is formed as a result of the coupling of the two plasmonic modes. In this resonance gap mode, an intense field is formed in the gap between the two tips of the plasmonic nanotriangles, where strong light-matter interaction can happen. This makes bowtie antennas very interesting for sensing applications. An array of bowtie antennas are designed and fabricated using the top-down procedure that was discussed earlier in this section. The sizes of triangles are designed to be $d_1 = d_2 = 80\ nm$. Different gap sizes, $g$'s, are considered here.

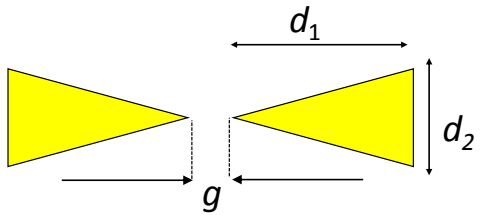


**Figure 12:** The schematic of a bowtie antenna with all the dimensions specified.

The SEM of an array of identical bowtie nanoantennas fabricated on a quartz substrate is shown in Figure 13. The extinction spectrum of an array of bowtie nanoantennas consisting of identical triangle pairs of dimensions $d_1 = d_2 = 80\,nm$, and $g = 5\ nm$ with a thickness of 30 $nm$ is measured at two different input polarization states, one with the electric field along the gap direction and the other one with the electric field perpendicular to the gap direction. The results are shown in Figure 14. It can be seen that when the input electric field polarization is along the gap direction, the LSPR gap mode is excited at a longer wavelength. On the other hand, when the electric field is along the lateral direction, a lateral LSPR mode is excited corresponding to the effective lateral width of the bowtie nanoantenna.

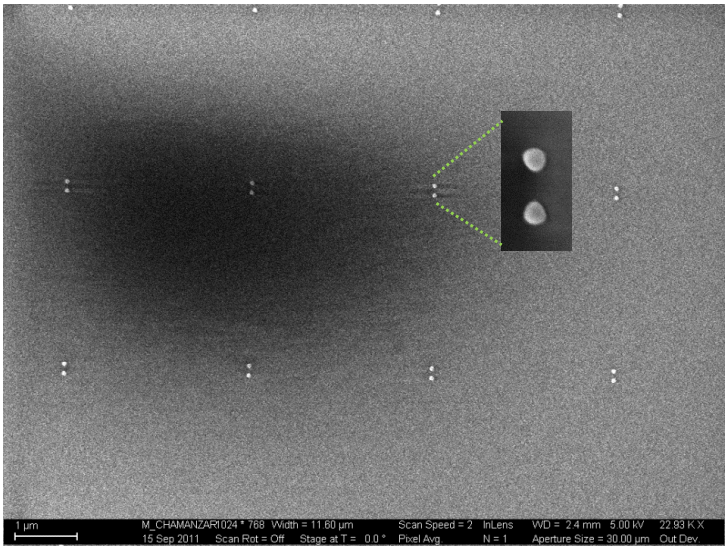

**Figure 13:** The SEM of an array of plasmonic gold bowtie nanoantennas fabricated on a quartz substrate.

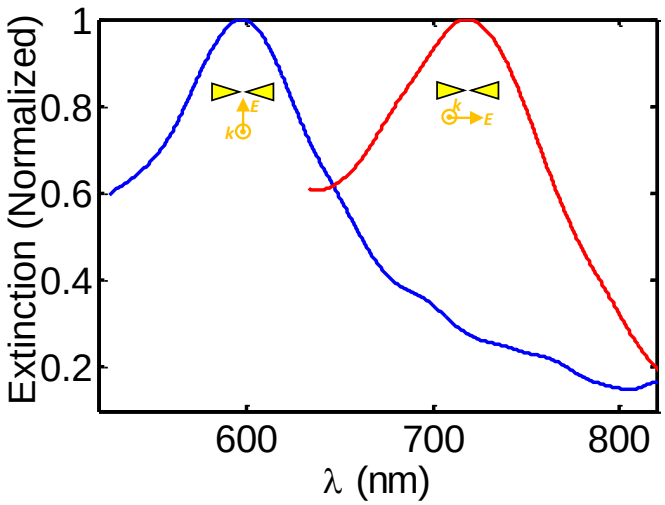


**Figure 14:** The measured extinction spectrum of a bowtie nanoantenna array consisting of identical triangle pairs of dimensions $d_1 = d_2 = 80\ nm$, and $g = 5\ nm$ with a thickness of 30 $nm$ at two perpendicular input polarization states.

Another measurement was carried out on an array of bowtie nanoantennas, each one with similar dimensions; however, with a gap size of $g = 15\ nm$. It can be seen from Figure 15 that there are two LSPR modes corresponding to the gap mode and the lateral resonance modes. Compared to the results in Figure 14, the lateral LSPR mode wavelength is almost the same, whereas the LSPR gap mode is

blueshifted. This behavior is expected, since the gap mode is in fact a supermode resulting from the coupling of the two triangle degenerate resonance modes, and as the gap between the two triangles is decreased, the splitting of the super modes is increased and the gap mode occurs at longer wavelengths.

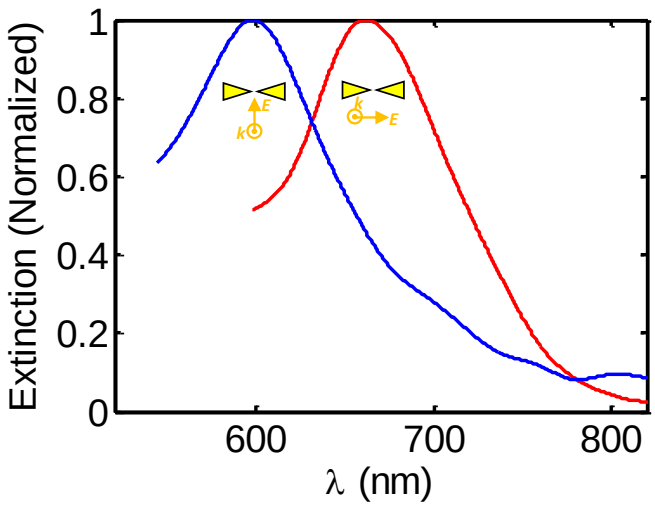


**Figure 15:** The measured extinction spectrum of a bowtie nanoantenna array consisting of identical triangles of dimensions $d_1 = d_2 = 80\,nm$, and $g = 15\,nm$ with a thickness of 30 $nm$ at two perpendicular input polarization states.

Novel hollow-core plasmonic nanoresonators have been recently introduced in the form of gold nanocages (AuNC) and gold nanoframes (AuNF) [70]. These nanoresonators, usually prepared using chemical synthesis methods, can provide ultra-high field enhancements and very large sensitivities ($\sim 600\ nm/RIU$). These nanoparticles are prepared using a galvanic replacement chemical synthesis method in Lasers Dynamics Laboratory (LDL) at Georgia Tech. We have used these chemically synthesized plasmonic nanoresonators in this research. The SEM of a typical AuNC assembled on a substrate is shown in Figure 16 with a wall length of $\sim 50\ nm$ and a wall thickness of $\sim 4\ nm$.

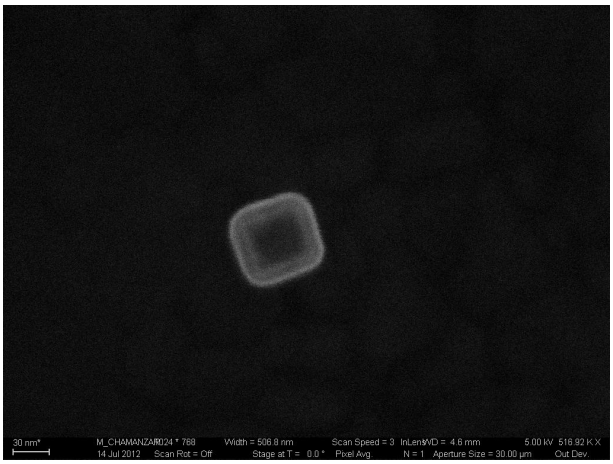

**Figure 16:** SEM of a gold nanocage (AuNC) with a wall length of $\sim 50\ nm$ and a wall thickness of $\sim 4\ nm$.

A monolayer of plasmonic AuNCs with a wall length of $\sim 50\ nm$ and a wall thickness of $\sim 4\ nm$ is assembled on a glass slide using the Langmuir-Blodgett technique [72]. The extinction spectrum of this assembled monolayer is measured, and the result is shown in Figure 17.

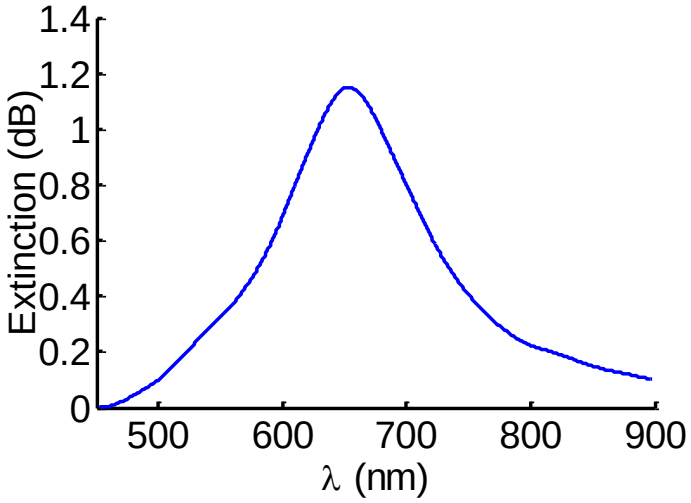


**Figure 17:** Extinction spectrum of a monolayer of gold nanocages (AuNCs) with wall length of $\sim 50\ nm$ and wall thickness of $\sim 4\ nm$ assembled on a glass substrate.

## 2.3 *Surface Enhanced Raman Spectroscopy (SERS) using Plasmonic Nanoresonators*

The Raman effect was discovered in 1928 by C. V. Raman as a secondry radiation or inelastic scattering of molecules when excited by an intense light source [73]. Raman scattering spectrum provides a unique means of detection of molecules based on different vibrational/rotational states of the molecule. As it can be seen from Figure 18, when a laser light at a certain wavelength ($\lambda_0$) excites a molecule, the scattered light can be at a slightly shifted wavelength due the rotational and vibrational bands of the molecule.

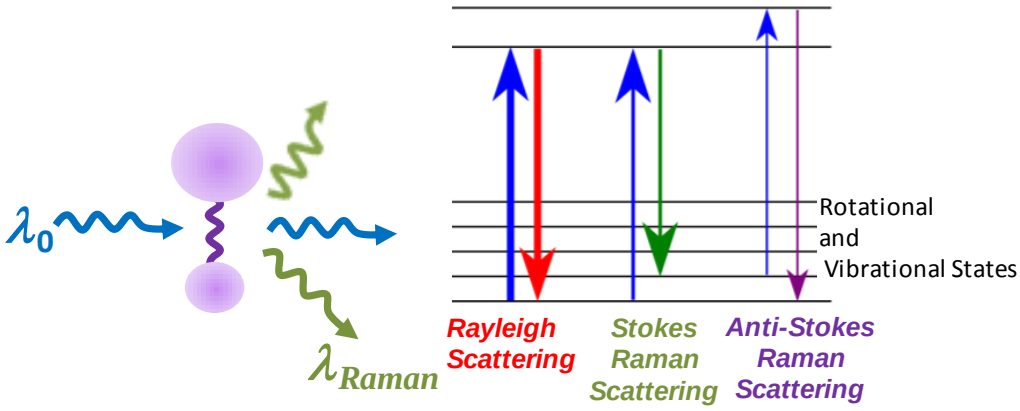


**Figure 18:** Illustration of Raman scattering concept. The Raman scattered light is at a slightly shifted wavelength due the rotational and vibrational bands of the molecule. The molecule energy band diagram is shown, with the excitation and the Raman transitions indicated.

Raman scattering spectrum can serve as a fingerprint of the molecule revealing its different rotational and vibrational states of all the available bonds. Therefore, Raman spectroscopy can be used as a very specific label-free detection mechanism. Since the Raman scattering cross section of molecules are usually very small ($\sim 10^{-30} cm^2$). Therefore, detection of the Raman signal requires an intense light source and many number of molecules. To detect low concentrations of molecules using the Raman scattering effect, an enhancement mechanism is required. It

was in 1977 that the enhancement of the Raman scattering of a molecule near a metal surface was noted [74]. The surface plasmon polaritons excited at the interface of a metal surface and a dielectric medium result in an intense field, enhancing the Raman emission. This effect was named surface enhanced Raman scattering (SERS), and the spectroscopy based on this effect is called surface enhanced Raman spectroscopy (SERS). It was also noted that in addition to the electromagnetic field enhancement, a chemical effect arising from the charge transfer between the molecule and the metal contributes to the enhancement of the Raman emission signal [30]. It was also shown later that the LSPR mode of a plasmonic nanoresonator can result in the enhancement of the Raman emission signal of molecules in the vicinity of the plasmonic nanoresonator [75]. Very large Raman enhancements on the order of ($\sim 10^{10}$) have been demonstrated [76]. To demonstrate SERS using the previously discussed plasmonic nanoresonator arrays, thiophenol ($C_6H_6S$), a simple aromatic thiol, is used as the model analyte. The thiol moiety in thiophenol (or Benzenethiol) forms a strong chemical bond with gold atoms on the surface of the nanoparticles. A self-assembled monolayer (SAM) thiophenol was adsorbed on the surface of gold nanoparticles in the vapor phase. Then a Raman microscope (Renishaw InVia micro Raman system) was used with the excitation laser wavelength of $\lambda_0 = 785\ nm$.

As the first device to test, a monolayer of gold nanocages (AuNCs) assembled on a glass substrate using the Langmuir-Blodgett technique is used. The extinction spectrum of this AuNC monolayer is measured and is shown in Figure 19. The location of the laser wavelength is also indicated in this Figure. Since the nanoparticles are aggregated on the surface of the glass, the LSPR mode extends to higher wavelengths, and can enhance the pump intensity as well as the Raman emission intensity.

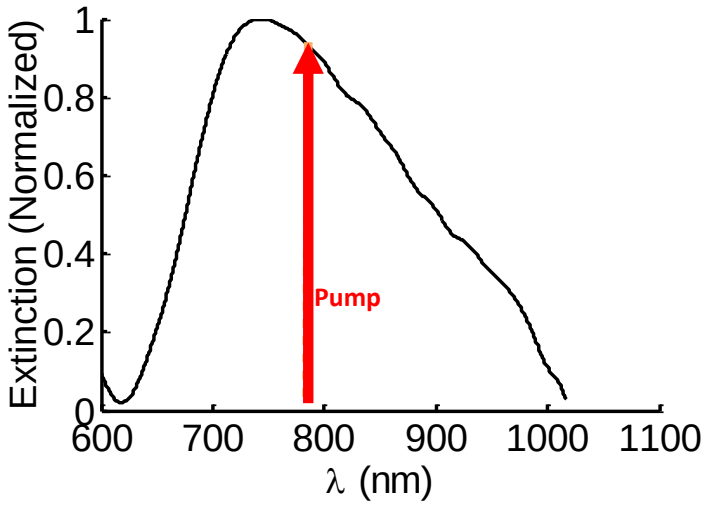


**Figure 19:** Extinction spectrum of a monolayer of gold nanocages (AuNCs) with wall length of $\sim 50\ nm$ and wall thickness of $\sim 4\ nm$ assembled on a glass substrate. The nanoparticles are aggregated, and therefore the resonance is extended to longer wavelengths.

The SERS spectrum of the thiophenol adsorbed on the AuNC sample is measured with a pump power of $P = 50\ mW$ at a wavelength of $\lambda_0 = 785\ nm$, and an integration time of 15 *sec* using a Renishaw Raman microscope. The measurement result is shown in Figure 20, where different Raman peaks are assigned according to the corresponding vibrational or rotational events [77]. The baseline was corrected by performing a piece-wise Fourier transform to obtain the background and subtract it from the signal.

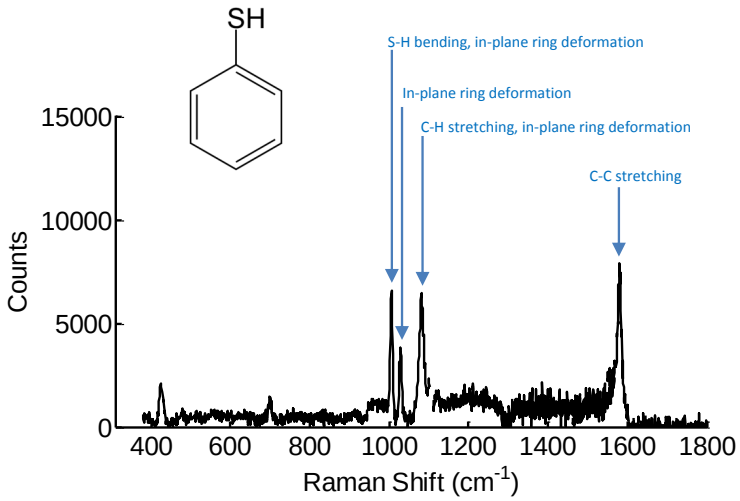


**Figure 20:** SERS spectrum of a self-assembled monolayer (SAM) of thiophenol on the surface of a monolayer of AuNCs with wall length of $\sim 50\ nm$ and wall thickness of $\sim 4\ nm$ assembled on a glass substrate. The nanoparticles are aggregated. The Raman spectrum was measured with a micro Raman system equipped with a pump laser at wavelength of $\lambda_0 = 785\ nm$ and with a power of $P = 50\ mW$. The integration time was 15 *sec*. The appropriate Raman bands are assigned according to the corresponding vibrational or rotational events.

Another set of measurements were carried out on lithographically fabricated plasmonic nanoparticle arrays. Again, a self-assembled monolayer (SAM) thiophenol was adsorbed on the surface of the plasmonic nanoresonators in the vapor phase. First, an array of gold nanorods with dimensions of $124 \times 57 \times 30\ nm$ was used. It was shown in Figure 10 that the longitudinal LSPR peak occurs at $\lambda_0 = 793\ nm$. When a thiophenol SAM forms on the surface of the nanoparticles, the LSPR peak wavelength redshifts by a few nanometers. The SERS spectrum of the thiophenol SAM on these gold nanorods is measured using the same setting of the Raman microscope as the those used for the measurement of AuNCs. The SERS spectrum is shown in Figure 21. It can be seen that with the same power setting and the same integration time, the Raman band peak intensities are weaker than those of AuNCs. This is in part because of the fact that the field enhancement of AuNCs is larger than the field enhancement of gold nanorods. Also, the density

of the AuNCs on the surface is higher than the density of gold nanorods that are spaced by 1 $\mu m$ from each other.

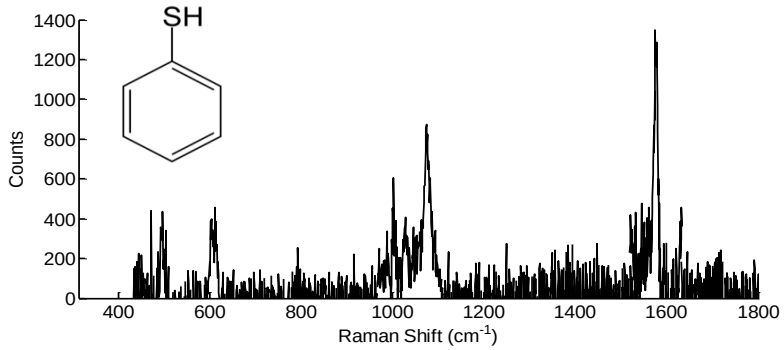


**Figure 21:** SERS spectrum of a self-assembled monolayer (SAM) of thiophenol on the surface of an array of $124 \times 57 \times 30$ $nm$ gold nanorods on a glass substrate. The Raman spectrum was measured with a micro Raman system equipped with a pump laser at wavelength of $\lambda_0 = 785$ $nm$ and with a power of $P = 50$ $mW$. The integration time was 15 $sec$.

The SERS spectrum of thiophenol was also measured on an array of gold bowtie nanoantennas with dimensions of $d_1 = d_2 = 80$ $nm$, and $g = 3$ $nm$. The result is shown in Figure 22. It can be seen that the Raman emission signal is highly enhanced due to the LSPR gap modes. The molecules trapped in the gap between the two tips of the bowtie nanoantennas feel a strong field, and the Raman emission is enhanced. Different types of plasmonic nanoparticles can be fabricated either using the top-down fabrication method or the chemical synthesis method, and the corresponding LSPR modes can be experimentally measured using the developed microabsorption microscope, and the resulting field enhancements can be used for SERS measurement of different analytes.

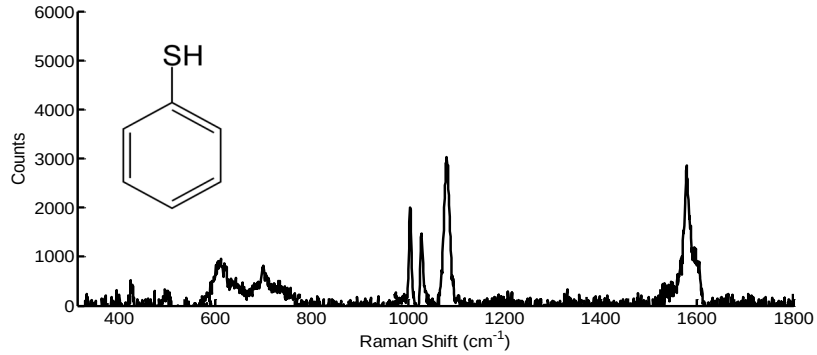


**Figure 22:** SERS spectrum of a self-assembled monolayer (SAM) of thiophenol on the surface of an array of $d_1 = d_2 = 80\,nm$, $g = 3\,nm$ bowtie nanoantennas on a glass substrate. The Raman spectrum was measured with a micro Raman system equipped with a pump laser at wavelength of $\lambda_0 = 785\,nm$ and with a power of $P = 50\,mW$. The integration time was 15 *sec*.

## *2.4 Detection of Glycan-toxin Binding using Plasmonic Nanoresonators*

Glycans are polysaccharides that are widely found in mammalians and cover the surface of different cells. Since glycans are mostly located on the surface of cells, they can regulate and mediate different cell functionalities such as cell signalling, cell communication with other cells, and interaction of cells with different molecules [78]. Various infectious microorganisms and toxins use specific types of glycans as recognition targets to enter the cell and cause infection [78]. Therefore the interaction of pathogen proteins with glycans play a key role on the onset of different diseases. This model of protein-glycan binding that exists in nature in the molecular level, can be employed to develop efficient, and specific diagnostics sensors based on synthetic glycans [79]. In this paradigm, glycans can be used as receptors to functionalize the transducer surface. The specific binding of target toxins and other pathogens to glycans can then be recognized by the transducer. The detection and study of glycan-protein bindings not only

can be used for sensing and diagnostics applications, but it can also be used to further understand and explore biological processes involved in the development of different diseases in the molecular level. Such information can then be used to design specific types of compounds that inhibit a specific glycan binding site to control the development of a disease [78].

Here, novel plasmonic nanoresonators in the form of gold nanocages (AuNCs), assembled on a glass surface have been used as LSPR sensors to detect toxins. The surface of the AuNCs is functionalized using a monolayer of glycan receptors at high density. Then, the target toxins can be detected by monitoring the shift of LSPR peak wavelength as they bind specifically to the glycan receptors. We use purified pentasaccharide GM1 glycans as the receptor to detect B-subunit of Cholera Toxin (CTB) as the model analyte.

A protocol was designed for functionalizing AuNCs with glycans. In the first step, purified glycans obtained from the Glycomics Center at Emory University were mixed with thioctic acid NHS ester in dry ethanol. This way, the NHS reacts with the glycans and a chain is formed that has two sulfides on one end and a glycan on the other end. Then this compound is introduced to the AuNCs, and the sulfides bind to AuNCs. To verify the specific chemical binding of the NHS ester to AuNCs, and the required incubation time, binding kinetics of the thioctic acid NHS ester to colloidal AuNCs is measured using a UV-Vis absorption spectrometer. The extinction spectrum of colloidal AuNCs measured over time is shown in Figure 23, after the introduction of 100 $\mu L$ of the thioctic acid NHS ester with a concentration of 200 $\mu M$ to 110 $\mu L$ of colloidal AuNCs. The volume was increased to 1.5 $mL$ by adding dry ethanol. It can be seen from the inset of Figure 23 that the LSPR wavelength redshifts as the NHS ester binds to AuNCs.

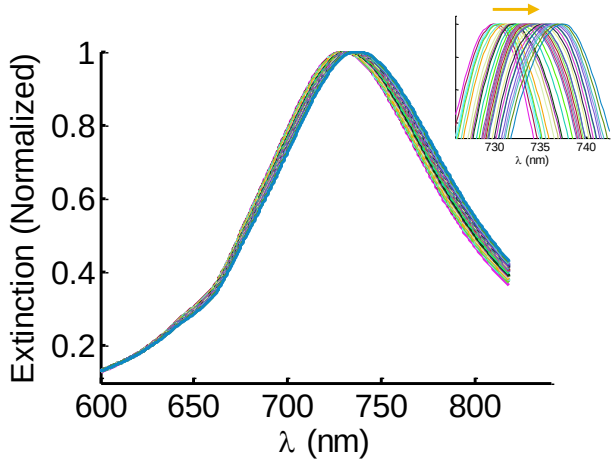


**Figure 23:** The extinction of AuNCs measured over time, as the NHS ester compound binds to AuNCs. The direction of the progress of the LSPR mode wavelength over time is indicated by an arrow on the Figure.

The location of the LSPR peaks is plotted versus time in Figure 24, where the binding kinetics can be easily measured. The curve fitting to the measurement data suggests that the binding of NHS ester compound to the surface of AuNCs follows a first order exponential bahavior with a rate constant of $4.16 \times 10^{-4}\ s^{-1}$. It can be seen that after about 120 *min* the binding events reach equilibrium. Therefore, it is expected that $2 - 3$ *hour* incubation time would be enough to make sure that the glycan-NHS compound covers the surface of the AuNCs efficiently.

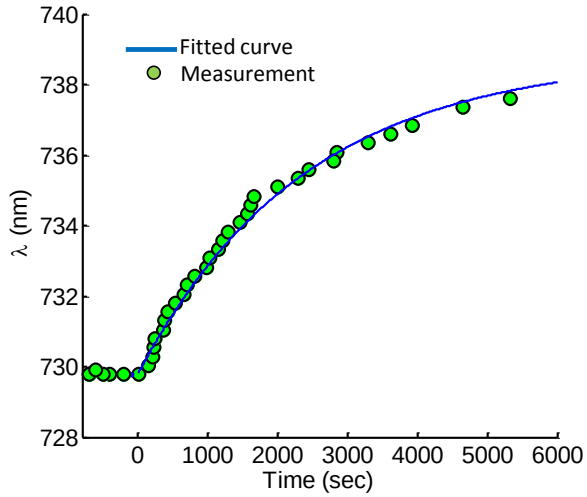


**Figure 24:** Kinetics of glycan-NHS compound binding to AuNCs.

The same procedure is then applied to the AuNCs assembled on the surface of a glass slide using the Langmuir-Blodgett technique. After the surface of the AuNCs is covered with a monolayer of glycans with high surface density, the sensor is ready to detect lectins/toxins bindings to glycans. Different glycans have specific affinities to certain toxins and lectins. Therefore, different spots on the sensor surface can be functionalized with different glycans to carry out multiplex sensing to detect multianalytes on the same chip. A fluorescence measurement is carried out to demonstrate the selectivity of glycans. A specific location of the sample is first coated with glycans using the procedure that was outlined earlier. Then the remaining NHS on the sample is blocked using ethanolamine solution. In the next step, biotinylated B-subunit of Cholera Toxin (CTB) is introduced to the sample, and is incubated for 1 *hour*. Then Streptavidin tagged with FITC dye is introduced to the sample. The sample is then washed thoroughly. The fluorescence microscope image in Figure 25 shows that in the regions where glycans exist, a large fluorescent emission can be observed. On the other hand, outside the glycan region, the fluorescent signal is very weak. This shows that the nonspecific binding is very minimal, and the tagged toxins mostly attach to the regions were there are glycan receptors.

The binding kinetic of the B-subunit of Cholera Toxin to the glycans is measured by monitoring the LSPR wavelength shift of assembled AuNCs on the surface of a glass slide. The location of the LSPR peak is plotted over time in Figure 26 after $\sim 10\ \mu M$ of CTB is introduced to the AuNC sample functionalized with GM1 glycans. It can be seen that in equilibrium, the LSPR wavelength shift is $\sim 16\ nm$. The CTB-GM1 binding on the surface of AuNCs exhibits a first order exponential behavior with a rate constant of $2 \times 10^{-3}\ s^{-1}$.

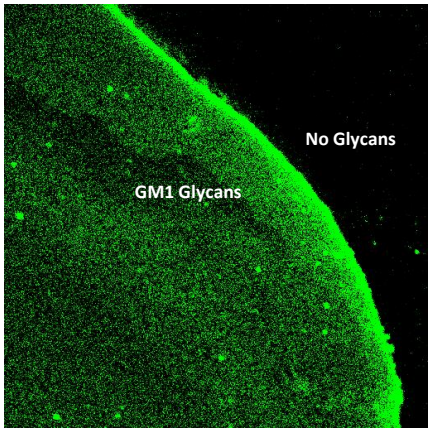


**Figure 25:** Fluorescent image of a spot on the AuNC sample functionalized with GM1 glycans. The tagged CTBs are only attached to the glycans and they are washed off the surface in the regions where there is no GM1 glycan.

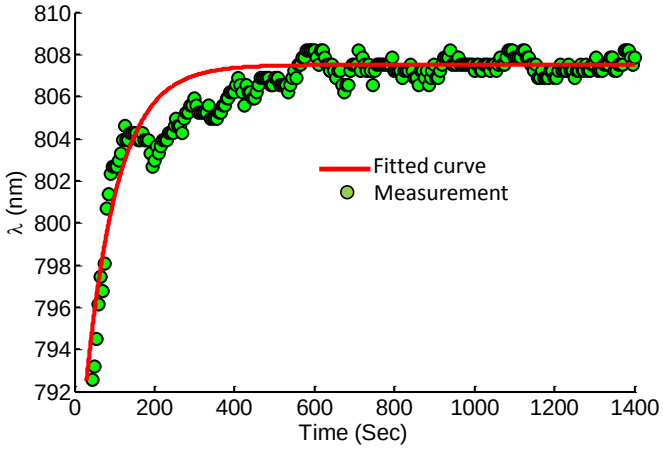


**Figure 26:** Binding kinetic of B-subunit of Cholera toxin (CTB) at 10 $\mu M$ concentration to GM1 glycan.

Plasmonic nanoresonators with their large sensitivities can be used for efficient LSPR sensing. The surface of plasmonic nanoresonators can be functionalized with different receptors to detect different analytes. We demonstrated the detection of CTB binding to GM1 glycans. Different types of glycans can be used to functionalize the surface of the chip at different spots to achieve multiplex multi-analyte sensing. These sensors with their large sensitivities can be used for the real-time monitoring of molecular bindings.

# CHAPTER III

# HYBRID PLASMONIC-PHOTONIC WAVEGUIDE STRUCTURES

Hybrid Plasmonic-photonic structures that consist of photonic waveguides and plasmonic structures are introduced in this chapter. The analysis, design procedure, and applications will be discussed. First, the structures consisting of a ridge waveguide and plasmonic nanoresonators will be discussed. In this type of hybrid structure, photonic guided modes are coupled to localized surface plasmon resonance (LSPR) modes of plasmonic nanoresonators. Second, hybrid structures consisting of plasmonic waveguides supporting propagating surface plasmon polaritons coupled to photonic waveguides will be discussed.

## *3.1 Plasmonic Nanoresonators Integrated with Photonic Waveguides*

In this section, a hybrid integrated plasmonic-photonic waveguide structure is demonstrated in which on-chip ridge waveguides are used to vertically couple the lightwave to LSPR modes of plasmonic nanoresonators. Individual or arrays of nanoparticles can be integrated with each ridge waveguide. The excitation of plasmonic nanoparticles in this hybrid device platform is alignment insensitive, and does not require bulky free-space optics with stringent requirements on the alignment. Plasmonic nanoresonators are integrated with photonic ridge waveguides, and coupling of light to the ridge waveguide guarantees the coupling of light to the intended plasmonic nanoresonators. Only plasmonic gold nanorods are considered here, since the LSPR wavelengths of nanorods can be easily tuned

by changing the dimensions, and also large field enhancements can be achieved at the two ends of nanorods [80]. Similarly, other types of plasmonic nanoparticles such as nanodisks, nanocubes, or dimer nanoantennas can be used in this hybrid device architecture. The proposed hybrid device structure can be combined with different integrated photonic structures such as multiplexers and demultiplexers to realize a fully functional multi-analyte multiplex on-chip sensor.

The schematic of the hybrid plasmonic-photonic structure consisting of a silicon nitride ($Si_3N_4$) ridge waveguide integrated with a gold nanorod on top is shown in Figure 27.

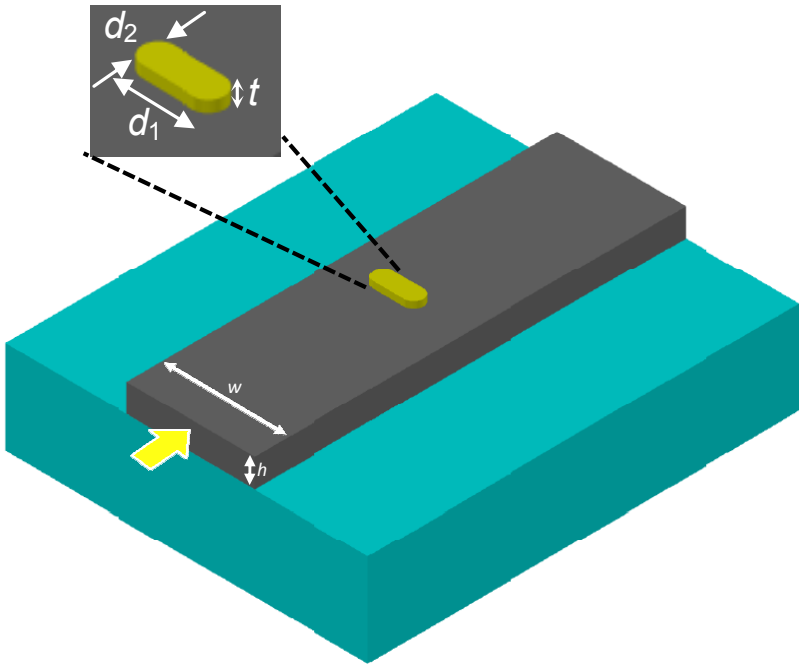


**Figure 27:** Schematic of the hybrid plasmonic-photonic structure consisting of a ridge waveguide integrated with a plasmonic nanoresonator. The evanescent tail of the guided mode can excite the LSPR mode of the plasmonic nanoresonator.

The substrate is silicon dioxide ($SiO_2$). The photonic waveguide with a cross section of ($w \times h$) supports a transverse electric (TE-like) mode over a spectral range that covers the resonance of the plasmonic nanoresonator. The ridge waveguide carries the light and the evanescent tail of the guided mode excites

the plasmonic nanoresonator mode. The plasmonic nanoresonator is assumed to be a gold nanorod with dimensions of $(d_1 \times d_2 \times t)$, where $t$ is the thickness of the gold nanorod. The radius of curvature of the nanorods is assumed to be half of its width, i.e., $(\frac{d_2}{2})$, which is the case according to our nanofabrication results. Although we have considered a gold nanorod as the plasmonic nanoresonator, other types of nanoparticles can also be used in the same hybrid structure, and the design, analysis, and implementation will follow the same procedure. Silicon nitride is considered as the material for ridge waveguide since it is transparent over a large spectral range from visible to infrared, and at the same time has a relatively large refractive index.

To analyze and design the structure shown in Figure 27, a model based on scattering analysis is employed [81]. Also, finite difference time domain analysis (FDTD) is used to numerically analyze the structure [69]. As shown in Figure 28, the hybrid structure consisting of a single nanoparticle vertically coupled to a ridge waveguide can be modeled as a standing wave resonator coupled to the waveguide.


**Figure 28:** Hybrid plasmonic-photonic structure can be modeled as a standing wave resonator coupled to a waveguide. Part of the incident power is coupled to the LSPR mode of the nanoresonator. The reflection, $R$, and the transmission, $T$, indicate the reflected and the transmitted power ratios in the waveguide.

Part of the incident wave is coupled to the LSPR mode of the nanoresonator; the rest is either reflected or transmitted through the waveguide. The reflected power ratio is indicated by $R$, the transmitted power ratio is indicated by $T$.

The plasmonic nanoresonator can localize the light energy resulting in a very large field enhancement in the near field region. Two major loss mechanisms cause the decay of the stored energy in the nanoresonator mode. Part of the stored energy is lost due to the internal metal material loss, and part of it is radiated either to the substrate or to the surrounding medium. These losses can be modeled by an intrinsic decay rate, i.e., $\Gamma_n^0 = \frac{1}{\tau_n^0}$, where $\tau_n^0$ is the intrinsic resonator photon lifetime. The internal loss resulting from material absorption, and also the radiative loss are proportional to the plasmonic nanoresonator field intensity. The plasmonic nanoresonator mode energy also decays because of the coupling of energy to the waveguide modes. The decay rate arising from the coupling to the backward wave in the waveguide is indicated here by $\Gamma_c^-$, and the decay rate due to the coupling of energy to the forward propagating wave in the waveguide is indicated by $\Gamma_c^+$. Using a scattering matrix analysis method [81], the reflection and the transmission can be obtained as,

$$|R|^2 = \frac{4\Gamma_c^+\Gamma_c^-}{(\omega - \omega_n)^2 + \Gamma_n^2}, \tag{2}$$

and

$$|T|^2 = \frac{(\omega - \omega_n)^2 + (2\Gamma_n - \Gamma_c^+)^2}{(\omega - \omega_n)^2 + \Gamma_n^2}, \tag{3}$$

respectively, where $\omega_n$ is the resonance frequency of the plasmonic nanoresonator and $\omega$ is the incident wave angular frequency, and $\Gamma_n = \Gamma_n^0 + \Gamma_c^+ + \Gamma_c^-$ is the total decay rate. The coupling efficiency is defined as the ratio of the incident power that is coupled to the plasmonic nanoresonator mode, and can be obtained as,

$$|k|^2 = 1 - R - T. \tag{4}$$

By substituting $R$ and $T$ from equations (1) and (2), the coupling efficiency can be obtained as,

$$|k|^2 = \frac{4\Gamma_n^0\Gamma_c^+}{(\omega - \omega_n)^2 + \Gamma_n^2}. \tag{5}$$

The goal is to maximize the coupling efficiency to deliver as much power as possible to the plasmonic nanoresonator mode. When the structure is symmetric, which is usually the case, the plasmonic nanoresonator mode will equally couple to the forward and backward propagating modes and $\Gamma_c^+ = \Gamma_c^-$. In this case, the coupling efficiency can be simplified as,

$$|k|^2 = \frac{4\Gamma_n^0 \Gamma_c}{(\omega - \omega_n)^2 + (\Gamma_n + 2\Gamma_c)^2}, \tag{6}$$

where $\Gamma_c = \Gamma_c^+ = \Gamma_c^-$ is the decay rate due to the coupling to the waveguide. It can be easily shown that the maximum coupling efficiency is 50% and this occurs at the resonance frequency when the decay rate due to the coupling is half of the intrinsic decay rate, i.e., $\Gamma_c = \frac{\Gamma_n^0}{2}$. The coupling decay rate, $\Gamma_c$, depends on the overlap of the waveguide field and the nanoresonator mode, which is determined by the distance between the waveguide and the nanoresonator and the waveguide dimensions. Since the coupling between the nanoresonator mode and the waveguide mode is strong and the plasmonic nanoresonator mode is strongly affected by the waveguide structure, a simple coupled mode analysis cannot reveal accurate results for the coupling of the waveguide and the nanoresonator modes. We use FDTD analysis to simulate the hybrid structure and optimize the coupling efficiency. To carry out the FDTD simulations, first finite element method (FEM) is used to obtain the mode of the waveguide at its cross section, then this mode is set as the source for FDTD simulations to analyze the time domain propagation. The fundamental TE-like mode of a $700nm \times 200nm$ $Si_3N_4$ ridge waveguide calculated using FEM is shown in Figure 29(a), and a snapshot of the time domain propagation of the waveguide mode (electric field profile) is shown in Figure 29(b).

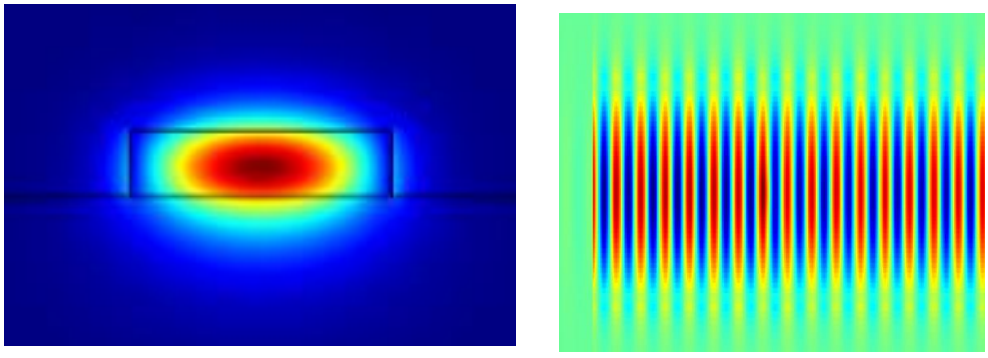

(a) (b)

**Figure 29:** (a) The fundamental TE-like mode of a $700nm \times 200nm$ $Si_3N_4$ ridge waveguide calculated using FEM and (b) A snapshot of the electric field profile of the time domain propagation of the waveguide mode calculated using FDTD.

As an example, a snapshot of the electric field intensity profile near a plasmonic nanorod with dimensions of $90nm \times 56nm \times 30nm$ integrated on a ridge waveguide with dimensions of $700nm \times 200nm$ at the resonance wavelength of $\lambda_0 = 731nm$ is plotted in Figure 30. The snapshot is taken halfway through the nanorod thickness, and it is normalized to the maximum field intensity in the same plane when there is no nanoresonator. It can be seen that the LSPR mode of the plasmonic nanorod on the waveguide is excited and the field intensity near the nanorod tips is highly enhanced.

For the FDTD simulation $3nm$ mesh sizse are used on the nanorod and $20nm$ mesh sizes are used for the waveguide region. The simulation time covers $200fs$ with $0.0054fs$ time steps, and the source is a $20fs$ pulse centered at $\lambda_0 = 740nm$. Perfectly matched layer (PML) boundary conditions are used for the outer boundaries of the simulation domain.

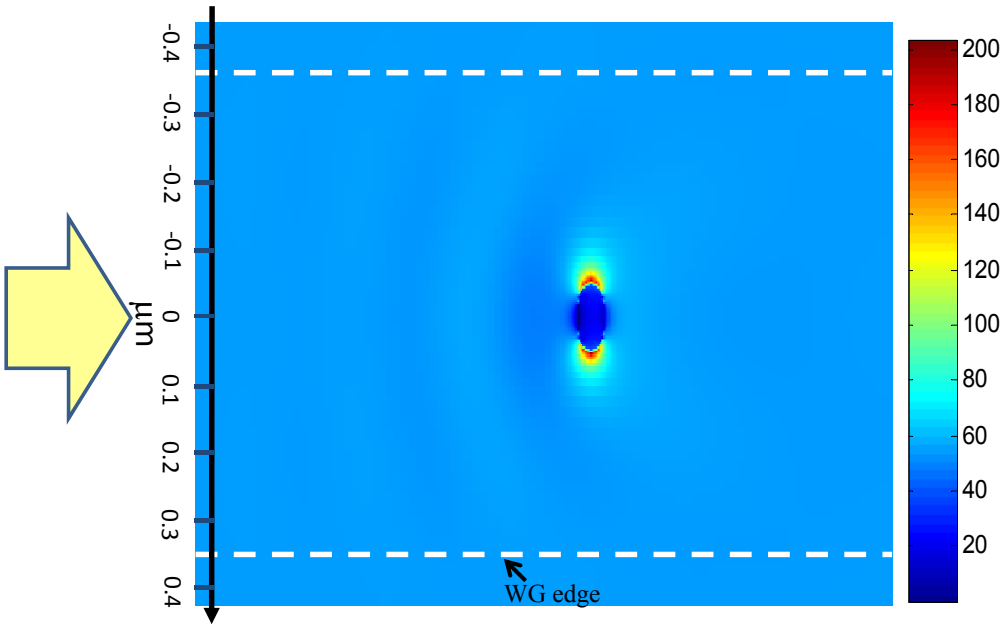


**Figure 30:** Electric field intensity profile near a plasmonic nanorod ($90nm \times 56nm \times 30nm$) integrated on a ridge waveguide ($700nm \times 200nm$) at the resonance wavelength of $\lambda_0 = 731nm$. The snapshot is taken at a height of $15nm$ from waveguide surface, halfway through the thickness of the gold nanorod.

In order to show the spectral response of the nanoresonators in the near field region, the electric field intensity spectrum is plotted in Figure 31, at a point that is $2nm$ away from the edge of the nanord and halfway through its thickness for three different nanorods, each one on a $700nm \times 200nm$ $Si_3N_4$ ridge waveguide. The point at which the field intensity is probed is indicated as point $P$ in the inset of Figure 31. In each case, the electric field intensity is normalized to the electric field intensity at the same location, point $P$, on a waveguide without a nanorod.

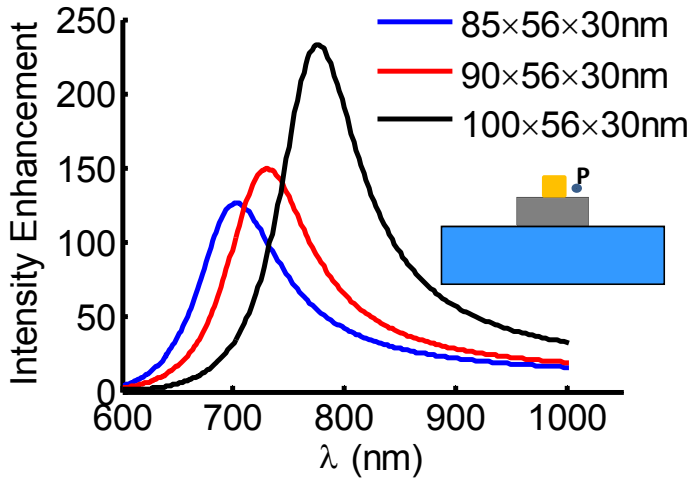


**Figure 31:** Electric field intensity spectrum probed at point $P$, $2nm$ away from the side of the nanorod and at a height of $15nm$ from the waveguide surface for three different gold nanorods, i.e., ($85nm \times 56nm \times 30nm$), ($90nm \times 56nm \times 30nm$), and ($100nm \times 56nm \times 30nm$), each one integrated on a ridge waveguide of dimensions ($700nm \times 200nm$).

It can be seen that each nanoresonator has a resonance peak at a resonance wavelength that increases as the aspect ratio $(\frac{Length}{Width})$ of the nanorod is increased. A large field intensity enhancement is observed near each nanorod tip.

The nanoresonator resonance can be observed as a drop in the transmission of the waveguide, and also as a peak in the reflection spectrum. At the resonance, part of the input power is coupled to the LSPR mode of the nanoresonator and the rest of it is either transmitted through the waveguide, or is reflected back toward the source. At the resonance, the extinction cross section is maximum, which means that the sum of absorption and the scattering cross sections are maximum. Therefore, the nanoresonator acts as a stronger perturbation and the reflection is large. The reflection and the transmission spectrum for the three previously mentioned structures are plotted in Figure 32(a) and Figure 32(b), respectively.

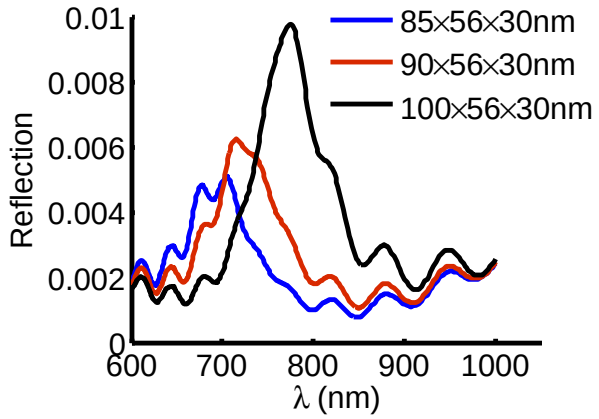


(a)

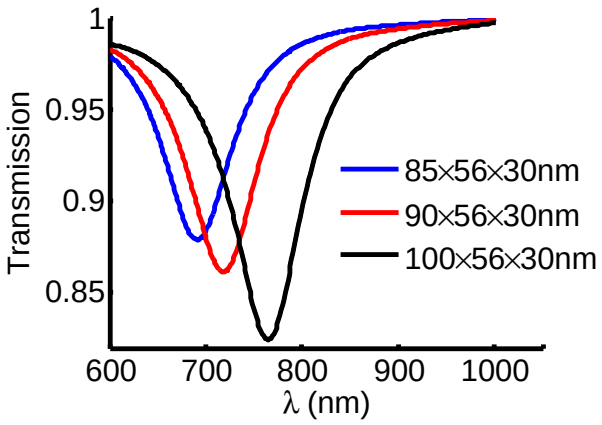


(b)

**Figure 32:** (a) Reflection and (b) Transmission spectra of a waveguide (750 $nm \times 200\ nm$) integrated with a gold nanorod. Blue curves show the results for a (85 $nm \times 56\ nm \times 30\ nm$) nanorod. Red curves show the results for a (90 $nm \times 56\ nm \times 30\ nm$) nanorod. Red curves show the results for a (100 $nm \times 56\ nm \times 30\ nm$) nanorod.

It can be seen that in each case, the transmission shows a drop near the resonance of the nanorod, and the reflection has a peak. The reflection at the resonance is less than 1% in each case. The oscillations in the reflection spectra are due to interference effects. In each case, the maximum extinction at the output of the waveguide is much larger than the reflection peak. The difference is the amount of power that is coupled to the LSPR mode of the nanorod. The coupling efficiency spectrum, which is defined in Equation 4, can

be obtained from the difference between the normalized incident power and the reflection and the transmission. The coupling efficiency spectrum for the three hybrid structures discussed in Figure 31 is shown in Figure 33. The coupling efficiency has a resonance peak at the resonance wavelength of each plasmonic nanoresonator. The maximum coupling efficiency can be as high as 16.6% for a (100 $nm \times 56\ nm \times 30\ nm$) gold nanorod integrated on a ridge waveguide of dimensions (700 $nm \times 200\ nm$), which means that about 16.6% of the input power is coupled to the LSPR mode of the plasmonic nanoresonator.

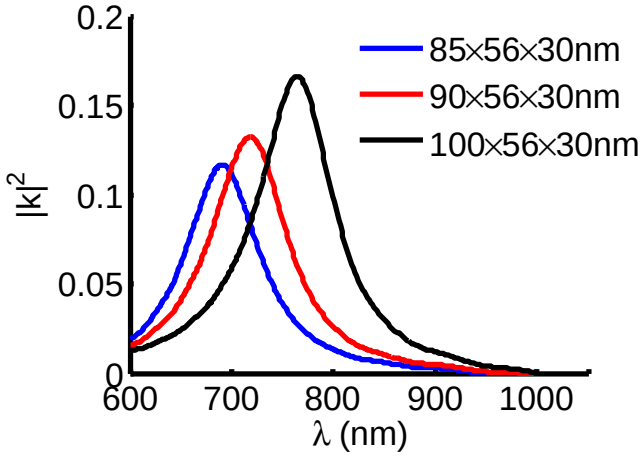


**Figure 33:** Coupling efficiency spectrum for three different gold nanorods, i.e., (85 $nm \times 56\ nm \times 30\ nm$), (90 $nm \times 56\ nm \times 30\ nm$), and (100 $nm \times 56\ nm \times 30\ nm$), each one integrated on a ridge waveguide of dimensions (700 $nm \times 200\ nm$).

As discussed earlier, part of this coupled power is absorbed by the nanoresonator, and part of it is scattered out by the nanoresonator. The ratio of the absorption to the scattering depends on the nanoresonator design, and depending on the application, either more absorptive nanoresonators or more scattering ones might be of interest.

By using Equation 4 to obtain the coupling efficiency, it is assumed that the portion of input power that is neither transmitted through the waveguide, nor reflected through the waveguide is in fact coupled to the LSPR mode of the

nanoresonator. This assumption implicitly implies that the input light is not scattered or reflected from the plasmonic nanoresonator merely because it is a perturbation. This indeed is the case. From the transmission and the reflection spectra shown in Figure 32(a) and Figure 32(b), we can see that far from the resonances the effect of the plasmonic nanoresonators as simple perturbation sites is negligible. For example, at the wavelength of $\lambda_0 = 1000\ nm$, the transmission is more than 99% and the reflection is less than 0.25% for a ($85\ nm \times 56\ nm \times 30\ nm$) gold nanorod integrated on a ridge waveguide of dimensions ($700\ nm \times 200\ nm$). At the resonance, the same structure exhibits a transmission of 88% and a reflection of about 0.4%.

The coupling efficiency depends on the overlap of the waveguide and the nanoresonator modes. The dimensions of the waveguide and the distance between the waveguide and the nanoresonator can be optimized to maximize the coupling efficiency. If the nanoresonator distance from the waveguide surface is increased, the coupling efficiency is decreased, because the overlap of the waveguide and the nanoresonator fields is decreased. If the waveguide dimensions (width and height) are decreased, then the waveguide fields spread more outside the waveguide core and overlap more strongly with the nanoresonator LSPR mode. The height of the waveguide is assumed to be fixed at $h = 200\ nm$. In practice, the waveguide height is usually fixed by the $Si_3N_4$ layer thickness, determined based on different considerations throughout the wafer, and locally changing it is cumbersome in the fabrication process. Therefore, the optimization strategy is to maximize the coupling efficiency for a fixed waveguide thickness. The coupling efficiency for a hybrid structure consisting of a gold nanorod ($100\ nm \times 56\ nm \times 30\ nm$) and a waveguide with a height of $200\ nm$ is plotted in Figure 34 versus the waveguide width.

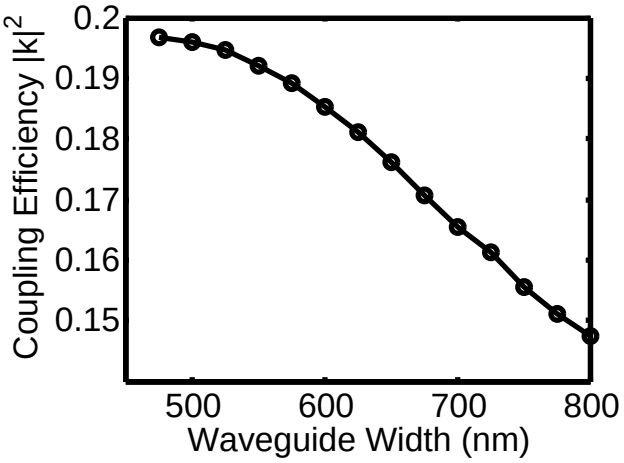


**Figure 34:** Coupling efficiency versus waveguide width for a hybrid structure consisting of a gold nanorods (100 $nm \times 56\ nm \times 30\ nm$) integrated on a ridge waveguide with a height of 200 $nm$.

It can be seen that as the waveguide width is decreased, the coupling efficiency is increased. However, it should be noted that the waveguide width cannot be decreased below $w = 350\ nm$ since the waveguide mode cuts off. As the waveguide width is decreased, the mode extends more outside of the waveguide and feels side walls more strongly. In practice, when the waveguide side walls have surface roughness arising from fabrication imperfections, the propagation loss is increased. Therefore, a reasonable value should be chosen for the waveguide width to maximize the coupling efficiency and minimize the propagation loss. The large coupling efficiency of 16.6% to a single (100 $nm \times 56\ nm \times 30\ nm$) gold nanorod integrated in the proposed hybrid structure is about two orders of magnitude larger than the coupling efficiency when the plasmonic nanoparticle is excited using a condensing lens. The extinction cross section of such a gold nanorod is extremely small ( $10^{-14} m^2$), and only a small fraction ( 0.1%)of the input optical power focused by a lens can be coupled to the LSPR mode of the plasmonic nanoresonator. In our hybrid structure, the coupling between the waveguide mode and the LSPR mode of the nanoresonator can be optimized so that the maximum

power is coupled from the waveguide to the nanoresonator. It was shown that using this architecture the maximum coupling efficiency is 50%. Our simulation results revealed that under practical conditions, coupling efficiencies on the order of $10 - 20\%$ are possible. using the proposed structure, single nanoresonator interrogation can be made possible. This is very important for the fundamental study of single nanoresonators without the ensemble broadening effects, and also is very important from application point of view, since individual or a few number of plasmonic nanoresonators can be used for on-chip sensing and spectroscopy.

## *3.2 Surface Plasmon Polariton Waveguides Integrated with Photonic Waveguides*

A hybrid integrated plasmonic-photonic waveguide structure is introduced in this section, which consists of on-chip photonic ridge waveguides integrated with surface plasmon polariton (SPP) waveguides. In this structure, lightwave propagates through the photonic waveguide, and is then vertically coupled to the SPP mode of a plasmonic strip waveguide integrated on top of the photonic waveguide. Plasmonic strip waveguides can provide a very compact means of propagation of light on a chip. The size of the strip waveguides can be subwavelength, and they can be densely integrated [49]. Because of the very small size of these waveguides, they have the potential of being interfaced with electronics to make very efficient and compact interconnects. On the other hand these plasmonic strip waveguides can be interfaced with photonic structures, and therefore, they can bridge the gap between the electronics world and the photonics world [39]. These waveguides support enhanced localized surface waves at the metal surface. Therefore, they can be used to enhance light-matter interaction in applications such as sensing and optical modulation. Moreover, these SPP waveguides can be coupled together laterally to form slot waveguides [41]. In this

case, the field inside the slot region is highly enhanced. As discussed in section 1.3, some recent efforts are focused on making plasmonic circuits using propagating SPPs in the form of waveguides and microresonators [42]. Plasmonic waveguides suffer from large propagation loss and the propagation distance is on the order of a few micrometers. Although long-range SPP waveguides have been proposed with propagation distances on the order of a few hundred micrometers, still the propagation loss of these structures prevents them to be suitable for making a fully plasmonic platform [44].

Here, a hybrid platform is proposed in which a photonic backbone is used to steer the lightwave on the chip with a low propagation loss. Then, the lightwave is vertically coupled to the SPP waveguide mode at the site of interest. This way, the plasmonic waveguides do not need to be long to cover the whole chip, and they are used wherever they are needed. Enhanced localized propagating SPPs are excited on the chip and enhanced light-matter interaction is then possible. A schematic of the hybrid waveguide structure is shown in Figure 35. It consists of a silicon nitride ($Si_3N_4$) ridge waveguide core, a silicon dioxide ($SiO_2$) buffer layer, a metal strip, and a cladding layer. The metal strip can be gold, silver, or any other material that can support SPPs. The cladding layer can itself be the material of interest, which is intended to interact with the lightwave, or it can be a host material for the interacting material. For example, in sensing applications, the cladding layer can be a porous material in which target molecules can penetrate.

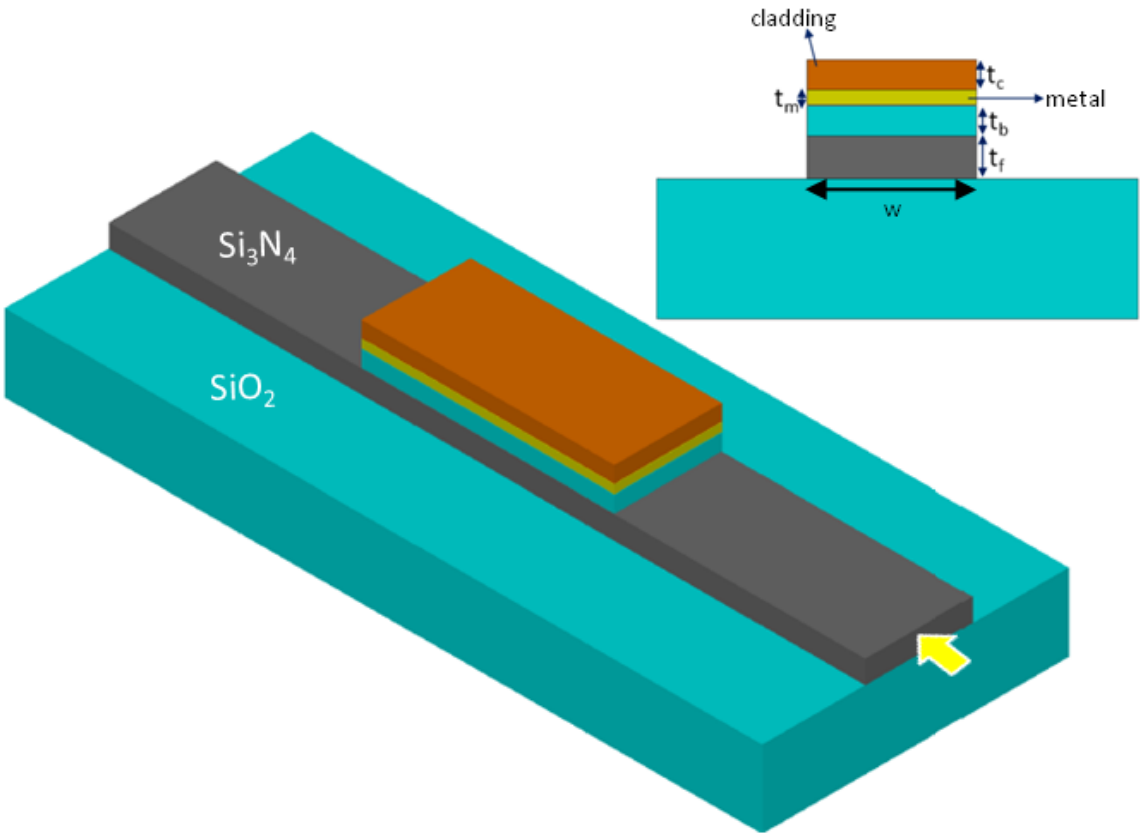


**Figure 35:** 3D schematic of a hybrid SPP waveguide consisting of a photonic ridge waveguide and a plasmonic strip waveguide. The inset shows a cross section of the hybrid structure consisting of a photonic ridge waveguide vertically coupled to a plasmonic strip waveguide. These two waveguides are separated by a $SiO_2$ buffer layer. The cladding layer is where strong light-matter interaction occurs. In this structure, $t_f$ is the photonic core film thickness, $t_b$ is the buffer layer thickness, $t_c$ is the cladding layer thickness, $t_m$ is the buffer layer thickness, and $w$ is the waveguide width.

This hybrid structure can be designed in such a way that the propagation wavevector, $\beta$, in the $Si_3N_4$ waveguide can provide the required momentum, $K_{sp}$, to excite SPPs at the interface of the metal and the cladding layer. As shown in Figure 36, SPPs are traditionally excited using prisms that can provide the necessary momentum, $K_{sp}$, at the wavelength of interest. It should be noted that direct excitation of SPPs at the metal-dielectric interface is not possible since the in-plane momentum of SPPs, $K_{sp}$, is larger than that of the surrounding dielectric medium, and the necessary condition of momentum matching cannot be directly

satisfied. The prism in the Kretschmann configuration [82], Figure 36(a), or in the Otto configuration [83], Figure 36(b), helps with satisfying the momentum matching condition.

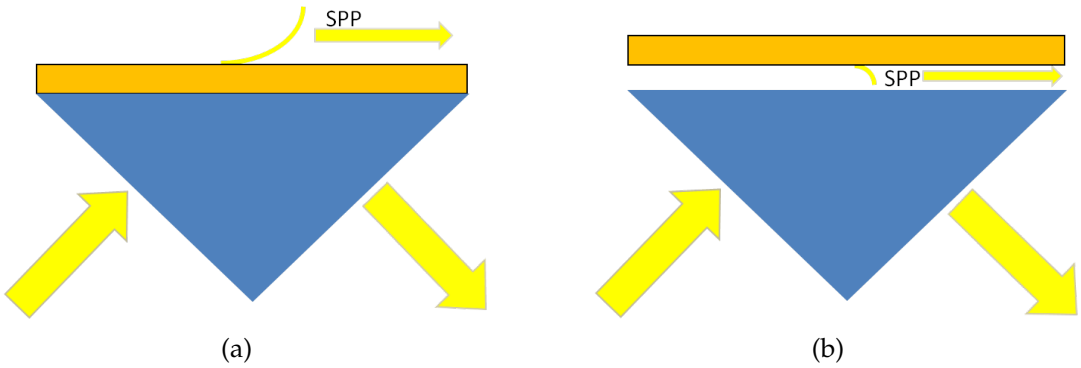


**Figure 36:** Excitation of SPPs using a prism that provides the required momentum, $K_{sp}$, (a) in the Kretschmann configuration (b) in the Otto configuration.

In the hybrid structure, the photonic waveguide has the role of a prism to excite propagating SPPs along the metal strip. When the buffer layer is thick, the metal strip and the photonic waveguide have their own separate modes. As the buffer layer thickness is decreased, the two photonic and plasmonic modes are coupled to each other, and they form two supermodes. The photonic waveguide width is chosen so that the waveguide has a single mode for each polarization at the wavelength of interest. The polarization of interest for the hybrid structure is TM-like with the principal magnetic field component along the $x$ axis. The TM-like mode has the SPP mode component at the interface of the metal and the cladding layer.

To analyze and design the hybrid waveguide structure, finite element method (FEM) [84] is used to obtain the eigenmodes at each wavelength. Maxwell's equations are solved for transverse components of electric and magnetic fields in the plane of the waveguide cross section. The metal layer dispersion is considered through the method outlined in Appendix B. As an example, a hybrid waveguide structure with dimensions of $w = 400\ nm$, $t_f = 200\ nm$, $t_b = 120\ nm$, and $t_m = 50\ nm$

is analyzed at a wavelength of $\lambda = 650\ nm$. The photonic core is assumed to be $Si_3N_4$ with a refractive index of $n = 2$, the buffer layer is assumed to be $SiO_2$ with a refractive index of $n = 1.444$, and the cladding is assumed to be porous alumina ($p - Al_2O_3$) with a refractive index of $n = 1.59$. The transverse magnetic field component along $x$ direction, $H_x$, for the two supermodes of this structure is plotted in Figure 37(a) and Figure 37(b). One of these modes, Figure 37(a), has an effective index of $n_{eff} = 1.616 - j0.0017$ and the other one, Figure 37(b) has an effective index of $n_{eff} = 1.722 - j0.0052$. It can be seen that the two supermodes have opposite symmetry.

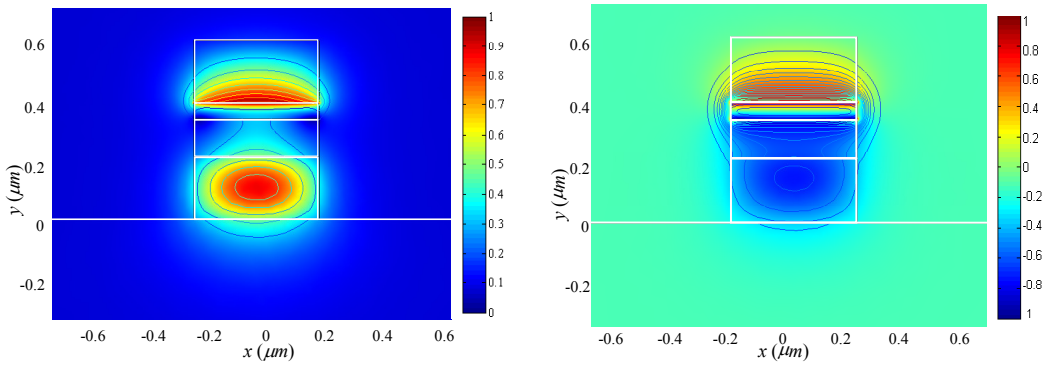


(a) (b)

**Figure 37:** Profile of the transverse magnetic field, $H_x$, for a hybrid plasmonic-photonic waveguide structure with $w = 400\ nm$, $t_f = 200\ nm$, and $t_b = 120\ nm$ at a wavelength of $\lambda = 650\ nm$. The photonic waveguide is $Si_3N_4$ with a refractive index of $n = 2$, the buffer layer is $SiO_2$ with a refractive index of $n = 1.444$, and the cladding is assumed to be porous alumina ($p - Al_2O_3$) with a refractive index of $n = 1.59$.

The dispersion of the hybrid structure with the aforementioned parameters is plotted in Figure 38 as the real part of the effective index versus wavelength, which has two branches corresponding to the two supermodes. At each wavelength, one of these modes has a lower effective index and the other one has a higher effective index. The imaginary part of the effective index, which accounts for the propagation loss, follows the same trend. Therefore, by strongly coupling the plasmonic and the photonic modes, mode splitting occurs, and as a result the lower

branch mode will have lower propagation loss. Therefore, the lower branch mode is of more interest for practical applications. The mode profile of the lower branch supermode at a wavelength of $\lambda = 650nm$, Figure 37(a), shows that the SPP mode at the metal-cladding interface is effectively excited. Thus, light-matter interaction in the cladding region is enhanced.

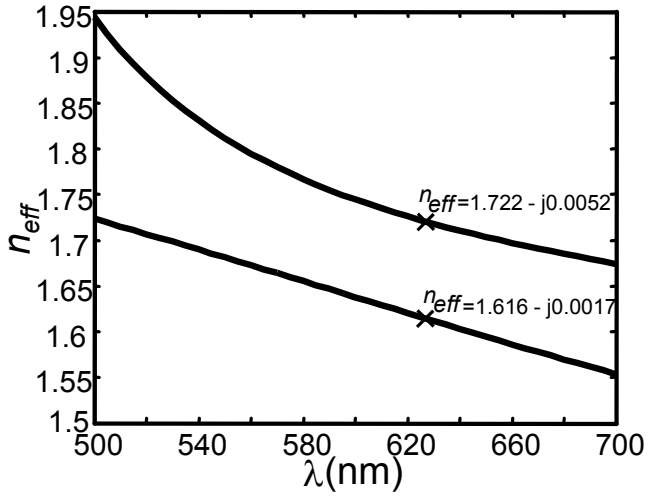


**Figure 38:** Dispersion of the two supermodes of the hybrid SPP waveguide structure. Only the real parts of the effective indices are plotted versus wavelength. The dispersion has two branches resulting from the splitting of the two photonic and plasmonic modes. All the parameters are the same as those used in Figure 37.

## *3.3 On-chip Sensing using Hybrid Plasmonic-photonic Waveguides*

In this section, the application of plasmonic-photonic waveguide-based devices for on-chip sensing is discussed. The device introduced in section 3.1 consisting of a waveguide integrated with plasmonic nanoresonators can be used as a broadband refractive index sensor. Plasmonic LSPR modes are very sensitive to the local environment surrounding the nanoparticles. When the refractive index of the surrounding environment is changed, the LSPR mode is shifted as shown schematically in Figure 39. This is the basis of LSPR sensing, where the refractive

index change and consequently the concentration of the target analyte can be inferred from the amount of resonance shift.

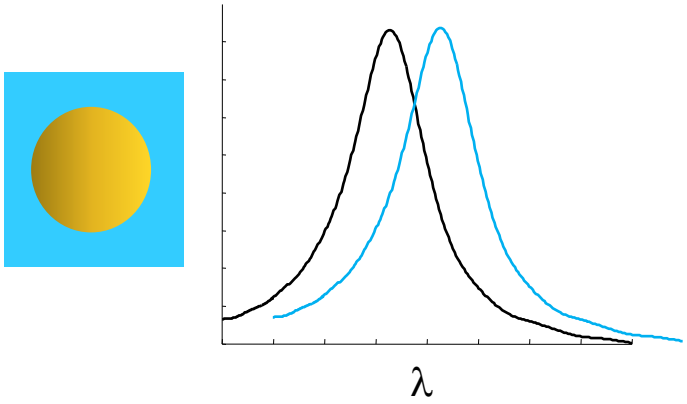


**Figure 39:** Schematic illustration of LSPR sensing concept. When the local environment surrounding a plasmonic nanoparticle changes, the LSPR mode shifts.

This refractive index-based sensing mechanism is very sensitive, and only a very small amount of analyte is required to cause the local refractive index change. The LSPR sensing can be potentially very fast, and capable of resolving fast binding kinetics. This sensing mechanism, like other refractive index based sensing methods, does not provide an inherent specificity, since different materials that introduce the same refractive index change, cause the same amount of shift in the LSPR mode, and cannot be distinguished from each other. To address the specificity issue, the surface of the plasmonic nanoresonators can be functionalized with different specific receptors to bind to specific target molecules. This way, different binding interactions can even be dynamically detected. The LSPR sensing has been used for the detection of different biomolecules and chemicals [85–87]. Using this method, different interactions such as antibody-antigen, biotin-Streptavidin, and aptamer-protein bindings have been detected [86, 87]. Different types of plasmonic nanoresonators have been used for LSPR sensing, either in

solution or dispersed or fabricated on substrates [87]. Since the coupling of light to the localized modes of individual plasmonic nanoresonators is very weak, usually an ensemble of these nanoparticles are interrogated.

In any refractive index sensing scenario based on a resonance shift, the detection limit, defined as the minimum amount of detectable analyte, depends on the sensitivity, resonance linewidth, and the signal-to-noise-ratio (SNR) [1]. The sensitivity, defined as the shift of resonance for a unit change of refractive index, is desired to be as large as possible. The linewidth of the resonance is desired to be as narrow as possible, and the SNR is desired to be as large as possible. The sensitivity and the linewidth are mostly determined by the design of the nanoparticle, and the SNR depends on the excitation coupling efficiency as well as the detection mechanism [88, 89].

Interrogation of single or a few number of plasmonic nanoparticles has always been of great interest in LSPR sensing, since the sensing volume, and consequently the required amount of analyte would extremely be small [90–92]. However, the coupling of light to the LSPR modes of individual plasmonic nanoparticles is not efficient in conventional free-space excitation using an objective lens. It has been shown that individual silver and gold nanoparticles can be used for LSPR sensing to detect low concentration analytes [90, 91]. Scattering spectrum of single nanoparticles is measured using darkfield microscopes equipped with cooled CCD detector spectrographs, and the shift of scattering resonance is monitored as a measure of the change of surrounding medium refractive index [90, 91]. It was shown in section 3.1 that by using our hybrid waveguide structure consisting of a plasmoniic nanoresonator and a ridge waveguide, a large coupling efficiency is possible for the excitation of the LSPR mode of plasmonic nanoparticles. Uisng this structure, LSPR sensing can be done with a single or only a few plasmonic nanoresonators. When target molecules are attached to the surface of

the plasmonic nanoresonators on top of the photonic waveguide (Figure 40), the refractive index of the environment surrounding the nanoresonator is changed. Consequently, the resonance wavelength of the plasmonic nanoresonators is shifted. By monitoring this resonance shift, the refractive index change, and consequently the concentration or mass of the target analyte can be determined.

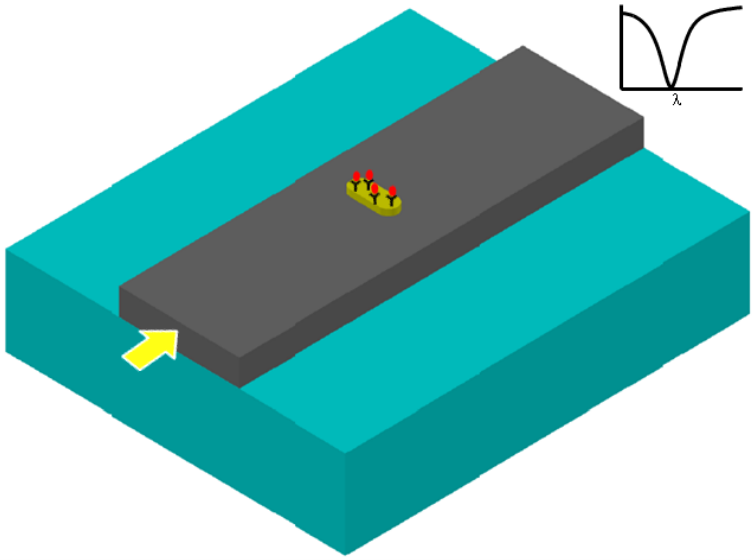


**Figure 40:** Schematic of a hybrid plasmonic-photonic waveguide sensor, consisting of a plasmonic nanorod integrated with a photonic waveguide. The receptors and the target molecules attached to them are schematically shown on top of the plasmonic nanoresonator.

As an example, the transmission spectrum calculated using FDTD analysis is shown in Figure 41, for three different cladding layers with different refractive indexes of ($n_c = 1.35$) and ($n_c = 1.36$) and ($n_c = 1.375$). The resonance redshifts as the cladding refractive index is increased. An advantage of the proposed hybrid structure over the conventional method of plasmonic nanoresonator interrogation using bulky microscopes is the fact that the resonance and its shift is monitored in the transmission spectrum of the waveguide, which makes the detection mechanism simpler and less alignment sensitive.

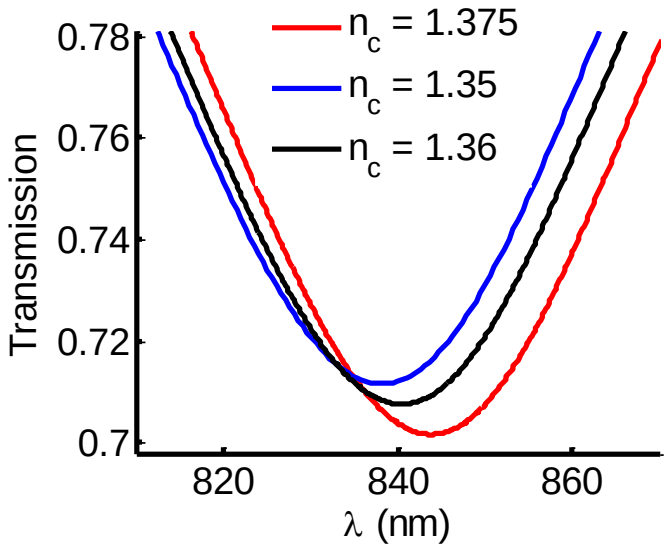


**Figure 41:** The transmission spectrum showing the LSPR mode of a single gold nanorod ($100nm \times 56nm \times 30nm$), on a $Si_3N_4$ ridge waveguide ($700nm \times 200nm$), for three different cladding refractive indexes of $n_c = 1.35$, and $n_c = 1.36$, and $n_c = 1.375$, where the LSPR wavelength redshifts as the refractive index is increased.

It can be seen that the extinction is about 30%. By using an array of plasmonic nanoresonators, the extinction can be further increased. If the plasmonic nanoresonators are identical and far enough from each other, the extinction of an array of plasmonic nanoparticles can be estimated to be $(1-x)^N$, where $x$ is the extinction of a single plasmonic nanoresonator, and $N$ is the number of plasmonic nanoresonators on a waveguide. Although increasing of the extinction by using an array of nanoresonators results in larger signal-to-noise ratio ($SNR$), the required amount of analyte is larger for an array of plasmonic nanoresonators, compared to a single nanoresonator. This sensor has many advantages. First, since the coupling efficiency and consequently the SNR is very large, low detection limits are possible, and the sensor can operate very fast by using room-temperature detectors. Second, since the sensing area is very small, the amount of required target analyte for sensing is very minimal. Therefore, sample preparation can be done very fast. Third, the resonance shift is measured in the waveguide output spectrum. Therefore, in contrast to conventional plasmonic nanoparticle-based

LSPR sensors, there is no need for precisely locating and imaging of individual nanoparticles [90] using bulky microscopes, and the resonance is manifested in the waveguide output. Fourth, since the sensor is very compact, an array of these hybrid waveguide-based sensors can be used in series or in parallel on the same chip with different plasmonic nanoresonators, each one with a different LSPR wavelength, for multiplex sensing. It should be noted that refractive index sensing is inherently a non-specific sensing mechanism, and two different target molecules that cause the same change of refractive index, cannot be distinguished from each other. To overcome this issue, specific surface coatings are usually used in refractive index sensors that specifically bind to the target molecules of interest [1,16]. Since the hybrid waveguide-based sensor is very compact, different surface coatings can be used for different hybrid sensor structures to realize multi-analyte sensing on a single chip.

The sensitivity, $S$, for the proposed refractive index sensor is defined as the rate of change of the resonance wavelength with respect to the change of the cladding refractive index. Figure 42 shows the LSPR wavelength versus the cladding refractive index change for a hybrid plasmonic-photonic sensor consisting of a $Si_3N_4$ ridge waveguide ($700nm \times 200nm$) integrated with a single plasmonic nanorod ($100nm \times 56nm \times 30nm$). The slope of the linear fit to the results of Figure 42 is the sensitivity of the sensor, which is equal to $S = 219.04 \frac{nm}{RIU}$, where RIU stands for refractive index unit. This sensitivity, which is obtained here in an integrated hybrid plasmonic-photonic device, is comparable to the sensitivity reported in literature for individual plasmonic nanoparticle LSPR-based sensors [90].

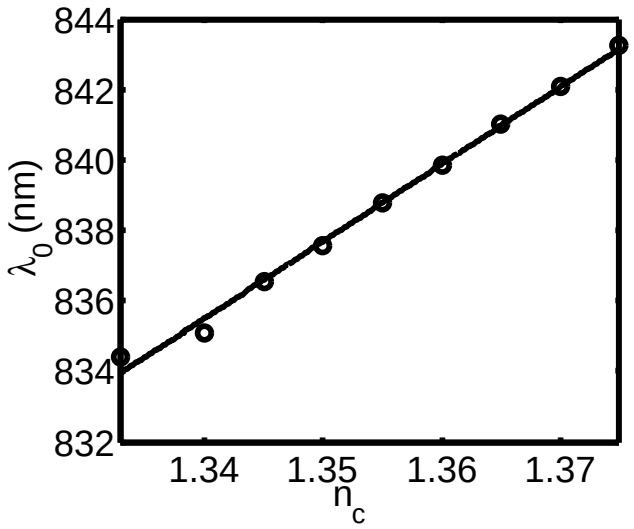


**Figure 42:** Resonance wavelength versus the change of cladding refractive index for a hybrid waveguide-based structure consisting of a $Si_3N_4$ ridge waveguide ($700nm \times 200nm$) and a single plasmonic nanorod ($100nm \times 56nm \times 30nm$). The sensitivity is the slope of the linear fit, and is obtained as $S = 219.04 \frac{nm}{RIU}$.

The hybrid sensor has a relatively wide resonance linewidth with a full width at half maximum (FWHM) of $\sim 92nm$. Therefore, it has a large spectral efficiency when used with a wideband source such as a light emitting diode (LED). In contrast to other refractive index sensors that rely on resonance shift of very high-Q resonance features, the hybrid sensor introduced here is less sensitive to environmental changes, such as temperature drifts. Besides the simplicity of the system and the spectral efficiency, by using a wideband source instead of a tunable laser source, the output spectrum can be monitored in real-time when the sensor is integrated with aspectrometer , eliminating the need for repeatedly scanning the spectrum. This makes the study of fast kinetic changes possible. Since the hybrid structure is very compact and can be realized on a chip, it has the potential of integration with micro-spectrometers [59] on the same chip, and therefore a very compact, unified, and fully functional on-chip sensor can be realized .

# CHAPTER IV

# EXPERIMENTAL DEMONSTRATION OF HYBRID PLASMONIC-PHOTONIC WAVEGUIDE STRUCTURES

In this chapter, the experimental demonstration of the hybrid plasmonic-photonic structures introduced in chapter 3, consisting of plasmonic nanoresonators and $Si_3N_4$ ridge waveguides are discussed. First, we will outline the fabrication procedure. Next, the characterization will be discussed, where the details of an in-plane characterization setup that was put together for this purpose will be discussed. Then the application of the hybrid waveguide-based structure for sensing will be demonstrated experimentally.

## *4.1 Fabrication of Hybrid Plasmonic-photonic Waveguide Structures*

In this section, the fabrication procedure for the hybrid plasmonic-photonic waveguides introduced in chapter 3 is discussed. Such devices consist of a photonic part and a plasmonic part. Therefore, the fabrication procedure consists of two major steps of fabricating the photonic structures, and fabricating the plasmonic structures. Since most of the devices of interest here are designed for applications in the visible or near infrared range of the spectrum, $Si_3N_4$ is used as the material for photonic devices. As discussed previously, $Si_3N_4$ is transparent over a wide range of wavelengths (from UV to infrared), and has a relatively large refractive index, and the fabrication of devices in $Si_3N_4$ is feasible. For applications in the infrared range of the spectrum, $Si$ can also be used, which has higher refractive index, and therefore, provides more confinement. Here, the detailed

procedure for fabrication of $Si_3N_4$-based devices will be explained.

The fabrication procedure starts with a wafer consisting of three layers, a 500 $nm$ thick $Si$ handle layer, a 4$\mu m$ $SiO_2$ insulating layer, and a 200 $nm$ $Si_3N_4$ film. We purchase these wafers from outside companies and then the fabrication procedure is done here at Georgia Tech Nanotechnology Research Center (NRC) cleanroom facilities. The three-layer wafer is ordered from either Rogue Valley Microdevices or LioNix. The wafers are prepared starting from a 500 $nm$ thick premium p-doped $Si$ wafer with 100 orientation. A 4 $\mu m$ thermal oxide is then grown on the substrate at a temperature of $1000^{\circ}C$, which consumes about 1.84 $\mu m$ of the $Si$ layer. Finally, 200 $nm$ stoichiometric silicon nitride is deposited using low pressure chemical vapor deposition (LPCVD) method. The ellipsometry measurements reveals that the refractive index of the $Si_3N_4$ film is $n = 2.0127$ and the average thickness measured for 3 different wafers purchased from Lionix is 195 $nm$. The thickness variation of the $Si_3N_4$ wafers is measured using an ellipsometer, and the variation is always less than 4 % across the wafer. As an example, the height map is shown Figure 43 for a typical wafer. The average thickness of the $Si_3N_4$ film is obtained as 199.05 $nm$.

The photonic devices are made in the $Si_3N_4$ film, and the buried oxide (BOX) layer acts as an insulator. The substrate is cleaned using standard procedures, and then the fabrication process is started. Generally, the fabrication procedure consists of two steps of electron beam lithography (EBL), one for defining the photonic structure patterns and the other for defining the plasmonic structures. The alignment between the two steps of lithography is critical to minimize any registration errors. We fabricate the devices on small pieces ( 1000 $mm \times 4000$ $mm$) that we cut from the wafer. Therefore, the thickness is very uniform on such a small piece.

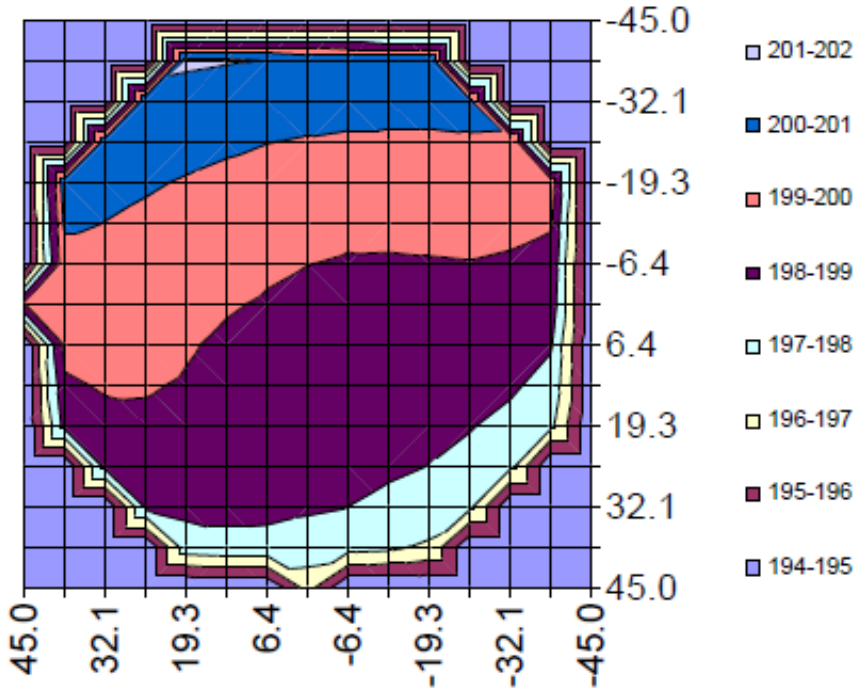


**Figure 43:** The thickness variation map of a $Si_3N_4$ wafer measured using an ellipsometer.

The fabrication procedure is illustrated in Figure 44. The initial step is the preparation and cleaning of the substrate, where AMI (Acetone, Methanol, Isopropanol) cleaning is performed followed by Piranha ($H_2SO_4 : H_2O_2$) cleaning. The cleaning process is very crucial, since any contamination or particles on the substrate can deteriorate the performance of the devices that are later realized on the substrate.

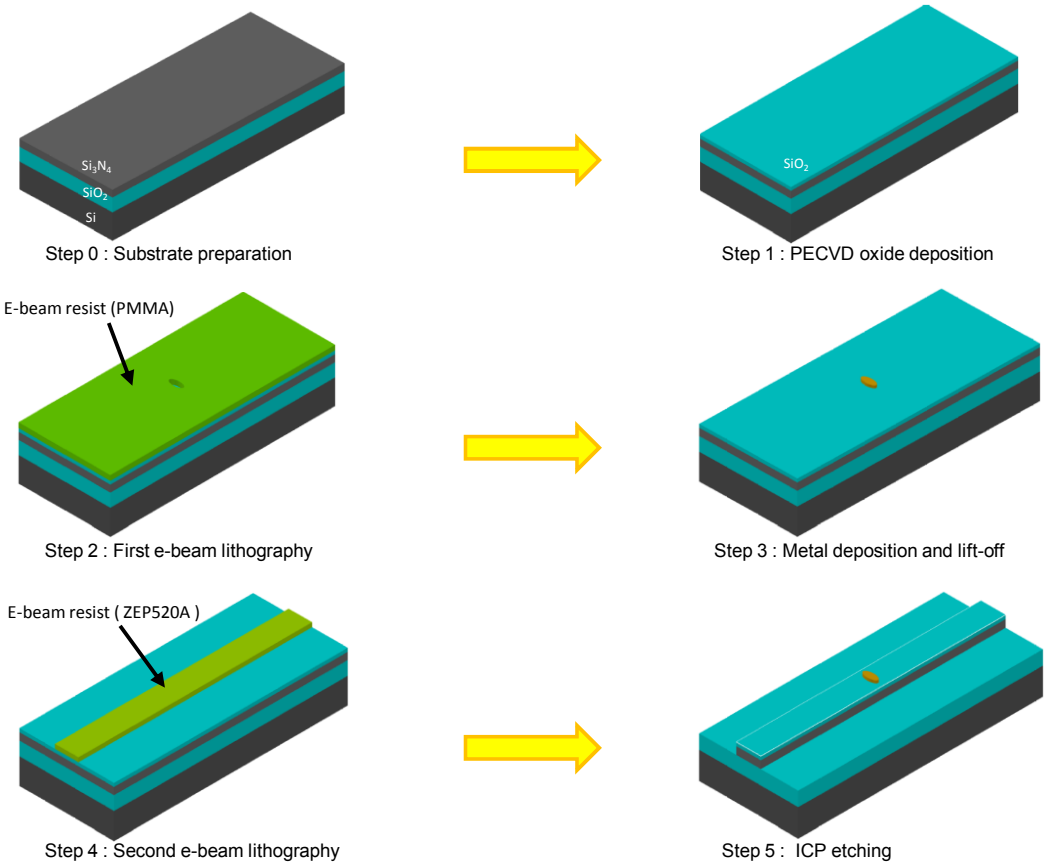


**Figure 44:** Fabrication process flow for hybrid plasmonic-photonic structures using nanofabrication lithography.

Different steps of this fabrication process are described as follows:

1. **Oxide buffer layer deposition**

   In some of the devices we have discussed so far, an oxide buffer layer separates the photonic structure from the plasmonic structure to control the coupling between the two photonic and plasmonic modes. This oxide buffer layer can be deposited using plasma enhanced chemical vapor deposition (PECVD) at the beginning of the process. The thickness of the buffer layer can be precisely controlled with an accuracy of 1 $nm$. This step can be skipped for the devices where a buffer layer is not required. The recipe to deposit PECVD oxide involves two gases of 2%$SiH_4$ and $N_2O$, injected at flow rates of 400 $sccm$ and 1420 $sccm$, respectively. The chamber pressure is kept at 650 $mTorr$, and the process temperature is 300$^\circ C$. The RF frequency is 13.6 MHz, and the power is 25 $W$. The deposition rate using an optimized recipe on an STS-PECVD machine is about 40.3 $nm/min$.

2. **First step of lithography**

   In this step, EBL is used to define the plasmonic patterns. First, a layer of polymethyl methacrylate (PMMA) resist with a 950000 molecular weight is spin-coated on the substrate. Depending on the feature sizes and the required resolution, different dilutions of PMMA in Anisole can be used to obtain the desired thickness. The resist is then pre-baked at 180$^\circ C$ for 90 $sec$. The electron-beam lithography (EBL) is carried out using a JEOL JBX-9300FS EBL System. The exposure is done by using a base dosage of 650 $\mu C/cm^2$ with a beam current of 2 $nA$, and an electron beam energy of 100 $keV$. The minimum shot pitch is 4 $nm$. The dosage is optimized by considering the proximity effects so that the resist is completely exposed in the regions of interest, and at the same time, the feature boundaries are defined precisely. The patterns are then developed in a mixture of methyl isobutyl ketone (MIBK) and isopropyl

alcohol (IPA) for 90$sec$. It should be noted that the optimized dosage and the optimal developing procedure depends on the features. For example, the scanning electron micrographs (SEMs) of two patterns made in PMMA are shown in Figure 45(a) and 45(b). The large pattern in Figure 45(a) is exposed using a total dosage of 650 $\mu C/cm^2$ and the small pattern is exposed using a total dosage of 715 $\mu C/cm^2$. It can be seen that both patterns are well obtained according to the designed layouts. For each particular structure discussed in this dissertation, the EBL optimization is separately carried out.

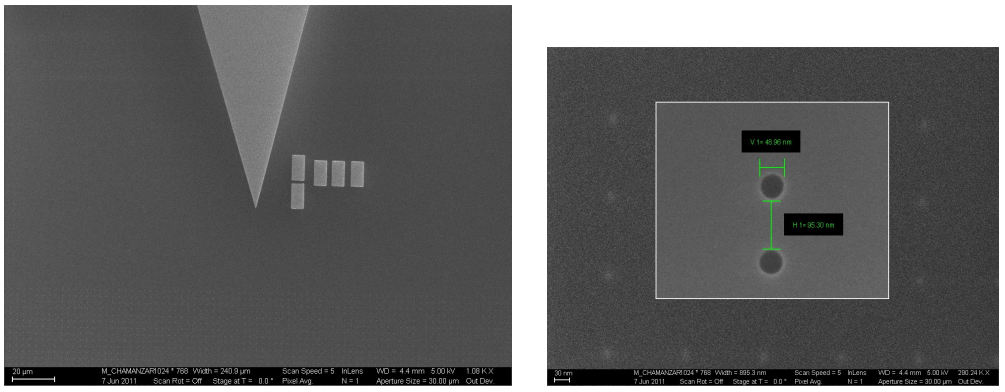

(a) (b)

**Figure 45:** (a) Scanning electron micrograph (SEM) of large markers in PMMA. The pattern was exposed using EBL with a dosage of 650 $\mu C/cm^2$. (b)SEM of small nanopatterns consisting of a dimer of ovals defined in PMMA using a dosage of 715$\mu C/cm^2$.

3. **Metal deposition and lift-off**

   After the plasmonic structure patterns are defined in the e-beam resist using EBL, the plasmonic layer is formed by depositing the appropriate metallic layer. The metal deposition is carried out using electron-beam evaporation. Different metals such as silver and gold can be deposited. Appropriate adhesion layers must be used to ensure the stiction of the metallic layer to the substrate. Titanium (Ti) and chromium (Cr) can be used as an adhesion

layer, since they bind to the gold and the silicon nitride surface very well. The appropriate thickness of the adhesion layer for the plasmonic structures discussed in this thesis has been chosen to be between $1 - 3\ nm$. Most of the metal depositions are carried out using CHA e-beam evaporator. The chamber is pumped down to a pressure level of ( $10^{-7}$Torr) so that the uniformity and homogeneity of the deposited film is ensured. After the metal deposition, lift-off process is carried out by immersing the sample in 1165 microposit remover at an elevated temperature of $70°C$ to remove the resist and the overlaying metals in unwanted regions. This way, the plasmonic structures are realized. This step of fabrication was optimized individually by fabricating isolated plasmonic nanostructures on bare substrates. In Figure 46 the SEM of an array of plasmonic nanoparticles fabricated on a bare silicon substrate is shown, where it can be seen that the features are precisely fabricated.

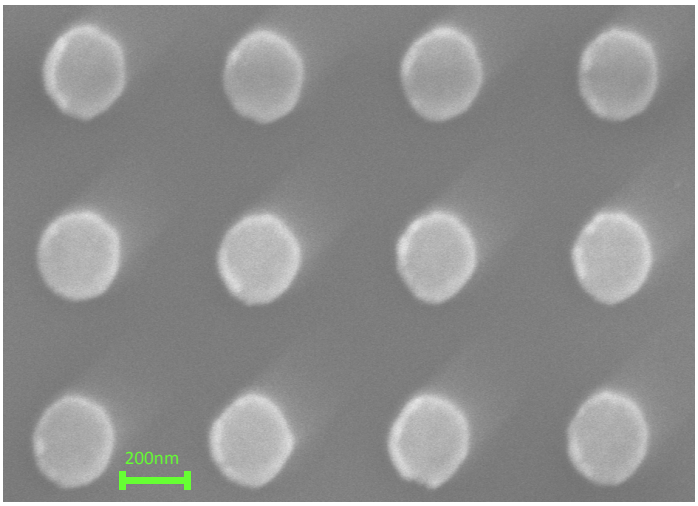


**Figure 46:** Scanning electron micrograph (SEM) of an array of gold nanodisks realized using the lift-off procedure.

4. **Second step of lithography**

   In this step, EBL is used again to define the photonic waveguide patterns.

First, a layer of ZEP520A e-beam resist is spin-coated on the substrate with a thickness of 500 $nm$. The resist is then pre-baked at 180°$C$ for 120 $sec$. The patterns are then written with a base dosage of 250 $\mu C/cm^2$ with a beam current of 2 $nA$ and an electron beam energy of 100 $KeV$. Shot pitch can be in the range of $4-6$ $nm$ depending on the features. The exposed patterns are then developed in Amyl Acetate for 120 $sec$. The registration of the patterns in this step with the patterns defined in the first step of lithography is critical. To ensure the precise alignment between the two steps of EBL, metal markers are fabricated in the first step, and then used in the second EBL step to correct for translation and rotation misalignments. The centers of two distant cross markers on the sample are detected using the EBL in the SEM mode, and the offset in the locations of the cross markers as well as the rotation angle are detected and compensated in the second EBL step.

5. **Etching photonic structures**

   After the photonic waveguides pattern is defined in the resist, this pattern must be transferred to the underlying film. In most of the devices introduced in this work, a $Si_3N_4$ film is used as the photonic layer. To etch $Si_3N_4$ with ZEP520A as the resist, plasma dry etching is used. Two different methods of dry etching have been used, i.e., inductively coupled plasma etching (ICP), and reactive ion etching (RIE). Both of these methods work based on the removal of material from the surface of the sample through active plasma ions. The active plasma ions are accelerated towards the substrate and remove the material either through chemical reactions or physical sputtering. The recipe that has been optimized to etch the $Si_3N_4$ film in this work consists of a mixture of 50 $sccm$ $CHF_3$ and 5 $sccm$ $O_2$. The source power is 175 $W$, and the pressure is 55 $mTorr$. These parameters result in a DC bias of 370 $V$, and the average etch rate of $Si_3N_4$ is 54 $\frac{nm}{min}$, and the average etch rate of ZEP

is 48 $\frac{nm}{min}$. Therefore the selectivity of this process to etch $Si_3N_4$ with ZEP as the mask is 1.125. The etching of $Si_3N_4$ using this recipe on an Oxford RIE machine results in relatively smooth, however angled sidewalls. As an example, the SEM of a waveguide formed by etching $Si_3N_4$ using RIE is shown in Figure 47, where it can be seen that the sidewall is angled and rounded.

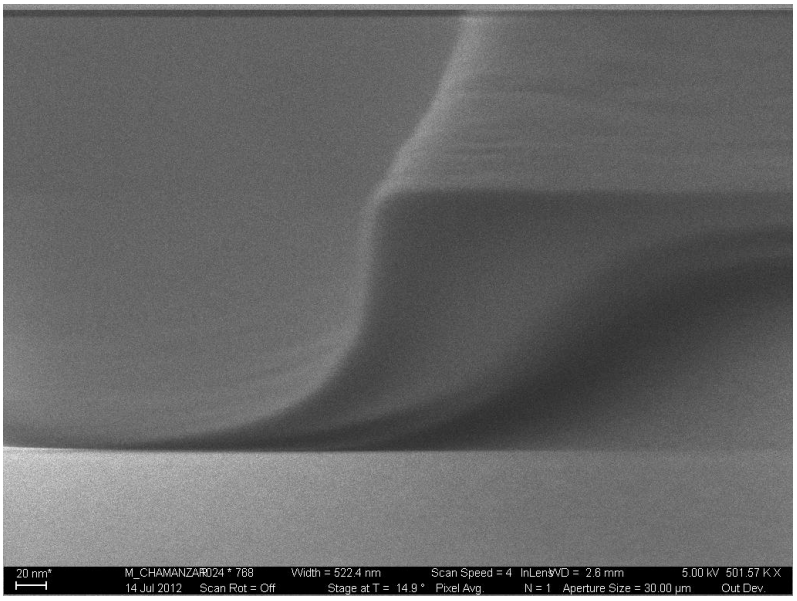


**Figure 47:** Scanning electron micrograph (SEM) of a $Si_3N_4$ waveguide etched using RIE. The sidewalls are angled and rounded.

Another method to etch $Si_3N_4$ is to use ICP with $CF_4$ gas. ICP has a coil connected to an AC power to produce a high density plasma. A recipe has been optimized on an RIE-ICP machine to etch $Si_3N_4$. This machine has the two plates of RIE and a coil to produce ionized gas species. The platen field, then accelerates the ionized species towards the substrate. In this recipe, the platen power is 50 $W$; the coil power is 400 $W$; the gas flow rate is 30 $sccm$. The DC bias turns out to be 216 $V$, and the etch rate was 226 $\frac{nm}{min}$; and the selectivity was 0.61 with respect to ZEP. This selectivity allows etching of about 250 $nm$ $Si_3N_4$ with 500 $nm$ of ZEP mask, leaving a

margin for surface protection. Etching $Si_3N_4$ using ICP results in relatively straight sidewalls. It can be seen from Figure 48 that the waveguide sidewalls are relatively vertical. It can be seen that using an ICP to etch $Si_3N_4$ results in microtrenching. For etching thicker films, a hard mask such as a $SiO_2$ mask can be used.

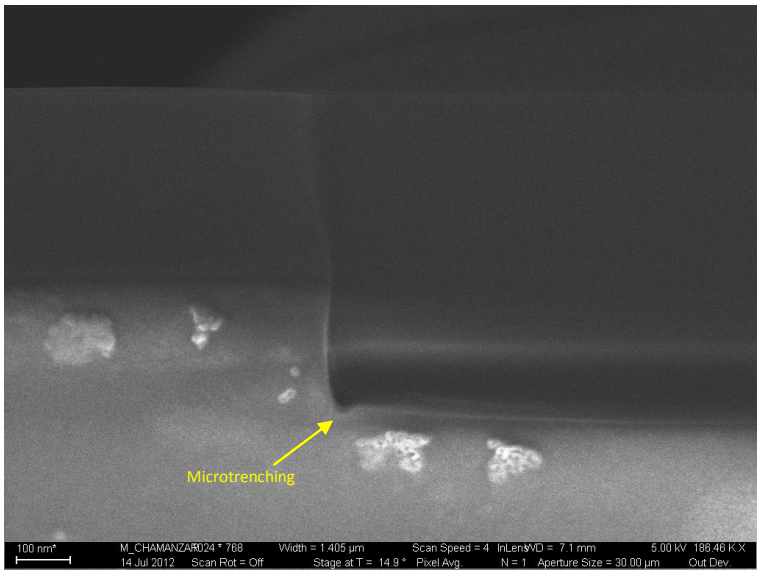


**Figure 48:** Scanning electron micrograph (SEM) of a $Si_3N_4$ waveguide etched using ICP. The sidewalls are relatively vertical. It can be seen that using an ICP to etch $Si_3N_4$ results in microtrenching.

If $Si$ is used as the photonic layer in a silicon on insulator (SOI) platform, then $Cl_2$ can be used as the gas for ICP etching of $Si$. A recipe is optimized on STS SOE machine for this purpose with an etch rate of 160 $\frac{nm}{min}$. If an oxide layer is used as a buffer to separate the photonic and the plasmonic structures, then this layer must be first etched before etching the photonic layer film. Dry etching of this oxide buffer layer can be carried out by ICP etching using a mixture of $CHF_3$ and $CF_4$ gases. A recipe has been optimized on STS SOE to etch $SiO_2$ with an etch rate of 155 $\frac{nm}{min}$ and a selectivity of 0.73 with respect to ZEP.

Different hybrid plasmonic-photonic waveguide devices discussed in the previous

chapter can be fabricated using the nanofabrication process discussed in this chapter. The scanning electron micrograph (SEM) of an exemplary hybrid structure consisting of a gold nanorod and a $Si_3N_4$ ridge waveguide is shown in Figure 49, where it can be seen that the gold nanoparticle is precisely fabricated on the top surface of the $Si_3N_4$ wavegiude. In all of our fabrication trails, consisting of more than 100 such structures, the registration error between the two steps of lithography has always been less than 15 $nm$.

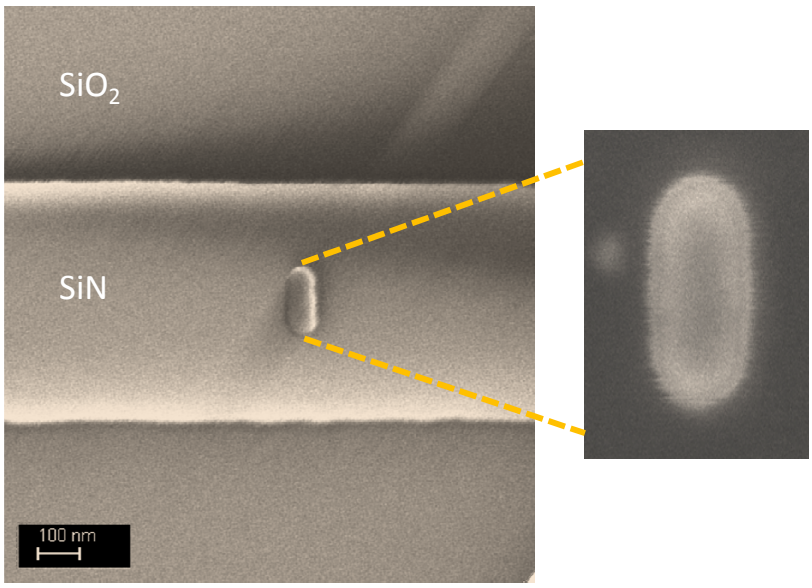


**Figure 49:** Scanning electron micrograph (SEM) of a device consisting of a $Si_3N_4$ ridge waveguide integrated with a nanolithographically fabricated gold nanorod.

As another example, the SEM of a hybrid waveguide structure consisting of a gold nanorod dimer integrated with a $Si_3N_4$ waveguide is shown in Figure 50. The size of each nanorod is 51 $nm \times 73$ $nm$, and the gap between the two nanorods is only 6.8 $nm$. It can be seen that by optimizing the lithography and the lift-off process, even very small gaps and features can be precisely fabricated.

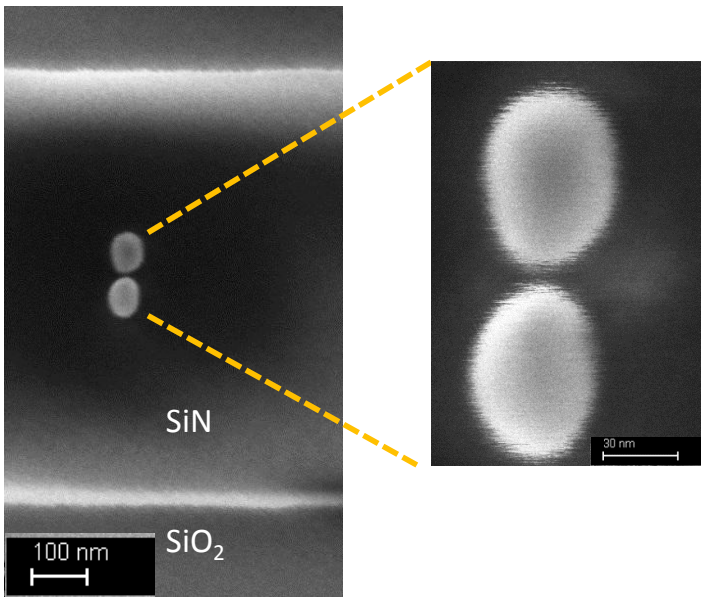


**Figure 50:** Scanning electron micrograph (SEM) of a device consisting of a $Si_3N_4$ waveguide integrated with a dimer of gold nanorods. The size of each nanorod is 51 $nm \times 73$ $nm$, and the gap between the two nanorods is 6.8 $nm$.

## *4.2 Optical characterization of Hybrid Plasmonic-photonic Waveguide Structures*

The experimental characterization of the hybrid plasmonic-photonic devices discussed in previous chapters will be demonstrated in this chapter. To experimentally characterize the realized devices, test setup is designed and built as shown schematically in Figure 51.

In this setup, lightwave from a supercontinuum laser source is first collimated and polarized in free space and then is focused on the side of the chip by using a lens. The chip is placed on a 3D xyz stage with precision micrometers. By precisely positioning the chip facet with respect to the input lightwave spot, we can butt-couple the lightwave into each input waveguide on the chip. The output of the chip is imaged using a lens onto the entrance slit of a spectrometer. A beam splitter is used at the output to direct part of the light to a CCD camera so that the output

waveguide spot can be imaged. A microscope assembly is implemented on top, which provides with the capability of imaging and measuring the scattering from top through a long working distance objective lens.

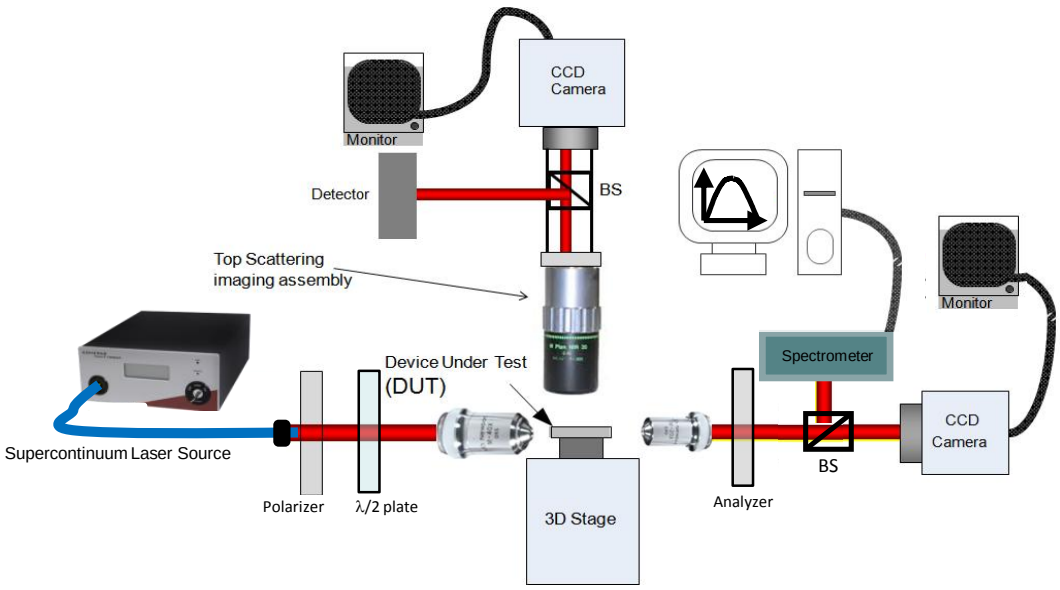


**Figure 51:** Experimental setup schematic for the characterization of hybrid plasmonic-photonic structures consisting of a supercontinuum source and a spectrometer at the output.

An image of the characterization setup is shown in Figure 52, where different components are labeled. The supercontinuum laser source (SuperK Compact) provides a broadband lightwave source covering a wavelength range of $500\ nm - 2000\ nm$. The master laser pulse width is less than $2\ ns$, and the repetition rate is $19\ kHz$. The spectral response of this supercontinuum laser measured using an Agilent 86142B optical spectrum analyzer (OSA) is shown in Figure 53, where it can be seen that the spectral response is nearly flat over the entire range. The range of wavelengths in this measurement was mostly limited to the OSA bandwidth.

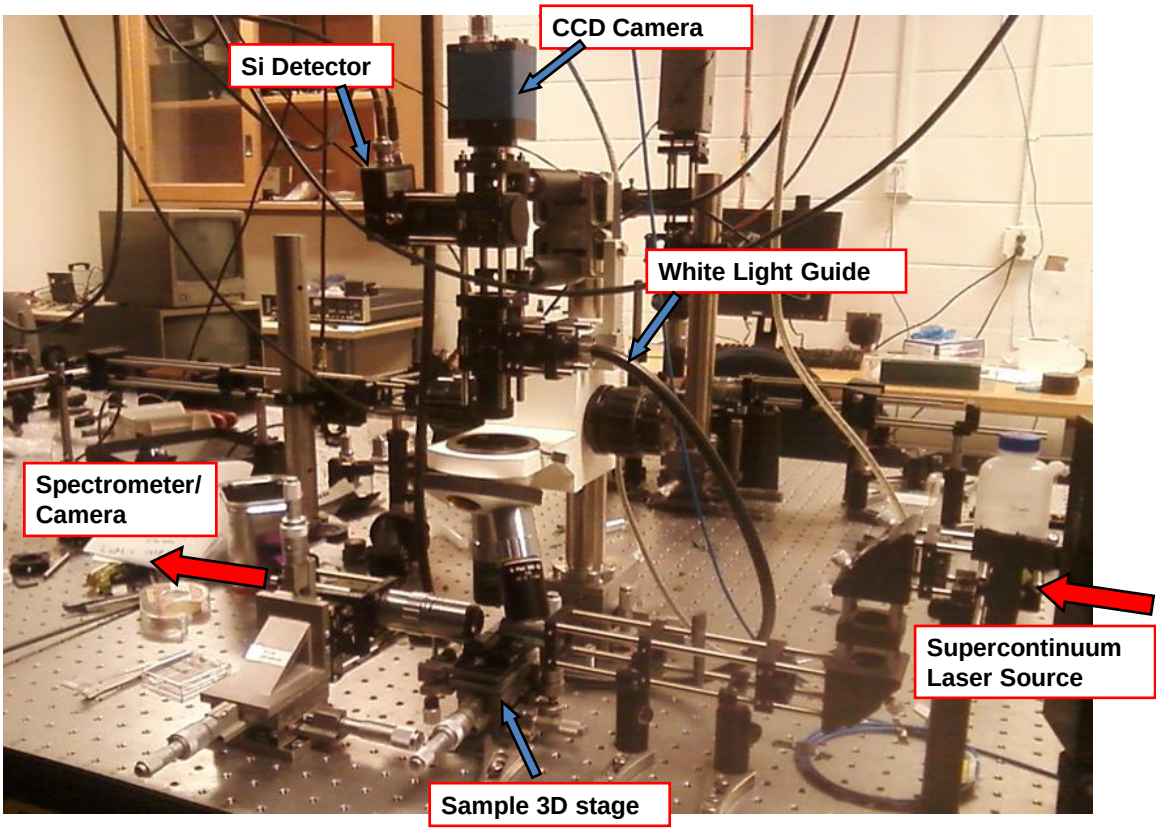


**Figure 52:** Image of the experimental setup for the characterization of hybrid plasmonic-photonic structures consisting of a supercontinuum source and a spectrometer at the output.

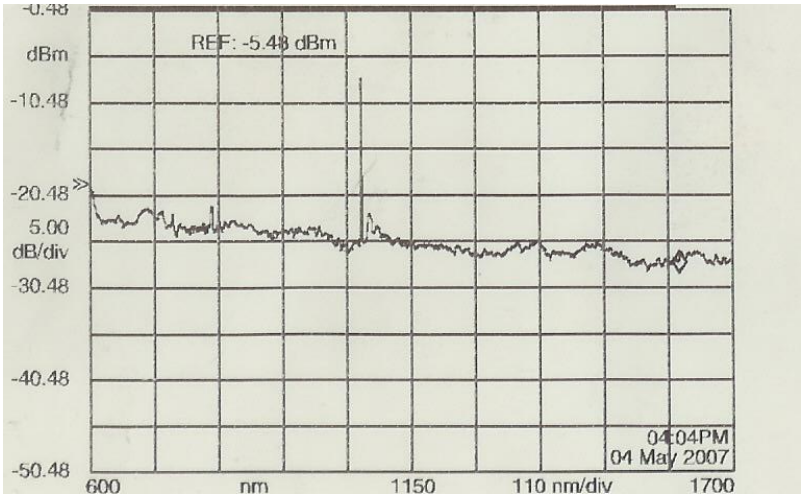


**Figure 53:** The optical spectrum of the supercontinuum broadband laser source measured using an optical spectrum analyzer (OSA).

It should be noted that implementing a working optical setup that can operate with the supercontinuum laser source over such a broad range of wavelengths is quite challenging, and requires special attention, since any dispersion in the system can result in unwanted optical spectral features. To address this issue, special achromatic optical components are used, and the optical paths are carefully aligned so that all the wavelength components of interest are collimated, focused, and imaged together. The top microscope assembly is a bright-field microscope illuminated with a white light source, and consists of a camera and a detector port. This custom-made microscope was assembled so that, the input laser spot and the chip, and the output can be aligned together precisely. Also, part of the light collected through the microscope objective lens is diverted to a detector port through a Pellicle beam splitter, where it can be coupled to a detector or a fiber-coupled spectrometer. Different hybrid plasmonic-photonic structures have been characterized using this characterization setup.

As an example, the darkfield scattering image of an array of identical plasmonic

gold nanorods of dimensions $96 \times 57 \times 27\ nm$ integrated with a $865\ nm \times 200\ nm$ $Si_3N_4$ waveguide measured from top is shown in Figure 54. This array is excited over the bandwidth of the LSPR resonance. It can be seen that the light from the waveguide is coupled to the LSPR mode of the individual plasmonic nanorods, separated from each other by 11 $\mu m$, and the scattering intensity is reduced as the light propagates along the array in the waveguide. In this architecture, different numbers and types of plasmonic nanoparticles can be excited in a controlled manner.

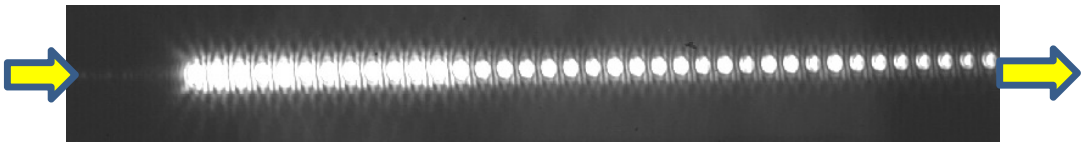

**Figure 54:** Dark-field scattering image of an array of plasmonic nanorods integrated on a $Si_3N_4$ waveguide.

The extinction of plasmonic nanoparticles in the hybrid waveguide structure, as defined in Equation 7, can be obtained by measuring the transmission at the output of the waveguide. In this equation, $''Sample''$ refers to a hybrid waveguide structure containing gold nanorods. In each case, a reference waveguide is measured having the same dimensions as the sample waveguide; however, without the nanoparticle, referred to as $''Ref''$. The dark measurement, $''D''$ is carried out to subtract background from the sample and the reference.

$$Extinction = -10log(\frac{Trans_{Sample}(\lambda) - D}{Trans_{Ref}(\lambda) - D}). \tag{7}$$

The extinction of a hybrid waveguide structure consisting of a $900\ nm \times 200\ nm$ $Si_3N_4$ waveguide integrated with an array of plasmonic gold nanorods of dimensions $96 \times 57 \times 27\ nm$ is measured and is shown in Figure 55. In this figure, the extinction is shown in terms of the optical density (OD). The maximum

extinction occurs at a resonance wavelength of $\lambda_0 = 646.7\ nm$, and is 5.33 $dB$, which corresponds to a coupling efficiency of 6.2 % to each individual plasmonic gold nanorod. The inset of Figure 55 shows the SEM of the hybrid waveguide structure with the $Si_3N_4$ waveguide and an integrated plasmonic gold nanorod. The polarization of the light propagating in the waveguide is chosen to be TE-like so that the main component of the transverse electric field is lined up with the longer dimension of the gold nanorod to excite the longitudinal LSPR mode.

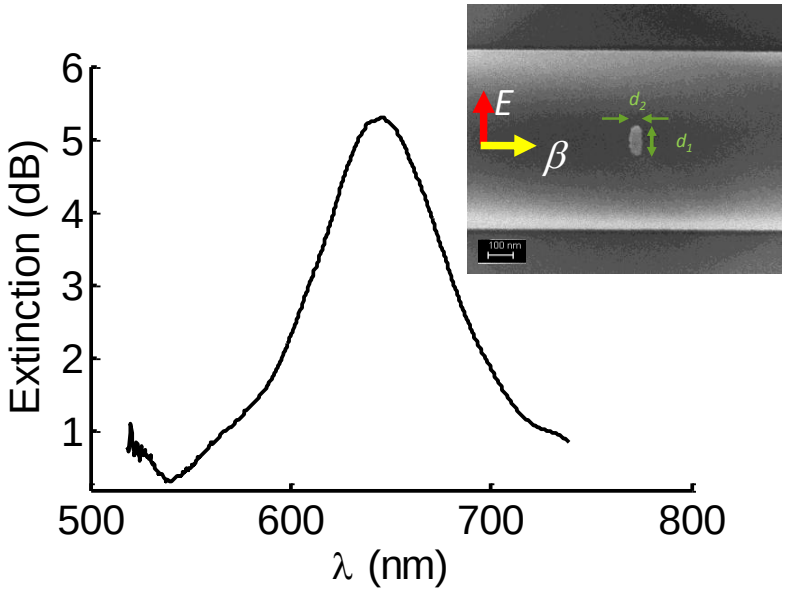


**Figure 55:** Extinction of a hybrid waveguide structure consisting of a 900 $nm \times$ 200 $nm$ $Si_3N_4$ waveguide integrated with an array of plasmonic gold nanorods of dimensions 96 $\times$ 57 $\times$ 27 $nm$.

The normalized extinction of different gold nanorods, all having a thickness of 27 $nm$ and a width of 57 $nm$, with five different lengths, fabricated on different $Si_3N_4$ waveguides with identical dimensions of 865 $nm \times$ 200 $nm$ are measured at the output of the waveguides and plotted in Figure 56. It can be seen that the resonance wavelength of the nanorod LSPR mode redshifts as the aspect ratio of the nanorod is increased. This behavior is expected from theoretical simulation of such structures, as discussed in chapter 3. All the measurements are carried out with an integration time of only 2 $sec$, and the source power was attenuated

using a variable optical density filter so that the power spectral density was only $-54\ dBm/nm$ before coupling to the chip. This suggests that the coupling efficiency is so large that with a room-temperature detector, a very low input power, and only 2 *sec* integration time, the extinction of plasmonic gold nanorods can be easily measured.

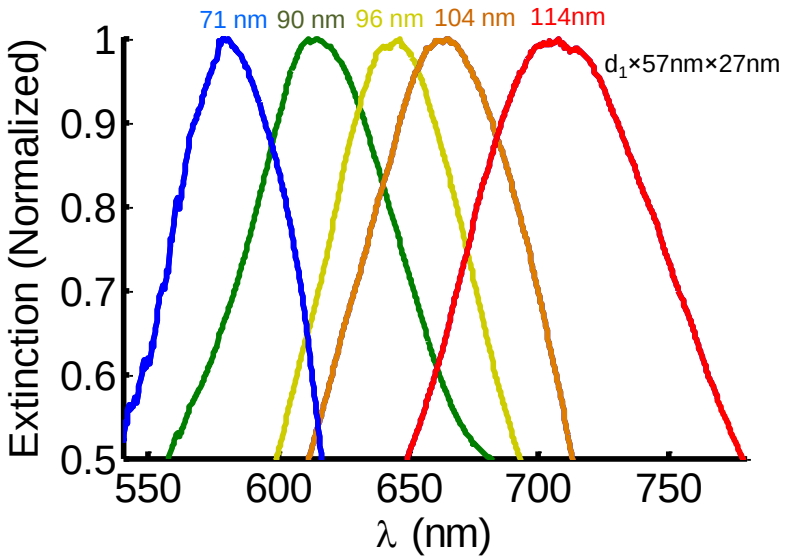


**Figure 56:** Normalized extinction of five different sizes of gold nanorods fabricated on different $Si_3N_4$ waveguides with identical dimensions of 865 $nm \times 200\ nm$, all having a thickness of 27 $nm$ and a width of 57 $nm$, with different lengths($d_1$), indicated on each curve. It can be seen that by increasing the length of the gold nanorod, the resonance is redshifted.

The coupling efficiency, defined as the ratio of input power coupled to an individual plasmonic nanoparticle LSPR mode, and the signal-to-noise-ratio (SNR), defined as the ratio of the signal average power to the noise power, is summarized in Table 2, where it can be seen that the coupling efficiency, and therefore the SNR is very large in each case.

Using numerical simulations, it was shown in chapter 3 that in the hybrid waveguide structure by decreasing the width of the waveguide, the coupling efficiency to the LSPR mode of the plasmonic nanoparticle is increased. The theoretical limit of the coupling efficiency was also obtained to be 50 %, and it was

shown that in some cases the cut-off of the waveguide mode can result in lower limit for the coupling efficiency. Here, the effect of the width of the waveguide on the coupling efficiency is verified experimentally. A number of different hybrid waveguides were fabricated all with the same thickness of 200 $nm$ and different widths. Each waveguides is integrated with plasmonic gold nanorods of dimensions $96 \times 57 \times 27$ $nm$. The coupling efficiency to single gold nanorods is plotted in Figure 57 versus the width of the waveguides. In each case the measurement is repeated many times, and the error bar shows the variations in the measurements. For some of the data points were the error bar is within the markers.

**Table 2:** Coupling efficiency and SNR for different gold nanorods in the hybrid platform

| Gold NanoRods | Coupling Efficiency(%) | Signal-to-noise-ratio (SNR) (dB) |
|---|---|---|
| $71 \times 56 \times 27$ $nm$ | 2.95 | 15.7 |
| $90 \times 56 \times 27$ $nm$ | 3.32 | 19.33 |
| $96 \times 56 \times 27$ $nm$ | 7.18 | 20.2 |
| $104 \times 56 \times 27$ $nm$ | 8.16 | 20.7 |
| $114 \times 56 \times 27$ $nm$ | 9.7 | 24.64 |

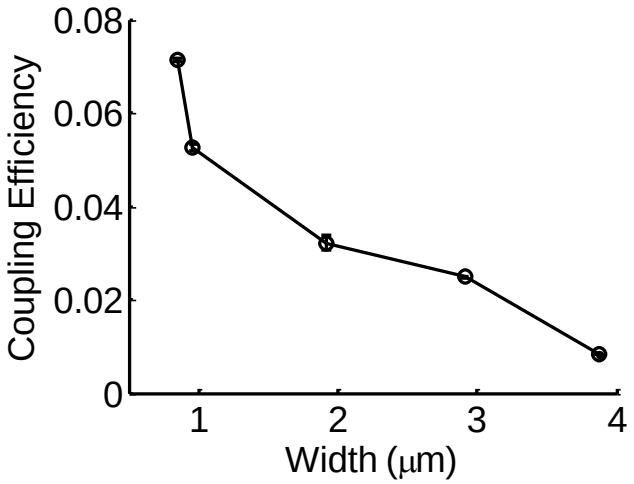


**Figure 57:** Coupling efficiency versus the width of the waveguides for hybrid plasmonic-photonic waveguides having different widths and integrated with plasmonic gold nanorods of dimensions $96 \times 57 \times 27$ $nm$.

It can be seen that by decreasing the width of the waveguides from 3.87 $\mu m$ to less than 900 $nm$, the coupling efficiency for the excitation of a single gold nanorod is increased from less than 1 % to more than 7 %. It should be noted that the width of the waveguide can further be decreased to increase the coupling efficiency. However, by decreasing the width of the waveguide less than 800 $nm$, the input insertion loss is highly increased and more importantly, the waveguide propagation loss is dramatically increased, because the waveguide mode is more spread out of the $Si_3N_4$ core and feels the sidewall roughness arising from fabrication imperfections, more strongly.

It should be noted that the large coupling efficiency of about 8 % to excite individual plasmonic nanoparticle resonance modes is more than two orders of magnitude larger than the coupling efficiency when the nanoparticle is excited in free space using a microscope objective lens. This very large coupling efficiency results in the possibility of single nanoparticle interrogation with low integration time and large SNR, thus eliminating the need for ultra-sensitive detectors such as a cooled CCD. Also, since the coupling efficiency and the SNR are large, the proposed hybrid structure has a good potential for on-chip LSPR sensing.

## *4.3 Experimental Demonstration of On-chip LSPR Sensing using Hybrid Plasmonic-photonic Waveguides*

It was shown in section 4.2 the coupling efficiency and consequently the SNR for the excitation of plasmonic nanoresonators is large in the hybrid waveguide structure. Therefore, the LSPR mode of plasmonic nanoresonators can be efficiently and easily measured. Also, excitation of plasmonic nanoresonators integrated with $Si_3N_4$ waveguides only requires the coupling of light to the fundamental waveguide mode, and does not require bulky and alignment-sensitive microscopes. The extinction of the plasmonic nanoresonators can be measured at

the output of waveguide, making the extinction measurement easy for different hybrid waveguides integrated with different plasmonic nanoparticles. It was also discussed in section 4.1 that plasmonic nanoresonators integrated with $Si_3N_4$ waveguides are very sensitive to the local surrounding environment. Therefore, the proposed hybrid waveguide structure can be used as a robust and sensitive on-chip LSPR sensor. In this section, we will discuss the experimental demonstration of on-chip LSPR sensing using the hybrid plasmonic-photonic waveguide structure. The first set of refractive index sensing demonstrations was carried out using calibrated certified refractive index liquids purchased from Cargille Labs. These are liquids made from Chlorofluorocarbon components that have precisely defined refractive indices. A hybrid plasmonic-photonic waveguide consisting of a 900 $nm \times 200$ $nm$ $Si_3N_4$ waveguide integrated with an array of plasmonic gold nanorods of dimensions $120 \times 57 \times 27$ $nm$ is used. The extinction at the output of this waveguide measured using the method described in section 4.2 is shown in Figure 58. It can be seen that when the nanoparticle is exposed to air, the resonance wavelength is 741.6 $nm$.

Then, different certified calibration refractive index liquids are introduced to the hybrid waveguide structure, and the shift of LSPR mode in the output extinction spectrum is monitored. After introducing each liquid, the sample was carefully washed using organic solvents to make sure that no residue is left from the previous measurement. Then the LSPR spectrum is measured for the sample exposed to air again to make sure that the sensor response is returned to its original baseline. As an example, the LSPR extinction spectrum is shown in Figure 59, for the case when a liquid of refractive index $n = 1.31$ is introduced to the sample. On the same Figure, the extinction spectrum for the case when the hybrid structure is exposed to air is depicted. It can be seen that the introduction of a liquid of refractive index $n = 1.31$ that causes a refractive index change of $n = 0.31$ results

in a resonance shift of $\Delta\lambda_0 = 47.7\ nm$.

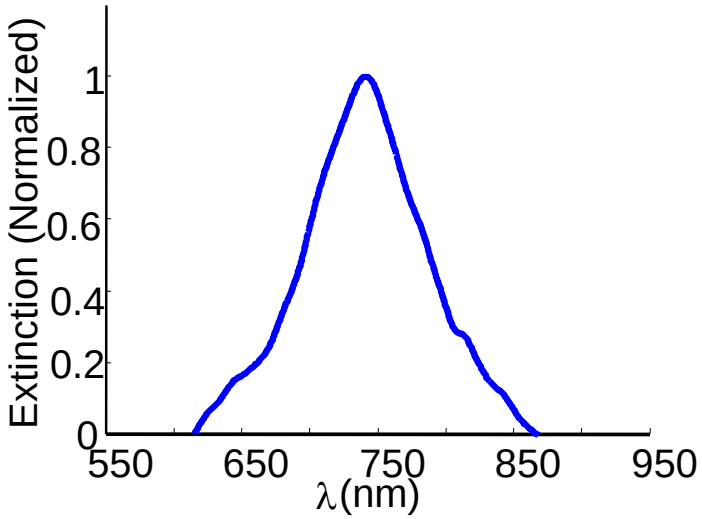


**Figure 58:** The normalized extinction of a hybrid plasmonic-photonic waveguide consisting of a 900 $nm \times 200\ nm$ $Si_3N_4$ waveguide integrated with an array of plasmonic gold nanorods of dimensions $120 \times 57 \times 27\ nm$ when exposed to air.

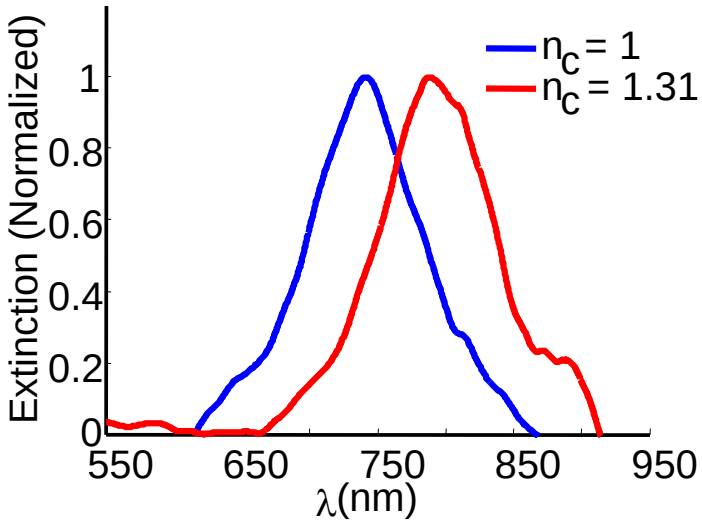


**Figure 59:** The normalized extinction of a hybrid plasmonic-photonic waveguide consisting of a 900 $nm \times 200\ nm$ $Si_3N_4$ waveguide integrated with an array of plasmonic gold nanorods of dimensions $120 \times 57 \times 27\ nm$ when exposed to air, and when a calibrated liquid of index $n = 1.3$ is introduced.

The same experiment was repeated for different certified refractive index

liquids with refractive indexes of $n = 1.31$, $n = 1.35$, and $n = 1.39$. The resonance shift versus the refractive index change is plotted in Figure 60. It can be seen from the linear fit that the sensitivity, defined as the slope of the linear fit, is about 168 $nm/RIU$. In this experiment, the change in the refractive index of the analytes is large, and since the refractive index of each analyte is very precise, the measurements can be used as the calibration of the data.

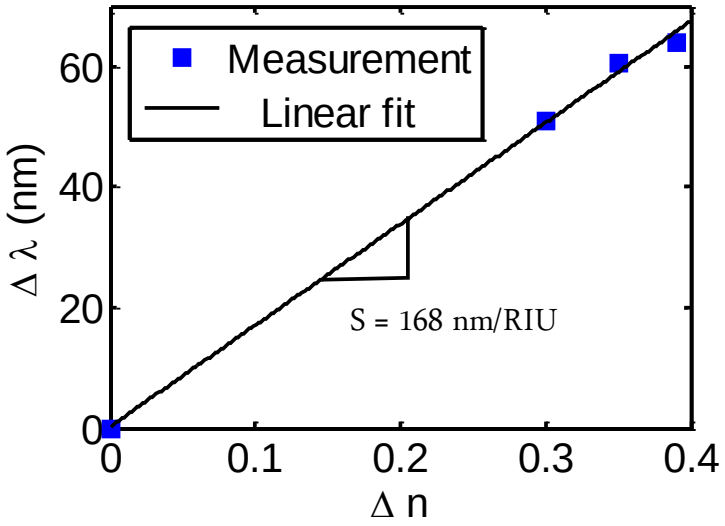


**Figure 60:** The resonance shift versus the refractive index change for a hybrid plasmonic-photonic waveguide consisting of a 900 $nm \times 200$ $nm$ $Si_3N_4$ waveguide integrated with an array of plasmonic gold nanorods of dimensions $120 \times 57 \times 27$ $nm$ when exposed to different analytes. The sensitivity is 168 $nm/RIU$, obtained from the slope of the linear curve fitted to the experimental data.

In practical situations, only a small amount of refractive index change is needed to be detected. As a practical demonstration of the application of the proposed hybrid waveguide structure as an on-chip LSPR sensor, different concentrations of glucose are used as the analyte. Glucose is a carbohydrate that serves as the primary source of cell energy, and the detection of glucose in different bodily serums is very important [93]. In a recent work, [94]Feng textitet al. have shown the application of plasmonic interferometers for the detection

of glucose. Here, we use Dextrose (D-glucose), which is the most abundant isomer of glucose, to demonstrate the sensing performance of the proposed hybrid structure. Dextrose ($C_6H_{12}O_6$) solutions are prepared at different concentrations. To characterize and calibrate the dextrose solutions, the refractive index associated with each concentration is first measured at $20^{\circ}C$ using a commercial Spectronic refractometer. The measurement results are shown in Figure 61. A linear regression fit reveals the relation between refractive index and concentration as $n = 0.16[C] + 1.334$, where $[C]$ is the concentration, and $n$ is the refractive index.

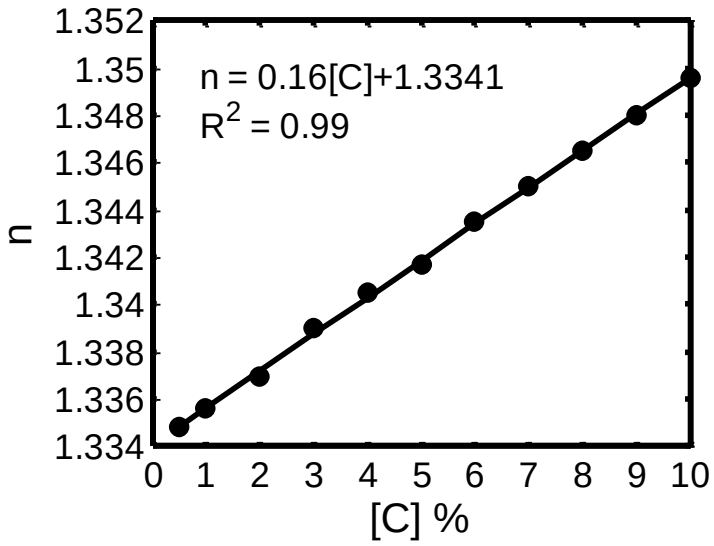


**Figure 61:** Refractive index of dextrose at different concentrations and the linear regression fit. The relation between the refractive index and the concentration is obtained as $n = 0.16[C] + 1.334$

A hybrid device consisting of $96 \times 57 \times 27$ $nm$ gold nanorods integrated with a 865 $nm \times 200$ $nm$ $Si_3N_4$ waveguide is used to carry out the LSPR sensing on these different sugar solutions. A PDMS fluidic system consisting of a microfluidic channel and a reservoir is integrated with the sample so that these different analytes can be introduced to the hybrid waveguide structure. The microfluidic fabrication and integration techniques are explained in detail in chapter 6. The reservoirs are connected to appropriate tubes and the analyte is pumped through

the channel using a syringe pump. The image of a hybrid device integrated with PDMS microfluidic channels and appropriate tubes placed in the optical characterization setup is shown in Figure 62. The microfluidic channel is at a normal angle to the direction of waveguides. It can be seen from Figure 62 that the analyte flow direction over the hybrid device is perpendicular to the direction of light coupling to the sample. Using such an integrated microfluidic system allows the introduction of multiple analytes one after the other and washing of the sample can be carried out in situ while the optical measurement is ongoing.

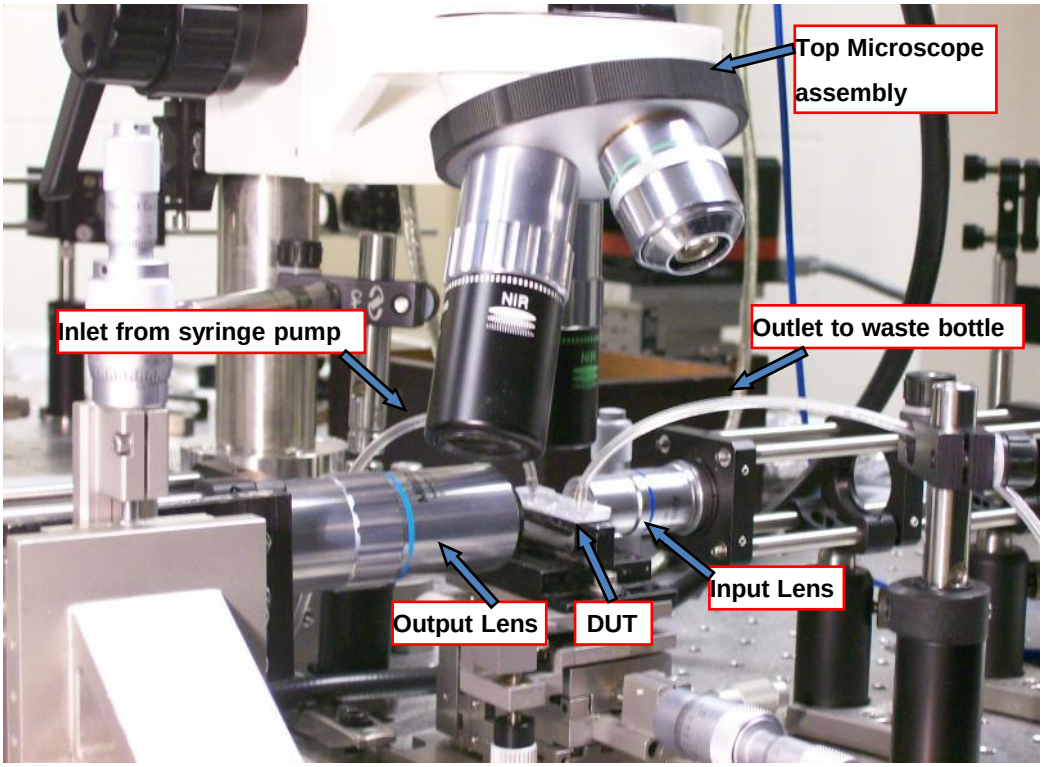


**Figure 62:** A hybrid waveguide structure integrated with PDMS microfluidic channels and reservoirs connected with tubes. The analyte of interest is pumped through the channel in a direction that is perpendicular to the direction of waveguides. The tubings are connected to a syringe pump to introduce the analyte.

The different dextrose solutions are then pumped through the microfluidic channel on the hybrid devices with a rate of 100 $\mu$L/$min$, and the shift of the LSPR resonance peak is monitored with respect to the location of the LSPR resonance for deionized (DI) water. After each sensing step, the channel is entirely washed with DI water for 1 hour to make sure that no residue of dextrose is left on the sample. In each measurement, the LSPR resonance shift due to pure DI water is used as the reference (baseline). As an example, in Figure 63, the LSPR spectrum of a device consisting of 96 $\times$ 57 $\times$ 27 $nm$ gold nanorods integrated with a 865 $nm$ $\times$ 200 $nm$ $Si_3N_4$ waveguide is shown for a dextrose solution of 8 % concentration. The LSPR extinction resonance spectrum of the device for DI water as the analyte is also shown in Figure 63, before and after the measurement of the dextrose solution.

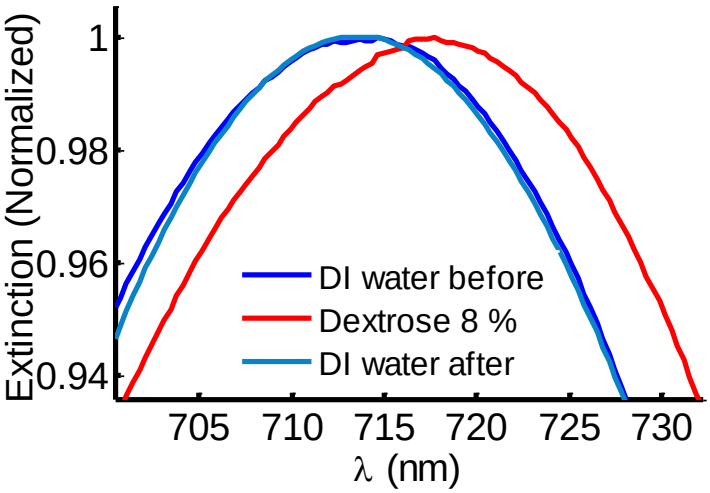


**Figure 63:** The LSPR spectrum of a hybrid waveguide device consisting of 96 $\times$ 57 $\times$ 27 $nm$ gold nanorods integrated with a 865 $nm$ $\times$ 200 $nm$ $Si_3N_4$ waveguide is shown for a dextrose solution of 8 % concentration. The LSPR extinction spectrum of the device when DI water is flowing through the microfluidic channel is shown before and after the introduction of the dextrose solution, where an almost perfect reversibility and stability is observed.

It can be seen that the introduction of dextrose 8 % causes 3 $nm$ resonance shift. The extinction spectrum due to DI water measured after the introduction of the dextrose solution matches well with that due to the DI water before the

introduction of dextrose solution, and returns to the baseline. This shows that the sensor response is perfectly reversible. The second DI water measurement was carried out 1 hour after the first measurement, and the agreement between the two results shows the stability and reversibility of the on-chip LSPR sensor performance.

The same experiment is carried out for different concentrations of dextrose, and the results are shown in Figure 64, where the LSPR wavelength shift is plotted versus the concentration, and the refractive index of each solution obtained from the results of Figure 61. In each case, the measurement was repeated 10 times at different time intervals. The linear regression fit to the measurement data shows a sensitivity of about 250 $nm/RIU$. The error bars show the deviation of the measurements. In these measurements, the coupling efficiency to the LSPR mode of the individual gold nanorod is 8.1 % and the measured SNR is 24 $dB$. The detection limit in these measurements is limited to the resolution of the spectrometer being 0.3 $nm$.

It should be noted that in our measurements, we have used the raw measured data to obtain the LSPR wavelength. Therefore, the presented results show the performance of the device and the measurement system including the spectrometer. However, if a priori knowledge about the resonance lineshape is used from simulations, and post processing of the data is carried out to cancel the noise effects, even much better performance can be obtained. Here, the main focus has been to demonstrate the device performance as an On-chip LSPR sensor.

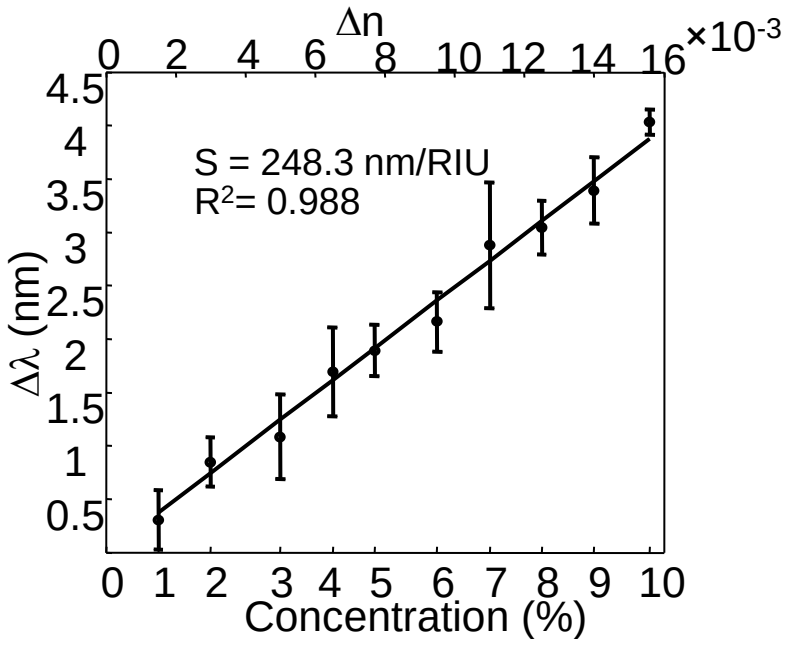


**Figure 64:** The LSPR wavelength shift versus the concentration for dextrose solutions at different concentrations. The hybrid waveguide device consists of a 865 $nm \times 200\ nm$ $Si_3N_4$ waveguide and $96 \times 57 \times 27\ nm$ gold nanorods. The linear regression fit to the measurement results suggests a large sensitivity of about 250 $nm/RIU$.

It should be noted that the efficiency of coupling of the light propagating in the waveguide to the LSPR modes of plasmonic nanoparticles in the hybrid structures introduced in this chapter being about 8 % to individual plasmonic nanoparticles is very large and results in a large SNR suitable for LSPR sensing. The coupling of light from free-space to the $Si_3N_4$ waveguide was carried out using a focusing lens. This coupling mechanism can be further improved by using an inverse taper waveguide input. It has been shown that by using an inverse taper waveguide the insertion loss of the light coupling to the fundamental mode of a ridge waveguide can be reduced to 0.8 $dB$ [95]. This way even with lower input powers and less integration times, the same SNR can be obtained, making the proposed device platform operate even faster and with a lower power consumption. This device can be integrated with superluminescent light emitting diodes (SLEDs)

and on-chip spectrometers [58, 59] to realize a fully functional stand-alone on-chip sensor. The proposed device can be used for the interrogation of different types of individual plasmonic nanoparticles with high efficiency. Different types of plasmonic nanoparticles can be integrated in parallel on different waveguides or in series on a single waveguide, each one designed for a specific LSPR wavelength, and functionalized to bind to a specific target molecule. This way a fully functional multi-analyte multiplex real-time sensing platform can be realized. The very small form factor, robust and alignment-insensitive architecture, large SNR, real-time response of the proposed device, and its potential of integration with SLEDs and on-chip spectrometers makes it practical for lab-on-chip applications commensurate with the requirements of point of care diagnostics.

# CHAPTER V

# HYBRID PLASMONIC-PHOTONIC RESONATOR STRUCTURES

In this chapter, hybrid plasmonic-photonic resonator-based structures are discussed. These structures consist of photonic resonators integrated with plasmonic structures. The devices introduced in this chapter can be considered as extensions of the waveguide-based structures discussed in chapter 3. Compared to the waveguide-based structures, where photonic waveguides have the role of routing and coupling of the lightwave, here, high quality photonic resonators with their large field enhancements and narrow resonance features are employed to add more functionalities to the hybrid plasmonic-photonic platform. First, the structures consisting of microresonators and plasmonic nanoresonators, which are strongly coupled with each other, will be discussed. Second, hybrid structures consisting of photonic microresonators vertically coupled to plasmonic ring resonators supporting surface plasmon polaritons will be introduced. The design procedure and the developed analytical models will be presented. Finally, the application of these hybrid resonator-based structures for sensing will be investigated.

## *5.1 Plasmonic Nanoresonators Integrated with Photonic Microresonators*

In this section, a hybrid plasmonic-photonic double-resonator structure is introduced that consists of a photonic microresonator and a plasmonic nanoresonator tightly integrated with each other [96]. Photonic microresonators can have high quality factors, and therefore, narrow resonance features. However, their physical

size and mode volume are large. On the other hand, plasmonic nanoresonators having extremely small sizes can enhance the lightwave intensity by several orders of magnitude. However, the resonance features of these plasmonic nanoresonators are broadband. The very small size of the plasmonic nanoresonators makes coupling of lightwave energy from outside to the resonance modes of these nanoresonators difficult and inefficient. The hybrid structure introduced here is designed to benefit from the best of the two worlds of photonic resonators and plasmonic nanoresonators. In this double-resonator structure, lightwave can be enhanced in two steps. It is first trapped and enhanced in the photonic resonator. Then, it is enhanced in another step in the plasmonic nanoresonator. It should be noted that these two types of resonators do not function independently, and mutual loading effects must be considered. In fact, the structure must be designed and analyzed as a holistic system rather than two independent structures coupled to each other. The plasmonic nanoresonators can be made from gold, silver, or any other plasmonic material, and they can be of different shapes, such as nanodisks, nanorods, nanocages, nanoframes, and bowtie antennas [45]. The photonic resonator can be a traveling-wave microresonator such as a microring or a microdisk resonator, or a standing wave resonator such as a photonic crystal resonator, a nanobeam photonic crystal resonator, or a Fabry-Perot resonator [53]. It will be shown that by properly designing the hybrid resonator structure, ultra-high field enhancements can be achieved that can be used for enhanced light-matter interaction. Using the hybrid resonator structure, individual plasmonic nanoresonators can be excited in a controlled and efficient way. In addition to practical applications, the hybrid structure provides a platform to study the individual plasmonic nanoresonator resonance properties without the interference of the collective effects of an ensemble of nanoresonators.

The schematic of the proposed hybrid plasmonic-photonic double-resonator

structure is shown in Figure 65. It consists of a silicon nitride ($Si_3N_4$) microring resonator integrated with a gold nanorod. The substrate is silicon dioxide ($SiO_2$). A photonic bus waveguide is used to deliver the lightwave to the hybrid resonator structure. When the lightwave is coupled from the bus waveguide to the hybrid resonator structure, it circulates around the dielectric microring resonator and gets enhanced and gradually couples to the LSPR mode of the plasmonic nanoresonator. The photonic microresonator has a cross section of ($w \times h$) and an outer radius of $R$. The plasmonic nanorod has dimensions of ($d_1 \times d_2 \times t$), and is assumed to be made from gold. The radius of curvature of the nanorod is assumed to be half of its width, i.e., ($\frac{d_2}{2}$). The polarization of light in the photonic structure is desired to be TE-like with the major component of the transverse electric field parallel to the longer dimension of the nanorod.

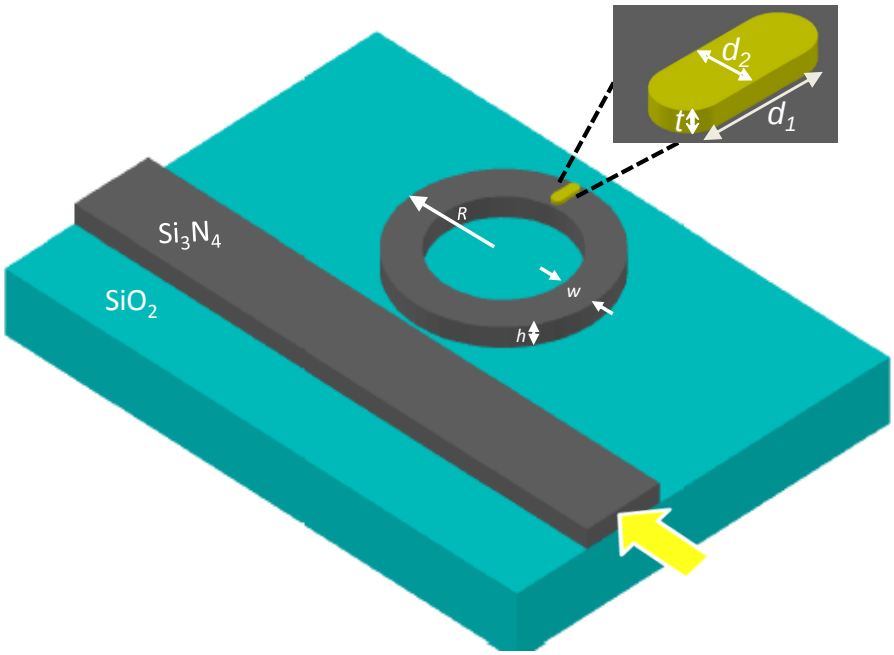


**Figure 65:** Schematic of the proposed hybrid plasmonic-photonic double-resonator structure consisting of a microresonator integrated with a plasmonic nanoresonator.

Since the coupling between the two resonator structures is very strong, conventional coupled mode theory cannot be used to calculate the modes of the hybrid resonator structure and a more rigorous method must be adopted. Here, a combination of FDTD analysis [69] and scattering matrix method [97] is used to analyze and design this hybrid resonator structure. Figure 66 shows a schematic of the hybrid resonator structure with forward and backward propagating waves indicated at different points. In the model discussed here, forward and backward electromagnetic waves at different points are related to each other trough scattering matrices. Existence of the plasmonic nanoresonator can result in the coupling of clockwise and counterclockwise modes in the photonic microresonator. Therefore, both modes are considered in the analysis.

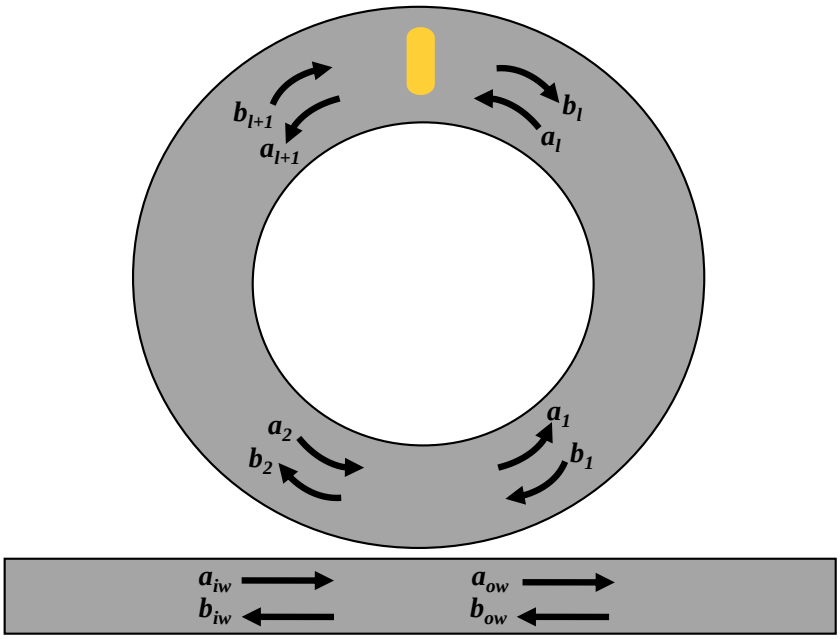


**Figure 66:** Two-dimensional schematic of a hybrid plasmonic-photonic double-resonator structure consisting of a microring resonator integrated with a plasmonic nanoresonator. Forward and backward propagating field amplitudes are indicated at different points on the structure.

Before discussing the model developed here for the analysis of the hybrid structure in a rigorous manner, a heuristic description is provided to better

understand how the model works. The incident lightwave in the waveguide, $a_{iw}$, is coupled to the counterclockwise traveling-wave mode of the photonic microresonator, $a_1$, which propagates around the microresonator, $a_l$. Part of the incident lightwave is coupled to the plasmonic nanoresonator mode and the rest is either reflected, $b_l$, or transmitted, $b_{l+1}$. These lightwaves propagate in opposite directions around the microring resonator. Part of the counterclockwise mode is then coupled to the bus waveguide in the forward direction. Similarly, part of the clockwise mode is coupled to the bus waveguide in the backward direction, which forms the reflection. It should be noted that in steady state, all these lightwaves exist simultaneously, and the heuristic and step-by-step explanation of the lightwave progression in the structure is not accurate. If there is no incident lightwave in the bus waveguide in the counter-propagating direction, then $b_{ow} = 0$. However, to keep the generality of the analysis, all the forward and the backward propagating waves available in the analysis are retained, and they will be made equal to zero whenever necessary in the numerical implementation. This is particularly useful when the bus waveguide itself is part of another microresonator. The light waves in the bus waveguide can be related to the lightwaves in the microring resonator as

$$\begin{bmatrix} a_{ow} \\ a_1 \end{bmatrix} = \begin{bmatrix} t & \kappa \\ -\kappa^* & t^* \end{bmatrix} \begin{bmatrix} a_{iw} \\ a_2 \end{bmatrix}, \tag{8}$$

and due to the reciprocity of the passive structure,

$$\begin{bmatrix} b_{iw} \\ b_2 \end{bmatrix} = \begin{bmatrix} t & \kappa \\ -\kappa^* & t^* \end{bmatrix} \begin{bmatrix} b_{ow} \\ b_1 \end{bmatrix}. \tag{9}$$

The lightwaves near the plasmonic nanoresonator in the microresonator, $a_l$ and $b_l$,

are related to the lightwaves $a_1$ and $b_1$, through the propagation matrix, $[P_1]$ as

$$\begin{bmatrix} a_l \\ b_l \end{bmatrix} = \begin{bmatrix} P_1 \end{bmatrix} \begin{bmatrix} a_1 \\ b_1 \end{bmatrix}, \tag{10}$$

where

$$[P_1] = \begin{bmatrix} \exp(-j\beta L_1 - \alpha L_1) & 0 \\ 0 & \exp(+j\beta L_1 - \alpha L_1) \end{bmatrix}, \tag{11}$$

is the propagation matrix, which accounts for the phase retardation as well as the loss of the electromagnetic waves propagating around the microresonator. The propagation constant in the microresonator is indicated by $\beta$, and the loss decay constant is indicated by $\alpha$. The average length of the microresonator from the waveguide-microresonator coupling point to the plasmonic nanoresonator location is indicated by $L_1$.

Similarly, the lightwaves, $a_{l+1}$ and $b_{l+1}$ are related to the lightwaves $a_2$ and $b_2$, through the propagation matrix, $[P_2]$ as

$$\begin{bmatrix} a_2 \\ b_2 \end{bmatrix} = \begin{bmatrix} P_2 \end{bmatrix} \begin{bmatrix} a_{l+1} \\ b_{l+1} \end{bmatrix}, \tag{12}$$

where $[P_2]$ is the propagation matrix accounting for the phase shift and loss of the lightwaves propagating from the nanoresonator to the waveguide-microresonator coupling point. The lightwaves in the microresonator and next to the plasmonic nanoresonator are related to each other as

$$\begin{bmatrix} a_{l+1} \\ b_{l+1} \end{bmatrix} = \begin{bmatrix} M \end{bmatrix} \begin{bmatrix} a_l \\ b_l \end{bmatrix}, \tag{13}$$

where $[M]$ is a matrix that accounts for the coupling of the clockwise and counterclockwise propagating lightwaves to the LSPR mode of the plasmonic nanoresonator as well as the reflection from and the transmission through the

nanoresonator. The portion of the hybrid double-resonator that consists of the plasmonic nanorod coupled to the microresonator can be locally assumed to be a hybrid waveguide similar to the structure introduced in section 3.1. Therefore, the results of section 3.1 can be used to obtain the matrix $[M]$. In section 3.1, the incident lightwave was assumed to be incident only from one side to the hybrid waveguide-based structure. Here, the results are extended for the case where the waveguide is excited using counter-propagating waves. According to Figure 67, the matrix $[M]$ can be constructed as

$$\left[M\right] = \begin{bmatrix} \frac{t_p^2 - r_p^2}{t} & \frac{r_p}{t_p} \\ \frac{-r_p}{t_p} & \frac{1}{t_p} \end{bmatrix}, \tag{14}$$

where $r_p$ and $t_p$ are the reflection and the transmission coefficients for the hybrid waveguide-based structure when excited from each side.

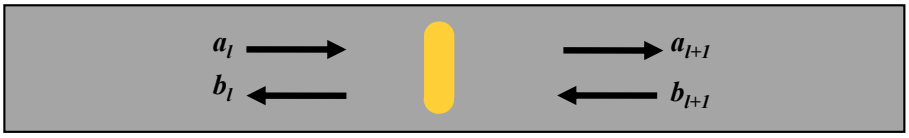


**Figure 67:** The portion of the hybrid structure in Figure 66 consisting of the plasmonic nanoresonator is modeled as a hybrid waveguide-based structure excited from both ends.

Since the coupling between the plasmonic nanoresonator and the photonic microresonator is strong, FDTD analysis is used here to obtain $r_p$ and $t_p$. In other words, the matrix $[M]$ is obtained using FDTD analysis in a rigorous way, and then it is inserted in the aforementioned scattering matrix analysis. Mathematical manipulation of Equations 8 to 14 results in expressions for various lightwave fields throughout the hybrid resonator structure. For example, the field amplitude

in the photonic microresonator, $a_1$, can be obtained as

$$\frac{a_1}{a_{iw}} = \kappa^* \frac{\exp(j\beta L)\exp(-\alpha L) - t_0 t^*}{t_0 t^*(1 - exp(-2\alpha L) - t^{*2}({t_p}^2 - {r_p}^2)[exp(-j\beta L) - exp(j\beta L)]exp(-\alpha L))}. \tag{15}$$

Other field components at different points can be easily found in a similar way using the scattering matrix relations in Equations 8 to 14.

The coupling efficiency, similar to the one defined in section 3.1, is defined as the fraction of the input power in the bus waveguide that is coupled to the plasmonic nanoresonator. Therefore, the coupling efficiency can be obtained as

$$|k|^2 = \frac{(|a_l|^2 + |a_{l+1}|^2) - (|b_l|^2 + |b_{l+1}|^2)}{|a_{iw}|^2}. \tag{16}$$

In the hybrid double-resonator structure introduced in Figure 65, the input lightwave is coupled to the plasmonic nanoresonator mode in two steps. In the first step, lightwave is coupled to the photonic microresonator from the bus waveguide. In the second step, the lightwave trapped in the microresonator is coupled to the LSPR mode of the nanoresonator. In analogy to microwave antenna theory, the photonic microresonator can be thought of as a matching circuitry behind the nanoresonator antenna facilitating the coupling of the input lightwave to the LSPR mode of the nanoresonator. In order to design and analyze the hybrid structure, it is first assumed that the gap between the waveguide and the hybrid resonator is so large that the coupling between the two structures is weak and the loading effect of the bus waveguide on the hybrid resonator structure can be neglected. The reflection and the transmission of the bus waveguide, for a hybrid resonator structure consisting of a 20 $\mu m$ radius microring with dimensions of ($w = 700\ nm$ and $h = 200\ nm$) integrated with a gold nanorod of dimensions ($100\ nm \times 56\ nm \times 30\ nm$), are plotted for the two cases of photonic microresonator with and without the gold nanorod, in Figure 68(a) and 68(b), respectively.

The results are plotted for an intrinsic quality factor of $Q_0 = 1.5 \times 10^4$ and

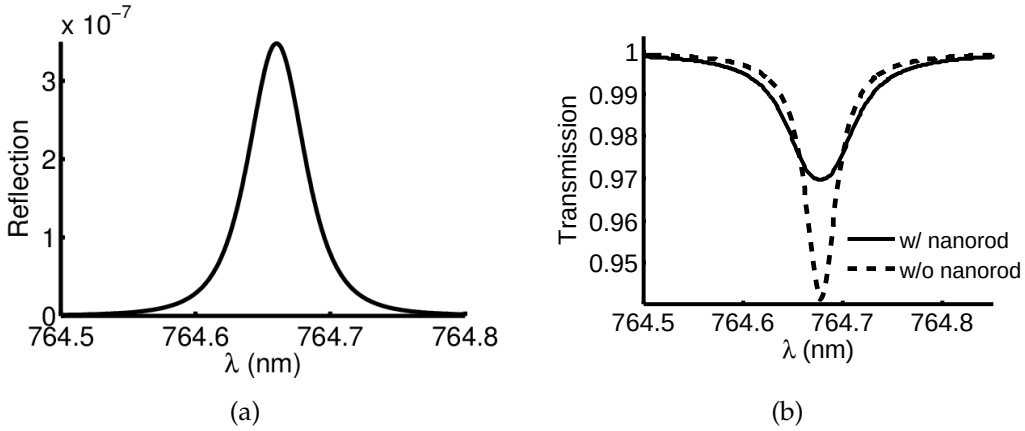


(a) (b)

**Figure 68:** (a) Reflection and (b) transmission of a bus waveguide coupled to a hybrid double-resonator in weak coupling regime with $Q_c = 10^7$. The results are plotted for two cases, one with a nanorod and the other without a nanorod. No reflection occurs when there is no nanorod integrated with the microresonator.

a coupling Q of $Q_c = 10^7$. The gold nanorod causes some portion of the counterclockwise mode to be coupled to the clockwise mode in the microresonator, which is consequently coupled to the reflected lightwave. From the transmission spectrum, Figure 68(b), it can be seen that the effect of the plasmonic nanorod is to broaden the resonance and lower the extinction.

As a reference, plasmonic resonance spectrum showing the lineshape of the gold nanorod (100 $nm \times 56$ $nm \times 30$ $nm$) integrated with a waveguide of the same dimensions as those of the microring resonator, i.e., (700 $nm \times 200$ $nm$), is calculated using a rigorous 3D FDTD analysis and the result is plotted in Figure 69. It can be seen that the LSPR wavelength is $\lambda = 763.9$ $nm$ and the lineshape is broadband with a full width at half maximum (FWHM) of 91 $nm$.

It should be noted that in Equation 15, $r_p$ and $t_p$ are functions of frequency and have resonance behaviors similar to the one shown in Figure 69. Therefore, the lightwave amplitudes and consequently, the coupling efficiency defined in Equation 16 are intricate functions of frequency. To gain more insight into the modes of the hybrid resonator structure, we study the response of the hybrid

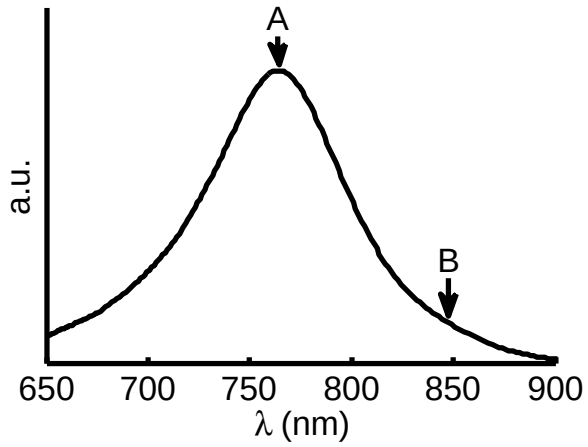


**Figure 69:** Plasmonic resonance lineshape of the gold nanorod (100 $nm \times$ 56 $nm \times 30$ $nm$) integrated with a waveguide that has the same dimensions (700 $nm \times 200$ $nm$) as those of the microring resonator cross section. Point A indicates the resonance wavelength, and point B indicates a wavelength far from the resonance wavelength.

double-resonator structure both at an input wavelength close to the LSPR peak wavelength, point $A$ in Figure 69, and also at a wavelength far from the LSPR peak wavelength, point $B$ in Figure 69. Figure 70(a) shows the coupling efficiency at the LSPR peak wavelength, point $A$, and Figure 70(b) shows the coupling efficiency far from the LSPR peak wavelength at $\lambda = 845.7$ $nm$, point $B$. It can be seen that far from the resonance of the plasmonic nanoresonator, the coupling efficiency exhibits a doublet response resulting from splitting of the counter-propagating modes. As the incident wavelength deviates from the plasmonic nanoresonator LSPR peak wavelength, the splitting becomes stronger and the coupling efficiency decreases. Therefore, the splitting quality factor, $Q_s = \frac{\omega n_g 2\pi R}{|r_p|^2 c}$, can be used as a measure of the coupling efficiency. Here, $\omega$ is the angular frequency, $n_g$ is the group index, $R$ is the radius of the microring resonator, and $c$ is the speed of light in free space.Therefore, in practice, the splitting quality factor, $Q_s$, can be used as a measure of the coupling strength.

In both cases shown in Figure 70(a) and Figure 70(b), the clockwise and the

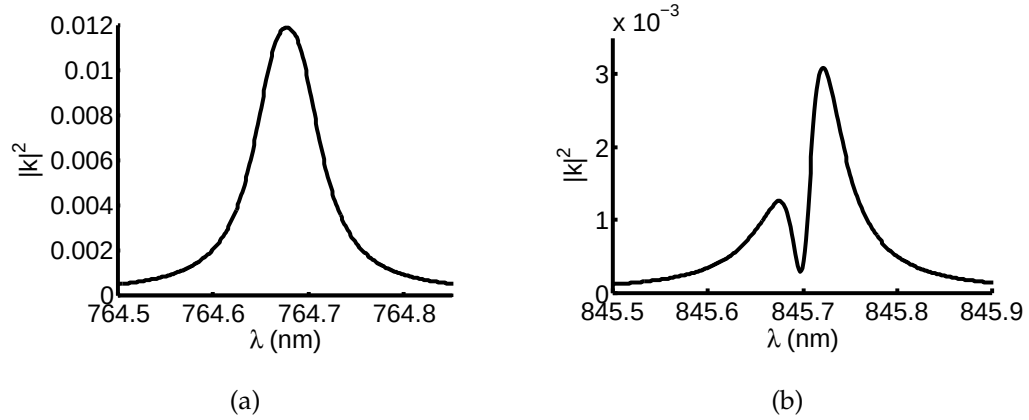


(a) (b)

**Figure 70:** Coupling efficiency for a hybrid double-resonator with the same parameters as those used in Figure 68, in the weak coupling regime, (a) near the LSPR resonance peak and (b) far from the LSPR resonance peak.

counter-clockwise modes exist in the microresonator and part of the input power is reflected back through the input waveguide.

So far, the hybrid resonator is studied almost independently of the loading effect of the bus waveguide by assuming a large $Q_c$ between the bus waveguide and the hybrid resonator. However, the coupling between the bus waveguide and the hybrid double-resonator must be considered. It can be seen from Figure 70(a) that when the gap between the bus waveguide and the hybrid resonator is large, i.e., $Q_c = 10^6$, even at the LSPR peak resonance wavelength, only 1.2% of the input power is coupled to the plasmonic nanoresonator mode. To optimize the coupling between the bus waveguide and the hybrid double-resonator structure, the coupling efficiency to the plasmonic nanorod, $|k|^2$, is plotted versus coupling quality factor, $Q_c$, between the waveguide and the hybrid double-resonator structure in Figure 71 for a hybrid structure with the same parameters as those used in Figure 69.

The coupling efficiency is maximized at a coupling $Q$ of $Q_c = 6.7 \times 10^3$. The maximum coupling efficiency is more than 50%. Under the optimum conditions, i.e., $Q_c = 6.7 \times 10^3$, the coupling efficiency spectrum is plotted in Figure 72(a), as

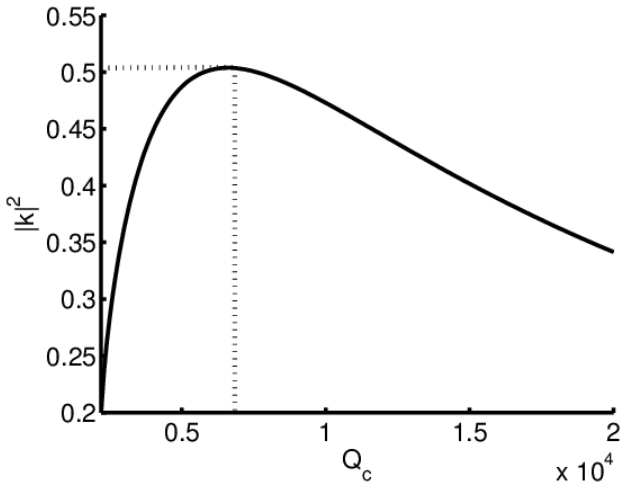


**Figure 71:** Coupling efficiency for the hybrid double-resonator structure discussed in Figure 70 versus the coupling quality factor, $Q_c$, between the waveguide and the hybrid resonator structure.The coupling efficiency is maximized at $Q_c = 6.7 \times 10^3$.

the coupling efficiency , $|k|^2$, versus wavelength.

It can be seen that the envelope of the coupling efficiency spectrum follows the broadband resonance feature of the plasmonic nanoresonator LSPR mode on an equivalent waveguide. As shown in Figure 72(b), this broadband envelope is sampled by the sharp resonances of the photonic microresonator. Using the proposed hybrid resonator structure, more than 50% coupling efficiency is possible to the plasmonic gold nanorod over several modes of the hybrid resonator structure that are separated by the free spectral range (FSR). The FSR = 1.2 $nm$ corresponds to the fundamental radial order modes of the microring resonator.

The presented analysis method, which is formulated in a matrix form, can be easily extended to the case where we have multiple plasmonic nanoresonators integrated with the photonic microresonator.

So far, we have shown that by optimizing the hybrid resonator structure, the coupling efficiency can be more than 50%, assuming $Q_0 = 1.5 \times 10^4$. The coupling efficiency to the resonance mode of the plasmonic nanoresonator structure depends on the coupling quality factor between the waveguide and the hybrid

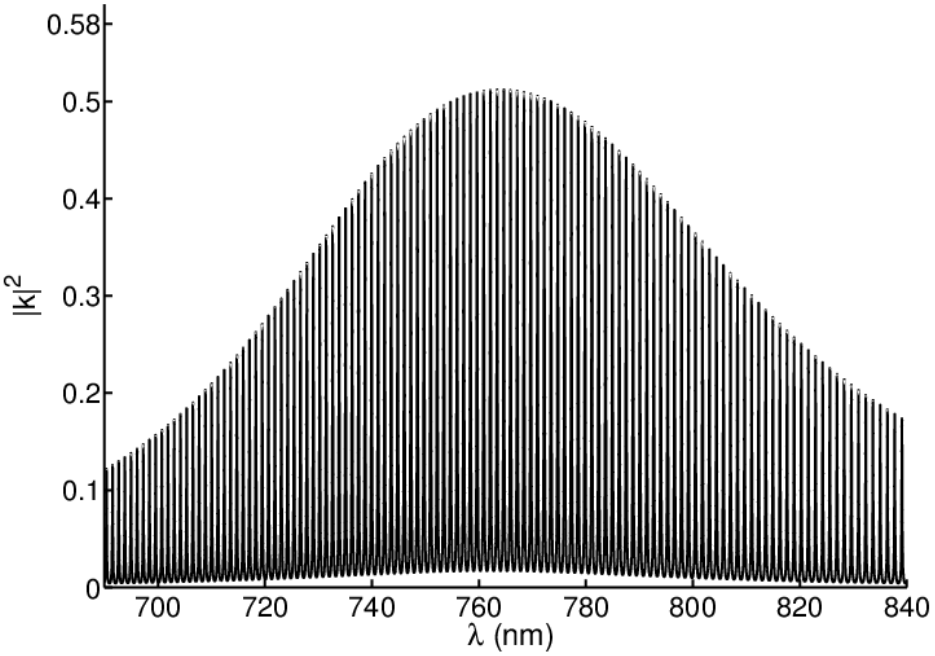


(a)

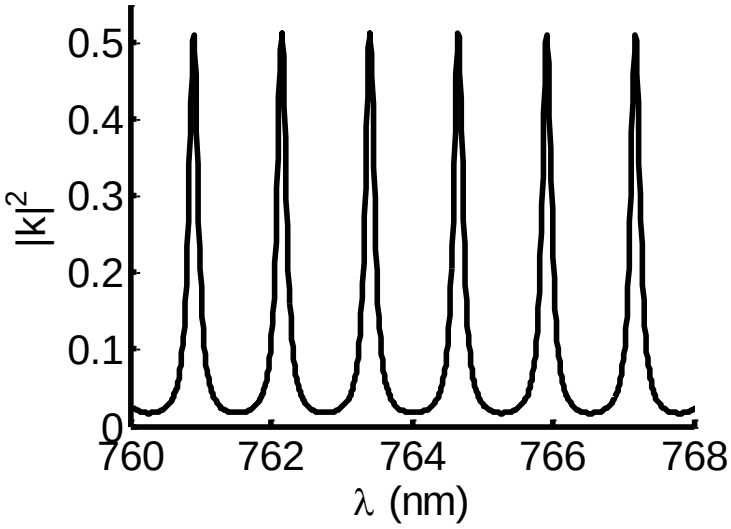


(b)

**Figure 72:** (a) Coupling efficiency spectrum over a large range of wavelengths under optimized conditions for the hybrid resonator structure discussed in Figure 71 (i.e., $Q_c = 6.7 \times 10^3$). (b) The enlarged portion of the coupling efficiency spectrum near the plasmonic resonance peak, where several different modes of the hybrid structure can be seen having large coupling efficiencies.

resonator, $Q_c$, the intrinsic quality factor of the photonic microring resonator, $Q_0$, as well as the coupling between the photonic microresonator and the plasmonic nanoresonator. It was shown that the coupling between the waveguide and the hybrid resonator structure can be optimized to maximize the coupling efficiency to the plasmonic nanoresonator for a specific $Q_0$ of the photonic microresonator. In an ideal scenario, when the photonic microresonator is perfectly lossless, i.e., $Q_0 = \infty$, the coupling efficiency to the plasmonic nanoresonator can be obtained as

$$|k|^2 = |\kappa|^2 \frac{1 - (t_p^2 + r_p^2)}{|1 - 2tt_p + t^2(t_p^2 + r_p^2)|^2}. \tag{17}$$

It can be seen that when the plasmonic nanoresonator is lossless, i.e., $t_p^2 + r_p^2 = 1$, the coupling efficiency is zero. In this case, there is no scattering or absorption of light by the nanoparticle; no power is removed from the lightwave circulating around the photonic microresonator and the plasmonic nanoresonator would only cause the coupling of the clockwise and the counterclockwise modes of the photonic microresonator. In practical situations, however, the scattering and the absorption cross section of plasmonic nanoresonators are nonzero and the coupling efficiency indicates the fraction of the input power in the waveguide that is coupled to the localized resonance mode of the plasmonic nanoresonator. Usually, $r_p \ll t_p$, since the extinction cross section of the plasmonic nanoresonators is very small. From Equation 17, when $r_p \to 0$, the coupling efficiency approaches 100% asymptotically for an optimum value of $t = t_p$, or alternatively, $Q_c = \frac{4\pi^2 R n_g}{\lambda_0(1-t_p^2)}$. Here, we can see the advantage of using the photonic microresonator, where a reasonable $Q_c$ results in efficient coupling of the input lightwave to a very low-$Q$ plasmonic nanoresonator. Therefore, in an ideal situation, when the photonic microresonator is lossless, it is possible to couple almost all of the input light power to the localized surface plasmon resonance of the plasmonic nanoresonator mode. The only limitation would be the reflected power that is coupled back to the input

waveguide through the clockwise propagating mode of the resonator. In practice, however, the photonic microresonator is not lossless and has a limited intrinsic quality factor, $Q_0$. To study the effect of the photonic microresonator intrinsic quality factor on the coupling of the lightwave to the plasmonic nanoresonator mode, the coupling efficiency is plotted versus $Q_0$ and $Q_c$ in Figure 73 at the resonance peak wavelength of $\lambda_0 = 764.65\ nm$.

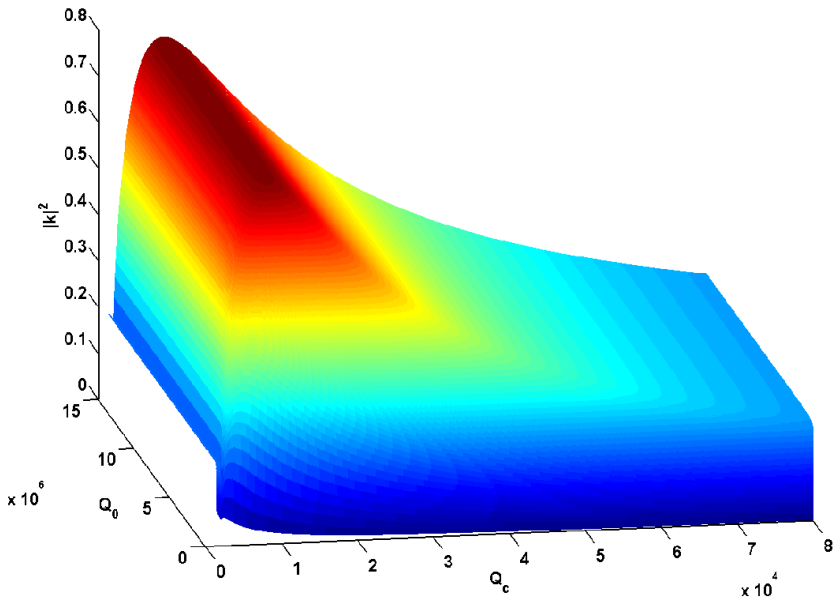


**Figure 73:** Coupling efficiency as a function of the intrinsic quality factor ($Q_0$) and the coupling quality factor ($Q_c$) at the resonance peak wavelength of $\lambda_0 = 764.65\ nm$. It can be seen that the coupling efficiency has a maximum at each $Q_0$ for a specific value of $Q_c$.

It can be seen from Figure 73 that the coupling efficiency has a maximum for each value of $Q_0$ at a specific $Q_c$ from the waveguide, where the coupling of the lightwave from the bus waveguide to the hybrid resonator system and consequently from the photonic resonator to the plasmonic nanoresonator is maximized. It can also be observed that when $Q_0$ is increased, the coupling efficiency is increased. For example, at $Q_0 = 1.5 \times 10^7$ and $Q_c = 8.6 \times 10^3$ the coupling efficiency can reach a value of more than 77%. Even at these very high

$Q_0$ values, where the loss of energy in the photonic microresonator is negligible, part of the lightwave is coupled to the clockwise travelling mode of the photonic microring resonator and is ultimately coupled back to the bus waveguide as reflection. Achieving such high intrinsic quality factors is not easily possible in practice with the current quality of materials and fabrication processes. To investigate how practical the proposed hybrid structure is in efficiently coupling the lightwave to the plasmonic nanoresonator mode, the optimization surface, presented in Fig. 73, is plotted in the form of iso-$|k|^2$ contours in Fig. 74. It can be seen for example that at a $Q_0 = 1.37 \times 10^5$ and $Q_c = 8.6 \times 10^3$, the coupling efficiency is 73%, which still is large. The intrinsic quality factor of $Q_0 = 1.37 \times 10^5$ and the coupling quality factor of $Q_c = 8.6 \times 10^3$ are practically achievable. The proposed hybrid structure can also be extended to other photonic microresonator structures such as microdisk resonators that have higher quality factors. However, microdisk resonators usually have multiple radial modes, which makes the design more difficult. Other photonic microresonators such as microtoroids, microspheres, standing wave resonators, and photonic crystal cavities [53, 98] can also be used in the proposed architecture.

It should be noted that the total energy that is coupled to the resonance mode of the plasmonic nanoresonator and results in large near-field enhancements is partly absorbed by the metallic nanoresonator, and is partly scattered. Depending on the application of interest, the plasmonic nanoresonator can be designed to have either a large absorption cross section or a large scattering cross section. When a material is interacting with the enhanced near-field of the plasmonic nanoresonator, the energy can also be absorbed by the material. Here, we have demonstrated the results for a gold nanorod. The plasmonic nanoresonator shape, size, and material can be used to design different plasmonic nanoresonators with different absorption and scattering properties. It should also be noted that we

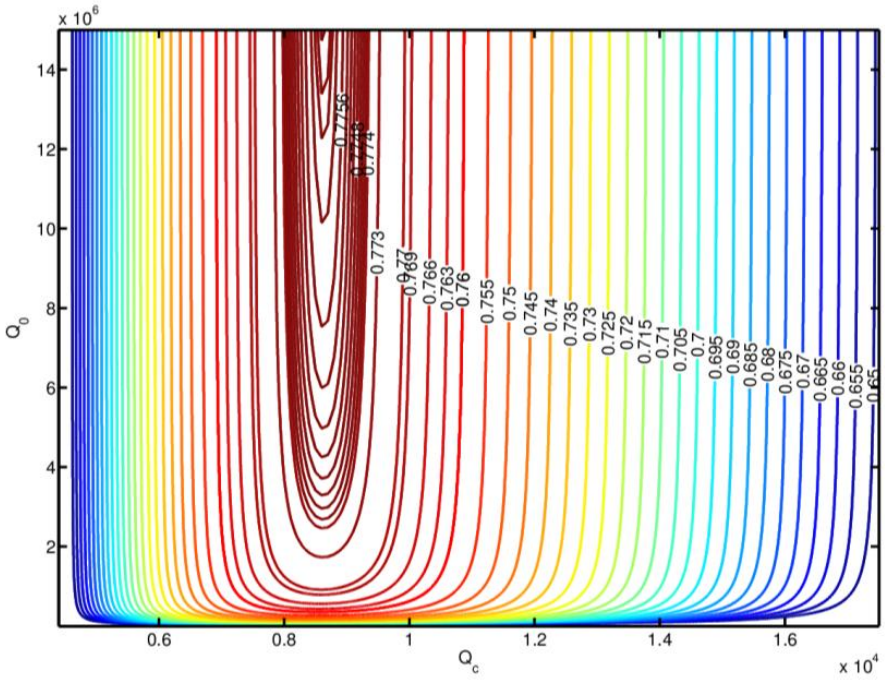


**Figure 74:** Contours of constant coupling efficiency as a function of the intrinsic quality factor, $Q_0$, and the coupling quality factor, $Q_c$ at the resonance peak wavelength of $\lambda_0 = 764.65\ nm$. It can be seen that the coupling efficiency has a maximum at each intrinsic quality factor, $Q_0$, for a specific coupling quality factor, $Q_c$.

have optimized the coupling of the lightwave to the dipole resonance mode of the plasmonic nanoresonator. The coupling efficiency can be optimized to higher order resonance modes, as well.

The large coupling efficiency to a single plasmonic nanoresonator mode greatly improves the field enhancement and signal-to-noise-ratio. This makes it possible to do practical individual plasmonic nanoresonator sensing by using low input powers. Also, the proposed hybrid structure can be realized on a chip, and is not alignment sensitive. Once the structure is implemented, excitation of the bus waveguide guarantees the excitation of the LSPR mode of the plasmonic nanoresonator. Also, the enhanced extinction of the hybrid resonator modes can be measured at the output of the bus waveguide. This eliminates the need for a

bulky microscope with precise alignment control and a very sensitive detector to interrogate single plasmonic nanoresonators.

In the proposed hybrid resonator structure, the photonic microresonator with a large intrinsic quality factor, $Q_0$, facilitates the coupling of the lightwave from the bus waveguide to the plasmonic nanoresonator. In analogy to microwave antennas, the high-Q photonic microresonator can be considered as an impedance matching circuitry that optimizes the coupling of the input power to the plasmonic nanoresonator, which can be considered as a nanoantenna.

## *5.2 Surface Plasmon Polariton Resonators Integrated with Photonic Resonators*

A hybrid integrated plasmonic-photonic waveguide structure was introduced in section 3.2 consisting of photonic ridge waveguides integrated with surface plasmon polariton (SPP) waveguides. In this section, the idea is extended to the case where a photonic microresonator is integrated with a SPP microresonator. In contrast to the structure introduced in section 5.1, the plasmonic resonator is not a nanoresonator; instead, it is an SPP traveling-wave microresonator. In the hybrid SPP-photonic resonator structure, a photonic microresonator is used to trap and enhance the lightwave. Then the lightwave is vertically coupled to an SPP microresonator. This structure benefits from large sensitivity of SPP microresonators and high-Q resonance properties of photonic microresonators. Plasmonic microresonators based on SPPs have been introduced before [42]. Since the propagation loss of SPPs is large, SPP microresonators have usually low quality factors and cannot support sustained high-Q modes. Bumki Min, et al. have shown that by coating a silica microdisk with a layer of silver, whispering gallery SPPs can be supported at the interface of silica and silver, which can have high

quality factors as high as $Q = 1800$ [99]. In this structure, SPP traveling-wave modes are excited inside the structure at the silver-silica interface, and are not accessible outside for light-matter interaction. In the hybrid structure introduced in this section, photonic microresonators with high quality factors are used to partly compensate for the loss of the SPP microresonators and help with sustaining high-Q hybrid modes, which can be used for light-matter interaction with high sensitivity.

Schematic of the hybrid SPP-photonic microresonator is shown in Figure 75(a). It consists of a photonic microring resonator vertically coupled to a plasmonic strip ring resonator supporting SPP traveling-wave modes. A buffer layer separates the SPP resonator and the photonic resonator. The structure will be designed to support SPP traveling-wave modes in the cladding layer on top of the plasmonic layer where strong light-matter interaction can happen. A bus waveguide side-coupled to the hybrid resonator structure is used to carry the lightwave to the vicinity of the hybrid resonator where it can be coupled to the mode of the hybrid structure. This structure can be designed in different wavelength ranges from visible to infrared and in different material platforms. For example, silicon can be used as the photonic material platform for operation in infrared range, and silicon nitride ($Si_3N_4$) can be used for operation in the visible or near infrared range of the spectrum. The plasmonic layer can be made of silver, gold, or any other material that can support SPPs at the wavelength of interest. The application of interest here is sensing; and for most of biological analytes, visible and near infrared are the preferred ranges for sensing since water absorption is very weak in this range. Therefore, $Si_3N_4$ is used as the material for the photonic part and silver ($Ag$) is used as the material for the plasmonic part. Buffer layer is assumed to be silicon dioxide ($SiO_2$) and the cladding layer is assumed to be porous alumina ($p - Al_2O_3$), which can serve as a host material for the molecules of interest that are intended

to interact with the SPPs. The cladding layer can itself be the material of interest that is intended to interact with the SPPs. Figure 75(b) shows a cross section of the hybrid SPP-photonic resonator. The photonic microresonator has a radius $R$ and a cross section ($w \times t_f$). The plasmonic strip ring resonator has a thickness of $t_m$ with the same width as that of the photonic microresonator. The buffer layer has a thickness of $t_b$ and the cladding layer has a thickness of $t_c$.

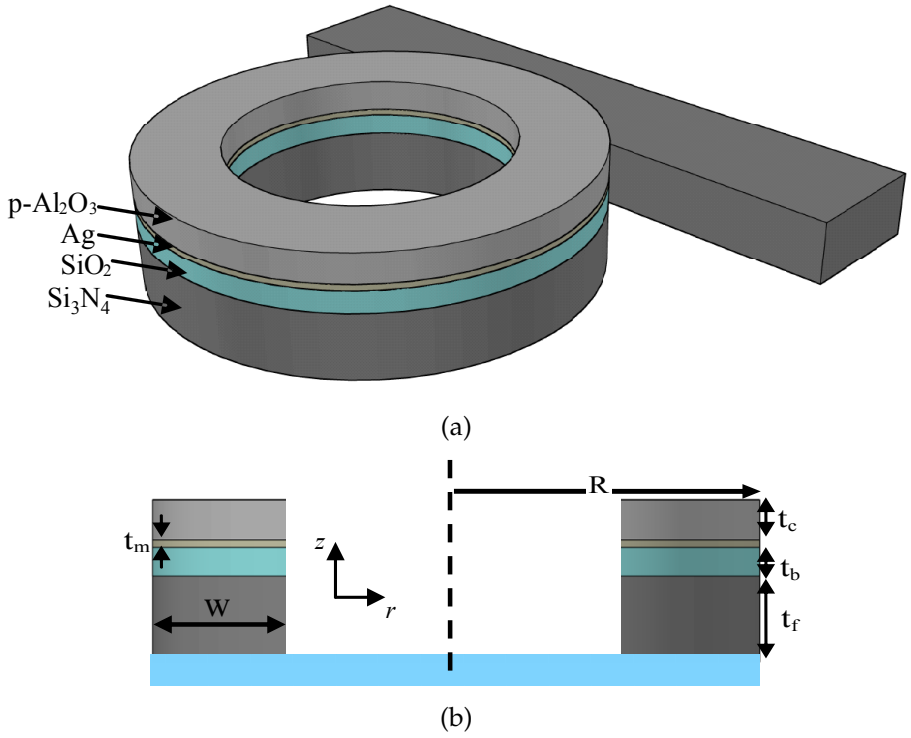


**Figure 75:** Hybrid SPP-photonic microresonator schematic, (a) 3D view showing the bus waveguide and the hybrid resonator structure. (b) 2D view showing a cross section of the hybrid microresonator. Different dimensions are specified on the schematic.

To design and analyze the hybrid resonator structure, finite element method (FEM) is used [84]. Since the structure has cylindrical symmetry, a radial cross section of the hybrid resonator can be analyzed to obtain the resonance modes. The electromagnetic fields for each resonance mode have the form $\mathbf{H} = \mathbf{H}(r,z,t)e^{(-jm\phi)}$ and $\mathbf{E} = \mathbf{E}(r,z,t)e^{(-jm\phi)}$, where $e^{(-jm\phi)}$ shows the azimuthal dependence of the electromagnetic fields, and $m$ is the azimuthal mode order. Therefore, the

azimuthal derivative of electromagnetic fields can be set $\frac{\partial}{\partial\phi} \Rightarrow -jm$ in Maxwell's equations. Maxwell's equations are combined to form Helmholtz equation in terms of magnetic fields, Equation 18. The structure has the same magnetic permeability, $\mu_0$, in all regions, and therefore, magnetic field components are continuous across all the internal interfaces in the simulation domain and are hence easier to solve.

$$\nabla \times \nabla \times \mathbf{H} = {k_0}^2 n^2 \mathbf{H} \tag{18}$$

Equation 18 is a vectorial equation, and the magnetic field has three components, i.e., $\mathbf{H} = \mathrm{H_r}\widehat{r} + \mathrm{H_z}\widehat{z} + \mathrm{H}_\phi\widehat{\phi}$. To further simplify Equation 18, one can use Maxwell's divergence equation, $\nabla \cdot \mathbf{H} = 0$, to obtain the azimuthal component of the magnetic field, $\mathrm{H}_\phi$, in terms of the transverse components, $\mathrm{H_r}$ and $\mathrm{H_z}$, Equation 19.

$$\frac{1}{r}\frac{\partial r\mathrm{H}_r}{\partial r} + \frac{1}{r}\frac{\partial \mathrm{H}_\phi}{\partial \phi} + \frac{\partial \mathrm{H_z}}{\partial z} = 0. \tag{19}$$

Now the cylindrical symmetry of the structure can be used to simplify Equation 19 and obtain $\mathrm{H}_\phi$ as

$$\frac{jm}{r}\mathrm{H}_\phi = \frac{1}{r}\frac{\partial r\mathrm{H}_r}{\partial r} + \frac{\partial \mathrm{H_z}}{\partial z}. \tag{20}$$

From Equation 20, $\mathrm{H}_\phi$ can be substituted in Equation 18 in terms of the transverse components of the magnetic field, $\mathrm{H_r}$ and $\mathrm{H_z}$. Therefore, Helmholtz equation can be solved for the transverse components of the magnetic field. It can be shown that after some mathematical simplifications, Helmholtz equation can be written as

$$\nabla_t \times \left[\frac{1}{n^2}\left(\nabla_t \times (r\mathbf{H}_t) - \widehat{r} \times (\mathbf{H}_t)\right)\right] - \frac{1}{n^2 r}\nabla_t\left[r\nabla_t \cdot (r\mathbf{H}_t)\right] + \left(\frac{m}{n^2 r}\right)\mathbf{H}_t = {k_o}^2 r\mathbf{H}_t, \tag{21}$$

where $\mathbf{H}_t = \mathrm{H}_r\widehat{r} + \mathrm{H_z}\widehat{z}$. This equation is an eigenvalue problem with ${k_0}^2$ as the eigenvalue. For each azimuthal mode order, $m$, a series of eigenvalues corresponding to resonance frequencies of different radial modes can be obtained. Although the divergence equation, Equation 19, is used to simplify the Helmholtz equation in terms of the transverse magnetic field components, still

some spurious solutions are obtained. These spurious solutions can be avoided by separately imposing the divergence equation. Other field components including different electric field components can be obtained using Maxwell's equations from transverse components of the magnetic fields, $H_r$ and $H_z$. Further details of this method is explained in [100]. These equations can be implemented in COMSOL™ environment and the eigenvalue solvers can be used to obtain the resonance modes. For hybrid SPP-photonic resonators with large radii, the main source of loss is the plasmonic layer material loss, and radiation loss can be neglected. Therefore, perfect electric field (PEC) boundary conditions are used for the exterior boundaries. For hybrid resonators with small radii, a perfectly matched layer (PML) must be used. Weak boundary conditions [100] are used for interior boundaries to satisfy the continuity of the tangential electromagnetic fields across the interfaces. The structure is meshed with triangular mesh elements with scalar nodal elements and quartic scalar Lagrange functions. To analyze the structure accurately, the material dispersion of the plasmonic layer is considered by implementing the frequency dependence of the metal permittivities from empirical results of Johnson and Christy [101] in the aforementioned equation system. Then, the structure is analyzed iteratively by first assuming an initial guess for the resonance frequency and setting the material properties at that frequency. Then, the obtained resonance frequency from FEM is used as a new initial point. This procedure is repeated until the solution converges.

To obtain the first initial guess for the resonance frequency, and to solve the eigenvalue problem using FEM to obtain $H_r$ and $H_z$, an approximation of the resonance condition can be used as

$$k_0 n_{eff}(2\pi R_c) = 2m\pi, \tag{22}$$

where $k_0 = \frac{2\pi}{\lambda_0}$ is the free space wavenumber, $m$ is the azimuthal mode order, $R_c = R - \frac{w}{2}$ is the center radius of the ring resonator, and $n_{eff}$ is the effective

index of the hybrid equivalent waveguide. The hybrid equivalent waveguide has the same dimensions as the cross-sectional dimensions of the microring resonator. The hybrid equivalent waveguide can be analyzed using the results discussed in section 3.2. As an example, a 7.2 $\mu m$ ($R = 7.2\ \mu m$) hybrid SPP-photonic microresonator is analyzed with $Si_3N_4$ as the photonic material, $SiO_2$ as the buffer layer, silver as the plasmonic layer, and porous alumina ($p - Al_2O_3$) with a refractive index of $n_c = 1.59$ as the cladding layer. The width of the resonator is assumed to be $w = 400\ nm$, the buffer layer thickness $t_b = 120\ nm$, the silver layer thickness $t_m = 50\ nm$, the photonic layer thickness $t_f = 20\ 0nm$, and the cladding layer thickness $t_c = 200\ nm$. The radius is chosen as a practical value for a compact structure. Too small radius results in large bending loss, while too large radius results in a large size and consequently larger plasmonic loss. It was shown in Section 3.2 that the equivalent hybrid waveguide structure has two modes at each wavelength. One of the modes (lower branch mode) has a lower effective index and lower propagation loss, and the other one has a larger effective index and larger loss. To design the hybrid SPP-photonic resonator, the mode with lower propagation loss is preferred as it results in higher quality factors. It was shown in Figure 37(a) that at the wavelength of $\lambda = 650\ nm$, the hybrid waveguide structure has a mode with an effective index of $n_{eff} = 1.616 - j0.0017$. By using this effective index in equation 22, it can be seen that for an azimuthal mode order of $m = 114$, an initial value for the resonance wavelength can be obtained as $\lambda_0 = 623.47\ nm$. This initial value is used in the FEM simulations and after a few iterations, a resonance wavelength of $\lambda_0 = 625.44\ nm$ is obtained. The free spectral range of the resonance mode for this structure calculated from FEM simulations is 4.54 $nm$. It should be noted that the hybrid resonator structure has another (undesired) mode that corresponds to the mode of the hybrid waveguide with higher effective index. This mode has a higher resonance wavelength and is not considered in our

design as it has considerably higher loss, and thus lower quality factor. The good agreement between the numerical result for the resonance wavelength obtained using rigorous FEM simulation and the result obtained from the effective index modeling using equivalent waveguide analysis suggests that the effective index modeling is a good approximation for the initial guess of FEM analysis and is useful to design and analyze the structure. The normalized radial field profile ($H_r$) for the hybrid resonator structure calculated using FEM simulations is plotted in Figure 76.

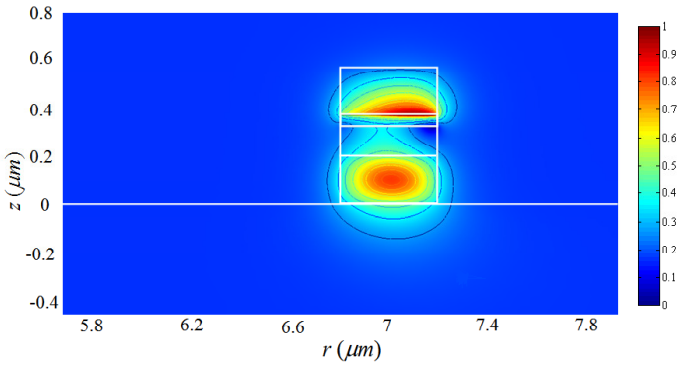


**Figure 76:** Mode profile of the hybrid ring resonator ($R = 7.2\mu m, w = 400\ nm, t_f = 200\ nm, t_m = 50\ nm, t_b = 120\ nm, t_c = 200\ nm$). The normalized radial component of the magnetic field ($H_r$) is illustrated in this figure.

It can be seen from Figure 76 that the SPP traveling mode and the dielectric traveling mode are strongly coupled to each other and form a supermode. The excitation of the SPP at the metal-cladding interface causes the enhancement of the electromagnetic field at the metal-cladding interface, where the resonator mode has maximum interaction with the target molecules. Another interesting feature in Figure 76 is the fact that the mode is inclined towards the outer radius. In fact, the mode of the metal strip microring is radiative at this radius without being coupled to a dielectric microresonator, and the bend radius at which it can support a bound mode is much larger than what is used here. However, the hybrid structure in which the dielectric microresonator and the SPP microresonator are strongly

coupled has a large enough effective index to support a non-radiative mode.

## *5.3 On-chip Sensing using Hybrid Plasmonic-photonic Resonators*

Two types of hybrid plasmonic-photonic resonators have been introduced in this chapter. The first one was a hybrid plasmonic-photonic double-resonator consisting of plasmonic nanoresonators integrated with a photonic microresonator. It was shown that by properly designing the structure, light is efficiently coupled to the plasmonic nanoresonator and a very large field enhancement is possible over several modes of the structure. This structure can be used to make enhanced on-chip Raman sensors. The second type was an SPP-photonic hybrid resonator consisting of a microresonator coupled with an SPP microresonator. This structure supports a hybrid high-Q mode that has the large sensitivity of the SPP resonator as well as the high-Q properties of the photonic microresonator. Therefore, it can be used as an on-chip highly sensitive refractive index sensor. In this section, the application of these two hybrid resonator-based structures for sensing is discussed.

### 5.3.1 On-chip SERS using Integrated Hybrid NanoPlasmonic-photonic Microresonator Structures

In this section, the application of the hybrid plasmonic-photonic double-resonator introduced in section 5.1 as an on-chip Raman sensor is discussed from a system level point of view. The performance is then compared with other implementations, and the advantage of the proposed hybrid device for realization of on-chip SERS will be discussed. It was shown in section 5.1 that by properly designing the structure, the LSPR mode of the plasmonic nanoparticles integrated with photonic microresonators can be efficiently excited. The coupling efficiencies of more than 73% to a single plasmonic nanoresonator is achievable in such structures. This high level of coupling efficiency can greatly enhance the field enhancement, and

consequently, the Raman signal emission efficiency and the overall signal-to-noise-ratio (SNR). The SNR in a Raman spectrometer can be obtained as

$$SNR = \frac{\eta_q \eta_0 P_R}{(\sigma_S{}^2 + \sigma_B{}^2 + \sigma_d{}^2 + \sigma_F{}^2 + \sigma_r{}^2)^2}, \tag{23}$$

where $\eta_q$ is the detector quantum efficiency, $\eta_1$ is the collection efficiency of the optics, including the spectrometer diffraction efficiencies and transmission of the lenses. $\sigma_S{}^2$ indicates the signal shot noise, $\sigma_B{}^2$ indicates the background shot noise, $\sigma_d{}^2$ indicates the detector dark noise, $\sigma_F{}^2$ shows the flicker noise arising from random variations in laser power, and $\sigma_r{}^2$ indicates the readout digitization noise. The dominant noise sources are usually the shot noises and the detector dark noise. Since the Raman signal emitted from molecules are usually quite very weak, having a reasonable SNR for detection of a few molecules is challenging. The Raman signal emitted from a sample of density $D$ that is illuminated by a laser power $P_0$, which is tightly focused on a spot of radius $r$, Figure 77(a), can be obtained as

$$P_R = \frac{P_0}{\pi r^2} \sigma D dz, \tag{24}$$

where $\sigma$ is the Raman scattering cross section, and $dz$ is the depth of the sample. To get an idea about the Raman signal level from low concentration samples (and potentially single molecules), the Raman signal emitted from a single Benzene molecule for a Stokes band of $922 cm^{-1}$ with a Raman scattering cross section of $\sigma = 28 \times 10^{-30} cm^2.sr^{-1}$ when illuminated with a $50mW$ laser at a wavelength of $\lambda = 785\ nm$ that is tightly focused to a $4\mu m$ spot can be calculated to be $P_R = 0.0044 photon.sr^{-1}.sec^{-1}$. This very low level of a signal can hardly be detected even with the state of the art cooled CCD detectors, specially when the collection efficiency is taken into account.

If a single plasmonic nanoresonator is used to enhance the Raman emitted signal of this molecule, the Raman emitted signal is enhanced by a factor of

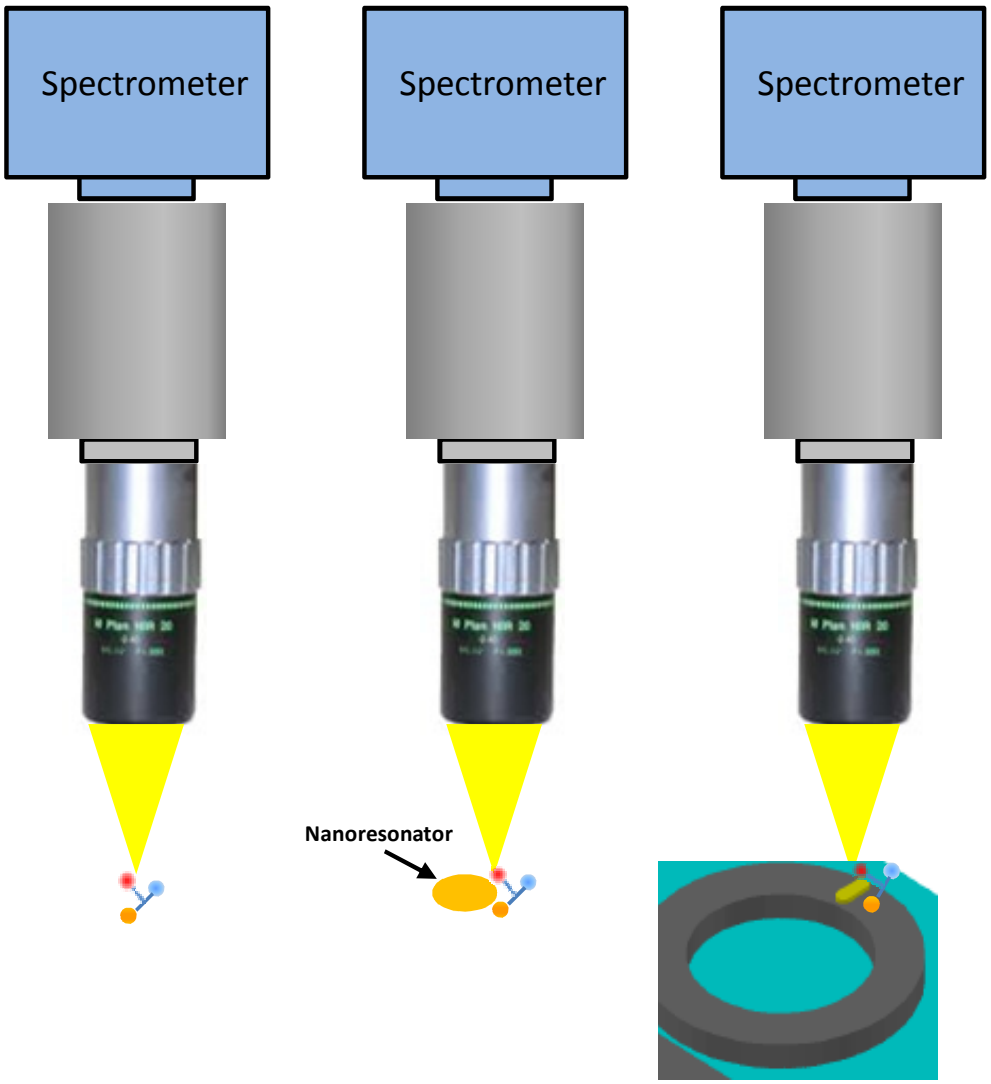


**Figure 77:** (a) Raman sensing of a single molecule using a microRaman system consisting of a microscope assembly and a spectrograph (b) Raman sensing of a single molecule next to a plasmonic nanoresonator using a microRaman system. Plasmonic nanoresonator enhances the Raman emission in this SERS arrangement. (c) Raman sensing of a single molecule using the hybrid plasmonic-photonic double-resonator.

$G_{SERS} = |E(\lambda_p)|^2 |E(\lambda_R)|^2$, where $\lambda_p$ and $\lambda_R$ are the pump and the Raman wavelengths, respectively. It has been shown that the field intensity near plasmonic nanoresonators can be enhanced by a factor of $10^3 - 10^5$. Also, the charge transfer between the molecule and the plasmonic nanoresonator results in another level of Raman emission enhancement called chemical enhancement. Altogether, enhancements on the order of $10^{10} - 10^{14}$ can be achieved. The Raman emitted signal from a single molecule attached to a single plasmonic nanoresonator, Figure 77(b), can be obtained as

$$P_R = \frac{P_0}{\pi r^2} \sigma_{NP} G_{SERS} {\eta_0}^2 \sigma, \tag{25}$$

where $\sigma_{NP}$ is the plasmonic nanoparticle extinction cross section, and $\eta_0$, a factor less than or equal to one accounts for the ratio of the enhanced intensity that is made available to the molecule of interest. It can be seen that although the SERS enhancement can greatly enhance the Raman emitted signal, still the fraction of power coupled to the plasmonic nanoresonator can be small due to the small value of $\sigma_{NP}$. The typical values of plasmonic nanoresonator extinction cross sections at the resonance are very small. For example, a nanorod with an effective radius of 21.86 $nm$ and an aspect ratio of 3.9 has an extinction cross section of $3 \times 10^{-14} m^2$. Therefore, only 0.24% of the input power is coupled to the resonance mode of this plasmonic nanoresonator, when illuminated with a laser focused to a $4\mu m$ spot. This shows that most of the optical power is lost and is not coupled to the plasmonic nanoresonator mode. In the proposed hybrid double-resonator sensor, we can achieve more than 73% coupling efficiency to a single plasmonic nanoresonator. Compared to a single plasmonic nanoresonator, the proposed structure shows more than two orders of magnitude enhancement. This means that the $SNR$ as defined in Equation 23 is improved by more than two orders of magnitude compared to SERS using a plasmonic nanoresonator alone. This can greatly relax the stringent requirements for Raman sensing systems such as

using of cooled CCD detectors, or high-power laser sources. The proposed on-chip Raman sensor can be used in the arrangement shown in Figure 77(c), where the Raman emitted signal is collected out of plane. It can also be designed in such a way that the hybrid double-resonator has modes in the frequency range covering the Raman signal band of interest. If the density of states and the coupling is designed properly, the Raman emitted signal can be coupled back to the hybrid double-resonator and monitored at the waveguide output.

### 5.3.2 On-chip Refractive Index Sensing using Integrated Hybrid SPP-photonic Microresonator Structures

Bulk SPPs can be excited at the interface of a metal and a dielectric. SPPs are localized to the surface of the metal layer, and thus, are very sensitive to the local refractive index changes. They have been widely used for sensing binding kinetics and changes in mass or refractive index. The principle of operation of surface plasmon resonance (SPR) sensors is based on the change of angle or wavelength under which SPPs are excited [16]. SPPs are usually excited in SPR sensors using prisms in arrangements such as the ones discussed in Figure 36. SPR sensing is now a common sensing method for real time monitoring of binding kinetics and is available in commercial instruments such as Biacore™. Different implementations of SPR sensors have been proposed both in bulk form [16, 22], and using guided wave optics such as planar waveguides [23] and fiber optics [24]. These sensors have shown a promise for fast and effective label-free biosensing and have been used in many biomedical studies [1]. SPR sensors are usually interrogated by monitoring the change of resonance angle or resonance frequency. Although the resonance peak shift is very large for small changes of refractive index in SPR sensors, the resonance lineshape is broad, which limits the accuracy in detecting the peak location. On the other hand, ultrahigh-Q photonic microresonators have been used for refractive index sensing. Although the resonance lineshape of

these resonators is usually narrow, they have relatively small sensitivities [19,20]. The hybrid SPP-photonic resonator structure introduced in section 5.2 supports a sustained and relatively high-Q hybrid plasmonic-photonic mode. The mode structure of interest, shown in Figure 76, has two major parts. Part of the mode is confined in the dielectric core as the photonic mode, and the rest is concentrated on the surface of the plasmonic layer as the SPP mode. The hybrid structure proposed here benefits from the large sensitivity of SPPs and high-Q properties of the photonic resonance mode. Therefore, this structure can have a very small detection limit. The schematic of the hybrid SPP-photonic sensor is illustrated in Figure 78.

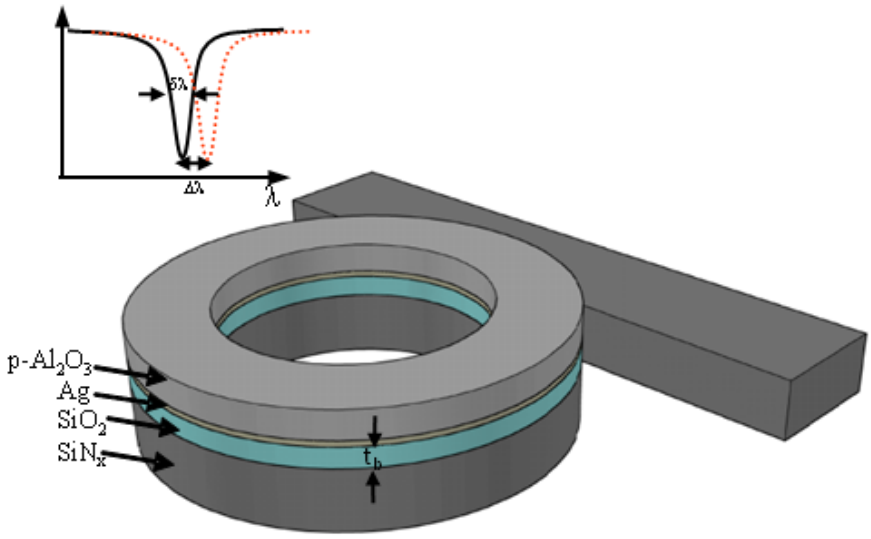


**Figure 78:** Schematic of the hybrid SPP-photonic resonator sensor. The cladding layer is porous alumina, which acts as a host for target molecules.

The cladding layer is assumed to be porous alumina ($p - Al_2O_3$), which acts as a host for target molecules. The porosity of this layer can be chosen according to the size and characteristics of the target molecules. The thickness of the porous cladding layer, $t_c$, effectively determines the index of the medium above the metallic layer, which in turn affects the effective index of the SPP mode. It has been shown that $t_c = 200\ nm$ results in a high sensitivity in a bulk SPR sensor

[102]. Therefore, as a practically reasonable value, $t_c = 200\ nm$ is assumed in all the simulations. When target molecules are adsorbed to the walls of the pores inside the $p - Al_2O_3$ layer, the average refractive index of the cladding is changed and consequently, the resonance wavelength of the resonator shifts. The cladding porous layer not only acts as a host for target molecules, but also enhances the performance of the sensor. It has been shown that using a high-index porous cladding layer such as $p - Al_2O_3$ or $p - TiO_2$ on top of conventional bulk SPR sensors greatly enhances their response [25,102,103]. Like other sensing platforms, different surface coatings can be used on the pore walls of the proposed sensors for target analyte binding; and depending on the surface coating and the target analyte of interest, the sensor can be either reusable or disposable [104]. The transmission spectrum of the bus waveguide side-coupled to the hybrid resonator exhibits a dip at the resonance wavelength of the hybrid structure. The resonance wavelength shifts as the target molecules are adsorbed in the cladding layer, and this shift can be tracked by monitoring the spectral location of the relatively high-Q resonance feature of this resonator at the output of the bus waveguide. The sensitivity, $S$, of this hybrid optical sensor is defined as the resonance wavelength shift per unit refractive index change ($S = \frac{\Delta\lambda}{\Delta n}$). To evaluate the sensitivity of the hybrid resonator structure, the cladding layer refractive index is changed and the shift of the resonance wavelength is calculated using FEM simulations. All the parameters and material properties of this structure are assumed to be the same as those of the structure discussed in section 5.2. The initial refractive index of the $p - Al_2O_3$ is assumed to be 1.59, which according to Maxwell-Garnett approximation [103,105], corresponds to a pore radius of 7.5 $nm$ and pore density of $5 \times 10^{10} cm^{-2}$. The cladding refractive index is increased to 1.608 in small steps of $\Delta n = 10^{-3}$. For the FEM simulations, the domain of the solution is meshed with triangular elements with quartic Lagrange functions. To ensure the convergence of the results, the

average size of the elements in the simulation are 15 $nm$ in the $Si_3N_4$ layer, 12 $nm$ in the buffer layer, 5 $nm$ in the metal layer, and 6 $nm$ in the cladding. The calculated resonance wavelength shift versus the refractive index change of the cladding is plotted in Figure 79 for different buffer layer thicknesses, $t_b$. The slope of each curve in Figure 79 represents the sensitivity of the sensor for the corresponding value of $t_b$. It can be seen that when the buffer layer thickness is decreased, the sensitivity is increased. In this case, the SPP mode and the guided mode of the dielectric resonator are coupled more strongly, and a stronger field interacts with the molecules. On the other hand, as the buffer layer thickness is increased, the coupling between the two modes becomes weaker and the sensitivity decreases.

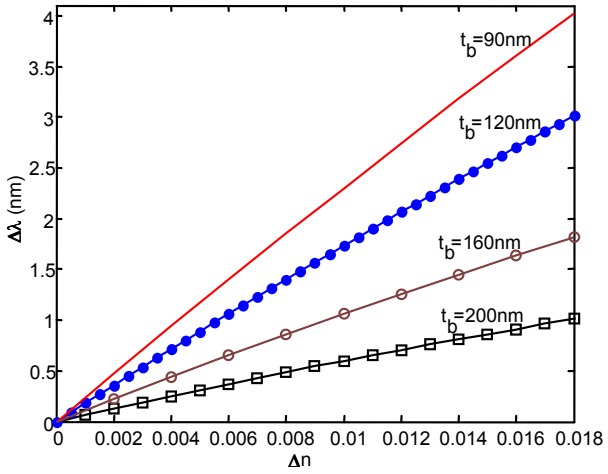


**Figure 79:** Spectral shift of the resonance versus refractive index changes of the cladding layer for different buffer layer thicknesses. The dimensions are $R = 7.2\mu m, w = 400\ nm, t_f = 200\ nm, t_m = 50\ nm, t_b = 120\ nm, t_c = 200\ nm$.

The detection limit of the sensor ($DL$) depends on the sensitivity, $S$, as well as the resolution of the sensor, $R$ [1],

$$DL = \frac{R}{S} \tag{26}$$

The resolution, $R$, is proportional to the linewidth of the resonance, ($\delta\lambda$), and inversely depends on the signal-to-noise ratio in the system, which is determined

based on the detection mechanism. To evaluate the performance of the proposed sensor, the linewidth of the resonance must also be investigated. In the proposed structure, the sources of resonator energy loss that contribute to the broadening of the lineshape are mainly (i) the SPP mode loss originating from the metal material loss, (ii) scattering loss from fabrication imperfections and sidewall roughness, (iii) radiation loss, and (iv) the coupling of the energy to the waveguide. In our calculations, we have considered the effect of SPP mode loss by considering the frequency dependent metal material loss from empirical data given in [101]. Also, the effects of scattering loss from the $Si_3N_4$ ridge sidewalls and the radiation loss are taken into account by assuming a typical intrinsic quality factor of $Q_s = 20000$ for the dielectric ring resonator. When the radius of the ring resonator is not very small for the radiation loss to dominate, $Q_s$ mostly depends on the quality of fabrication and can be improved. However, since the intrinsic quality factor of the proposed hybrid device is dominated by the metal material loss, there is no stringent requirement on the fabrication quality; and the hybrid device is well tolerant to fabrication imperfections. The overall effect of the metal material loss and the scattering loss can be lumped into an intrinsic quality factor ($Q_0 = (Q_m^{-1} + Q_s^{-1})^{-1}$), where $Q_m$ is the quality factor associated with the metal material loss. The coupling loss originating from the coupling to and from the waveguide is considered by using the coupling $Q$, i.e., $Q_c$. The overall quality factor of the hybrid resonator is then the loaded $Q$, i.e., $Q_L = (Q_0^{-1} + Q_c^{-1})^{-1}$, which is maximum under critical coupling condition [106], where $Q_c = Q_0$. The sensitivity, $S$, and the resonator intrinsic quality factor, $Q_0$, are plotted in Figure 80 versus the buffer layer thickness, $t_b$.

It can be seen that as $t_b$ is increased, the sensitivity is decreased, because there would be less mode overlap between the SPP mode and the dielectric mode. On the other hand, the resonator intrinsic quality factor, $Q_0$, increases as $t_b$ is increased,

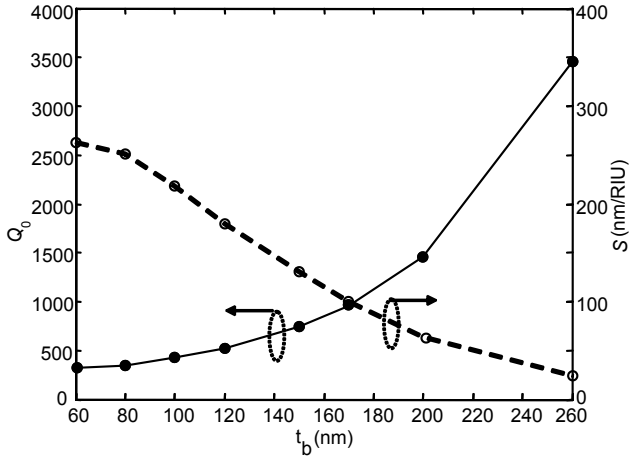


**Figure 80:** Sensitivity and the intrinsic quality factor, $Q_0$ versus the buffer layer thickness for the hybrid SPP-photonic sensor. The dimensions are $R = 7.2\mu m, w = 400\ nm, t_f = 200\ nm, t_m = 50\ nm, t_b = 120\ nm, t_c = 200\ nm$.

because the contribution of metal loss in the overall mode loss is decreased. These two effects compete in opposite direction; smaller $Q_0$ results in wider resonance peaks and more difficulty in detecting a small shift in the resonance wavelength, while larger $S$ results in a larger shift in the resonance wavelength for a given index change. To investigate the effect of this trade-off in the design of the proposed sensor quantitatively, and to obtain an optimum value for the buffer layer thickness, a figure of merit (FOM) is defined as [107]

$$FOM = \frac{S}{\delta\lambda}, \tag{27}$$

where $\delta\lambda$ is the linewidth of the resonance when the loaded $Q$, under the critical coupling condition (i.e., $Q_L = \frac{Q_0}{2}$) is considered (i.e., $\delta\lambda = \frac{\lambda 0}{Q_L}$). The detection limit defined in Equation 27 is inversely proportional to FOM, and the proportionality factor depends on the overall signal-to-noise ratio in the detection mechanism [108]. Therefore, FOM is independent of the signal-to-noise ratio and can be used for the assessment of the performance of any resonance-based refractive index sensing structure. FOM as defined in Equation 27 corresponds to a full

linewidth shift of the resonance wavelength. The larger the FOM is, the better is the performance of the device. One key parameter in the design of the proposed structure is the buffer layer thickness. In order to investigate the effect of this parameter, FOM for the hybrid resonator is plotted in Figure 81 versus the buffer layer thickness. The small value of FOM at very small $t_b$ ($t_b < 100\ nm$) is due to small values of $Q_0$. On the other hand, small values of FOM at large $t_b$ ($t_b > 200\ nm$) is due to small values of sensitivity, $S$.

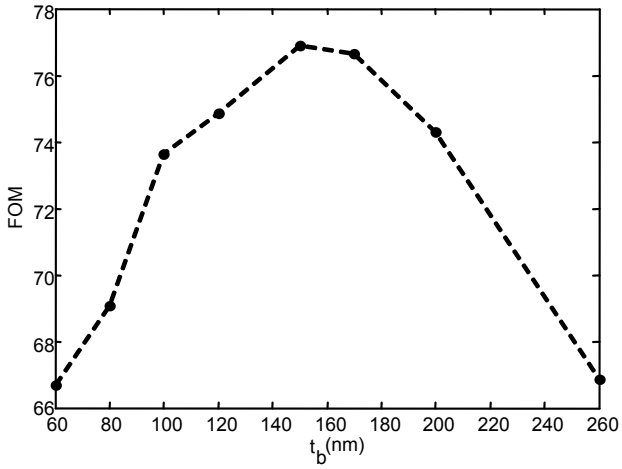


**Figure 81:** Figure of merit ($FOM$) for the hybrid SPP-photonic sensor versus the buffer layer thickness. The dimensions are $R = 7.2\ \mu m, w = 400\ nm, t_f = 200\ nm, t_m = 50\ nm, t_b = 120\ nm, t_c = 200\ nm$.

As is shown in Figure 81, there is an optimum operation region around $t_b = 150\ nm$, where the FOM is maximum. It can be seen in Figure 81 that the optimum operation point is not very sensitive to the buffer layer thickness around the optimum operation thickness. Therefore, in practice slight changes of the buffer layer thickness during the fabrication of the device does not seriously affect the performance.

As a comparison, FOM is calculated for a fiber-based SPR sensor [24] to be FOM = 71.4, which is comparable with the performance of the proposed hybrid sensor (FOM = 76.9). However, this performance is achieved with a much

more compact size and in an integrated platform, which better conforms to the requirements of applications such as point-of-care diagnostic testing. On the other hand, the values of FOM for different localized surface plasmon resonance (LSPR) nanoparticle sensors are reported to be (FOM < 4) [109], which are much less than the values of FOM in the proposed hybrid device. This superior performance is achieved at the expense of a larger sensing volume in the proposed hybrid sensor compared to a single plasmonic nanoparticle LSPR sensor. This means that the amount of required analyte for the proposed sensor is larger than that for single nanoparticle LSPR sensors. For the given example in this section, the sensing medium (i.e., the porous alumina layer) has a total volume of 3.5 $\mu m^3$, which is about four orders of magnitude larger than the sensing medium surrounding a typical LSPR nanoparticle [109]. However, although the total volume of analyte required to bind to the sensor surface is very small for conventional LSPR sensors, delivering a very small amount of analyte to the sensing sites of LSPR nanoparticles is quite challenging [110]. Moreover, coupling of light to individual LSPR nanoparticles is not very efficient. As another alternative technology, on-chip dielectric microresonators have been proposed for label-free index sensing [19, 111–113]. For example, a $Si_3N_4$ microdisk with a radius of $R = 15\ \mu m$ has been reported with a sensitivity of $S \sim 22.8\ nm/RIU$ [111]. The figure of merit for this structure can be calculated to be FOM = 142.8. Another example, is a glass-based microring resonator with a radius of $R = 60\ \mu m$, which has a sensitivity of $S \sim 141\ nm/RIU$ [112]. The FOM can be calculated for this structure to be FOM = 1111. It can be seen that these structures have a larger size compared to the proposed hybrid resonator and the sensitivity is smaller than the proposed hybrid resonator, in the former case [111], and comparable with the sensitivity of the proposed structure, in the latter case [112]. However, these resonators have better performance in terms of the FOM due to their extremely narrow resonance

linewidth. Theoretically, these dielectric resonators have shown a promise for ultra-small detection limits [1]. However, in practice, there are challenges in implementing these resonators, mainly because they are sensitive to fabrication imperfections [1,19].

## 5.4 Experimental Demonstration of Hybrid Plasmonic-photonic Resonators

In this section, the experimental demonstration of hybrid plasmonic-photonic resonators consisting of plasmonic nanoresonators tightly integrated with photonic microresonators is discussed. The fabrication procedure is similar to the fabrication method that was discussed in chapter 4 to realize hybrid on-chip waveguide structures. This two-step EBL fabrication process starts with the first step of EBL to pattern the plasmonic structures, followed by metal deposition and lift-off. In the next step of lithography, photonic structures including the bus waveguides and microresonators are defined and etched. The alignment between the two steps of EBL is critical. The scanning electron micrograph (SEM) of a typical hybrid resonator structure consisting of a 20 $\mu m$ ring resonator integrated with a gold nanorod of dimensions 100 $nm \times 56$ $nm \times 30$ $nm$ is shown in Figure 82. It can be seen that the nanorod is precisely fabricated on the top surface of the microring resonator.

To characterize these hybrid resonator structures, an optical characterization setup is designed and implemented, in which a tunable laser (TLB-6312 New Focus) is used as the source, and a silicon photodetector is used to detect the output signal. The schematic of the characterization setup is shown in Figure 83.

As it can be seen from this schematic, light from a tunable laser source is passed through a polarizer, where it becomes linearly polarized. Then a half-wave plate is used to rotate the polarization state of the input light . Then a lens is used

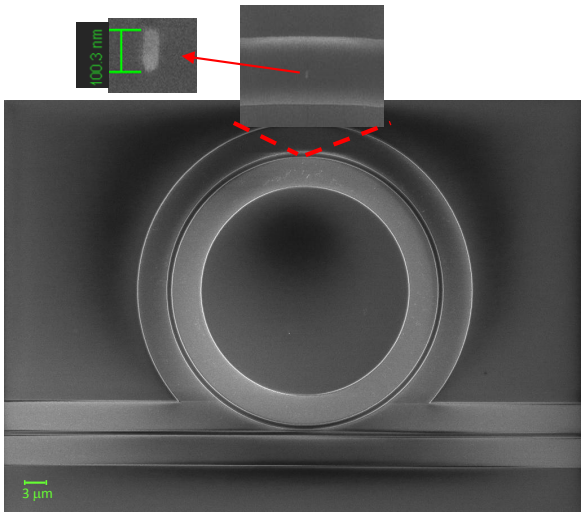


**Figure 82:** The scanning electron micrograph (SEM) of a typical hybrid resonator structure consisting of a 20 $\mu m$ ring resonator integrated with a gold nanorod of dimensions 100 $nm \times 56\ nm \times 30\ nm$.

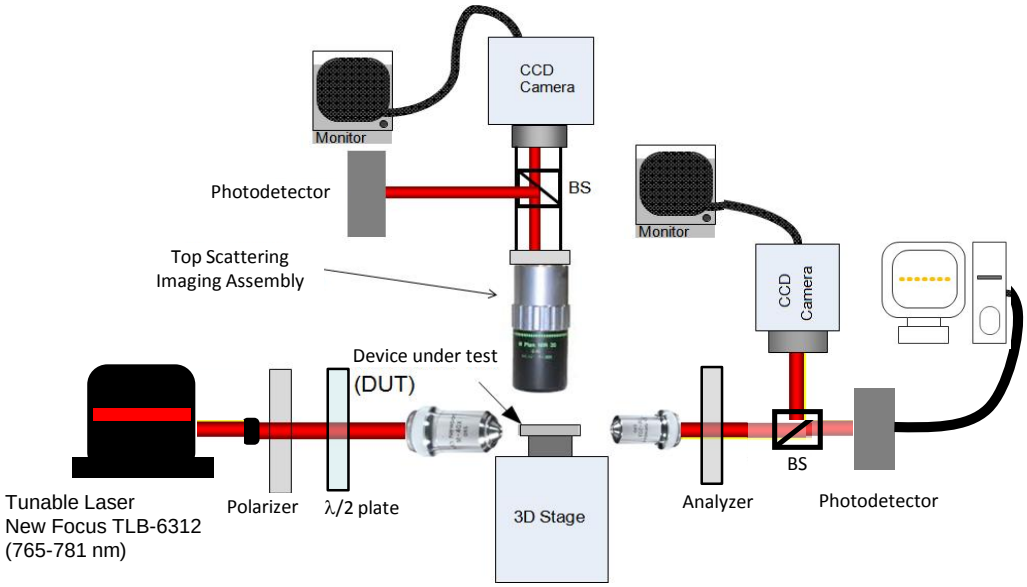


**Figure 83:** The schematic of the in-plane optical setup for characterization of hybrid resonator structures. The setup works with a tunable laser source and a photodetector.

to couple the light to the facet of the bus waveguide on the chip. The output of the waveguide is imaged to a photodetector through the output lens. A camera is used at the output to make sure that the waveguide output spot is aligned with the detector. A microscope is designed on top to facilitate the alignment. It is also equipped with a photodetector to measure the scattered signal from top surface of the devices. The photodetectors are synchronized with the tunable laser through a Labview code. This way, we can keep track of the input laser wavelength, and obtain the spectral response of the devices. The image of this optical characterization setup is shown in Figure 84, where different components are labeled. In the inset of Figure 84, the enlarged image of the part of the setup where the sample is placed is shown along with the input lens, the output lens, and the objective lens of the top microscope.

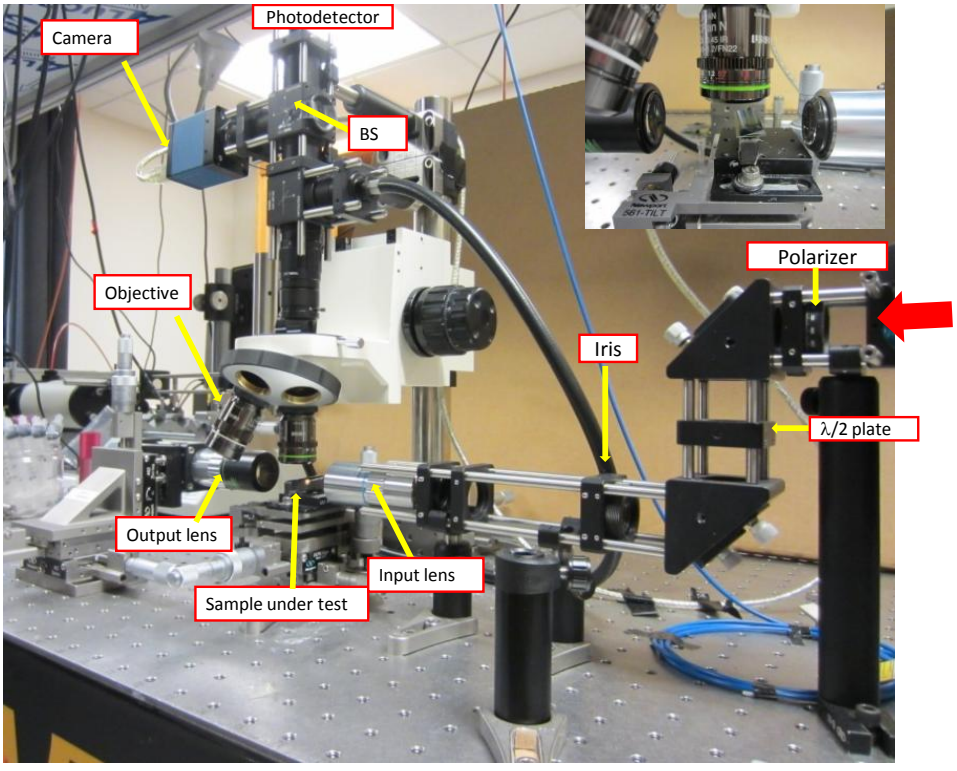


**Figure 84:** The image of the in-plane optical setup for characterization of hybrid resonator structures. The setup works with a tunable laser source and a photodetector. The inset shows the portion of the setup consisting the input, output, and the microscope lens and the sample stage.

After the devices are fabricated on the chip, the waveguides extended to the facets of the chip will be used to couple the laser light from the input lens to the chip. The bus waveguide of interest is aligned in front of the input lens and the laser spot is focused on the facet of the waveguide. First, a 20 $\mu m$ radius microring resonator coupled with a bus waveguide is measured. The width of the waveguide and the ring resonator are both 850 $nm$, and the gap between the waveguide and the microring resonator is $g = 100\ nm$ as shown in Figure 85.

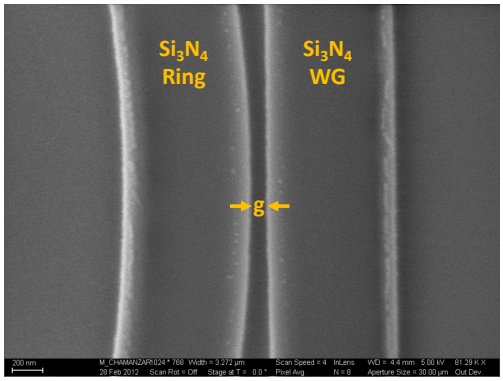


**Figure 85:** SEM showing the small gap between a straight bus waveguide and a $Si_3N_4$ microring resonator. The gap is $g \sim 100\ nm$.

The transmission spectrum of the bus waveguide coupled to this microring resonator is obtained by scanning the laser source and measuring the photodetector signal through a data acquisition (DAQ) card connected to a PC. The transmission spectrum over the tuning range of the laser, i.e., 761 $nm - 780\ nm$ is shown in Figure 86(a). The free spectral range is $FSR = 2.3\ nm$. The resonance mode at $\lambda_0 = 768.442\ nm$ is shown in Figure 86(b), where it can be seen that the intrinsic quality factor of this microresonator is $Q_0 \sim 1.7 \times 10^5$. The ripples on the transmission response correspond to the Fabry-Perot modes arising from the reflections through the sample, specially from the two facets of the chip.

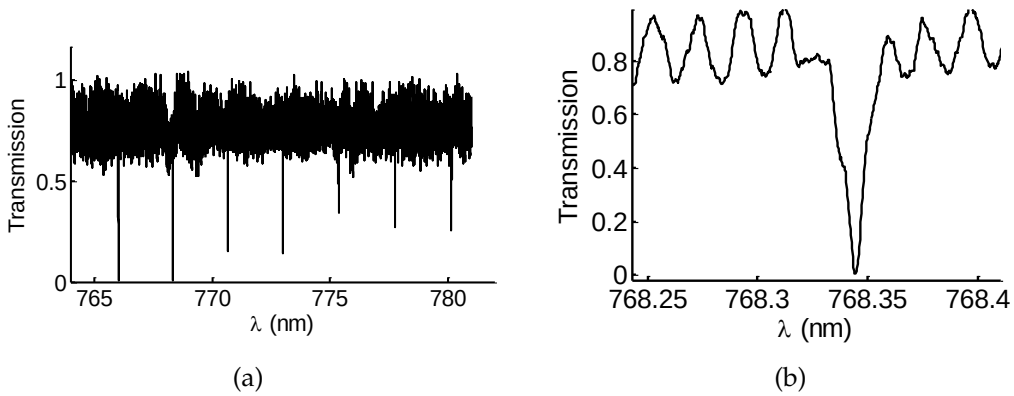


**Figure 86:** (a) The transmission spectrum of a bus waveguide coupled with a 20 $\mu m$ radius $Si_3N_4$ microring resonator. The free spectral range is $FSR = 2.3\ nm$. (b)The transmission spectrum of a bus waveguide coupled with a 20 $\mu m$ radius $Si_3N_4$ microring resonator, showing the resonance mode at $\lambda_0 = 768.442\ nm$ with $Q_0 \sim 1.7 \times 10^5$.

The top-view dark-field scattering image of the microring resonator at a resonance wavelength of $\lambda_0 = 768.442\ nm$ is shown in Figure 87. It can be seen that at the resonance, light is trapped in the microring resonator resulting in a very high field enhancement.

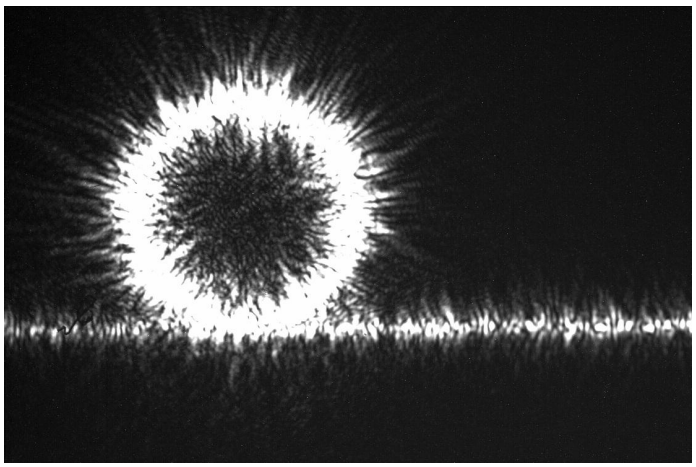

**Figure 87:** The top-view dark-field scattering image of the microring resonator at a resonance wavelength of $\lambda_0 = 768.442\ nm$.

In the next step, a hybrid resonator structure is measured on the same chip, consisting of a 20 $\mu m$ radius $Si_3N_4$ microring resonator, integrated with a 122 $\times$

$56 \times 27\ nm$ gold nanorod. The width of the microring resonator is 850 $nm$, similar to the reference microring resonator that was discussed earlier. The LSPR mode of the gold nanorod needs to be measured separately as a reference. For this purpose, a reference waveguide is designed and implemented on the same chip with the same width as the microring resonator width, integrated with a $122 \times 56 \times 27\ nm$ gold nanorod. The absorbance of this structure is measured using the method outlined in section 4.2, and the result is shown in Figure 88.

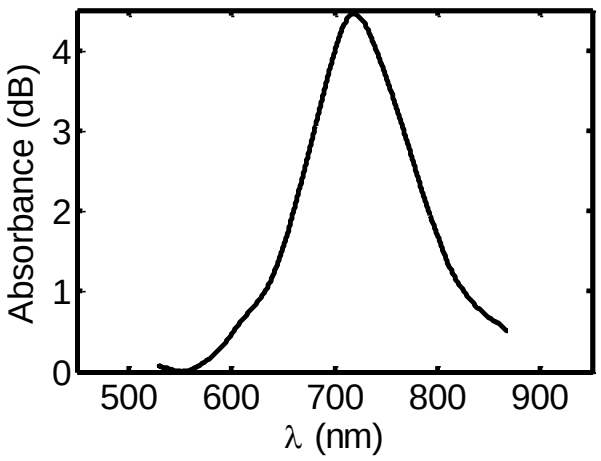


**Figure 88:** The absorbance of a hybrid waveguide structure consisting of a $200 \times 850\ nm\ Si_3N_4$ waveguide integrated with a $122 \times 56 \times 27\ nm$ gold nanorod.

It can be seen that the LSPR wavelength of this gold nanorod on the $Si_3N_4$ guided wave structure is $\lambda_0 = 717\ nm$. It should be noted that the effective index of the straight waveguide is slightly larger than the effective index of the microring resonator fundamental traveling mode. Therefore, it is expected that the LSPR mode of the gold nanorod on the microring resonator is slightly blueshifted with respect to the LSPR mode of the same gold nanorod on the waveguide. A hybrid microring resonator is then measured, in which the gap between the bus waveguide and the microring resonator is $g = 100\ nm$, similar to the case of a microring resonator without nanorod that we already discussed. The transmission spectrum is shown in Figure 89(a). The top scattering transmission

is also measured using the photodetector that is attached to the top microscope assembly (Figure 83). The result is shown in Figure 89(b).

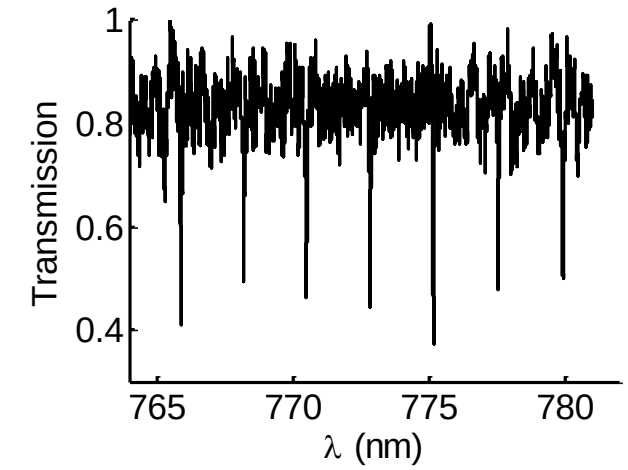


(a)

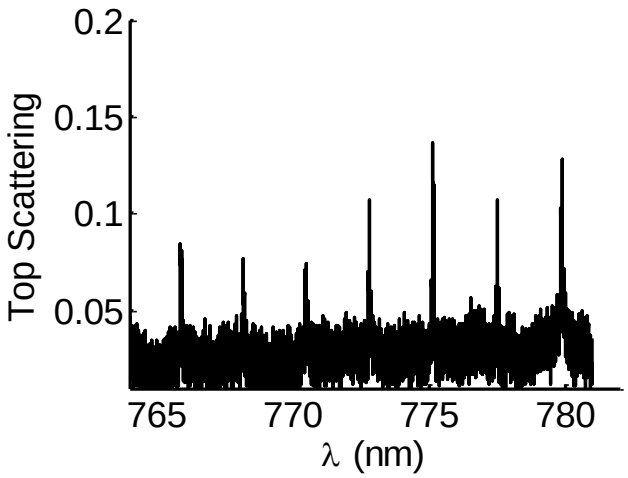


(b)

**Figure 89:** (a) The transmission spectrum of a bus waveguide coupled with a hybrid microring resonator consisting of a single gold nanorod of dimensions $122 \times 56 \times 27\ nm$. The gap between the bus waveguide and the microring resonator is $g = 100\ nm$. (b) The top scattering transmission spectrum of the structure discussed in (a).

It can be seen that the spectral location of the resonances measured from top and measured through the bus waveguide output are almost identical. It can also be seen that the free spectral range is $FSR = 2.3\ nm$, and it has not been changed

much because of the existence of the gold nanorod.

The resonance mode of this hybrid structure at $\lambda = 775.2\ nm$ measured at the waveguide output and measured from top is shown in Figure 90(a) and 90(b), respectively. It can be seen that the transmission drop is only 40%, meaning that about 60% of the power is not coupled to the hybrid resonator structure, because the coupling condition between the bus waveguide and the hybrid microresonator is not optimum.

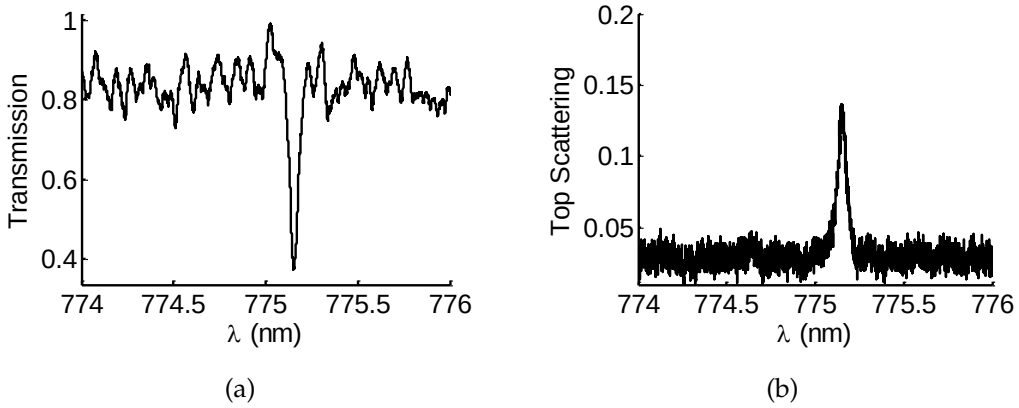


**Figure 90:** (a) The transmission spectrum of a bus waveguide coupled with a hybrid microring resonator consisting of a single gold nanorod of dimensions $122 \times 56 \times 27\ nm$, showing the resonance at $\lambda = 775.2\ nm$. The gap between the bus waveguide and the microring resonator is $g = 100\ nm$. (b) The top scattering transmission spectrum of the structure discussed in (a), showing the resonance at $\lambda = 775.2\ nm$.

The critical coupling condition to couple light to the microring resonator without nanoparticle is not valid for the hybrid resonator structure, since the intrinsic quality factor of the hybrid resonator is much less than the intrinsic quality factor of the microring resonator itself. In the next step, a hybrid microring structure is measured, in which the gap between the waveguide and the hybrid resonator structure is decreased to 50 $nm$. This way, the waveguide mode is coupled with the hybrid resonator mode more strongly. The transmission spectrum of the bus waveguide coupled with this hybrid microresonator structure is shown in Figure 91(a), where it can be seen that the extinctions of the resonance

modes are much higher, and more than 90% of the input power in the bus waveguide is coupled to the hybrid microring structure. The resonance mode at $\lambda_0 = 773.62\,nm$ is shown in Figure 91(b), where it can be seen that the total intrinsic quality factor of this hybrid microresonator is $Q_{0Hyb} \sim 3.2 \times 10^4$, which is about an order of magnitude less than the intrinsic quality factor of the same microring resonator without a plasmonic nanoparticle. The reduction in the intrinsic quality factor ($Q_0$) is mostly because of the scattering and absorption loss introduced by the nanoparticle.

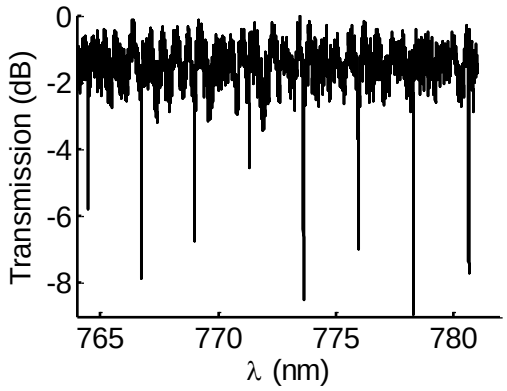


(a)

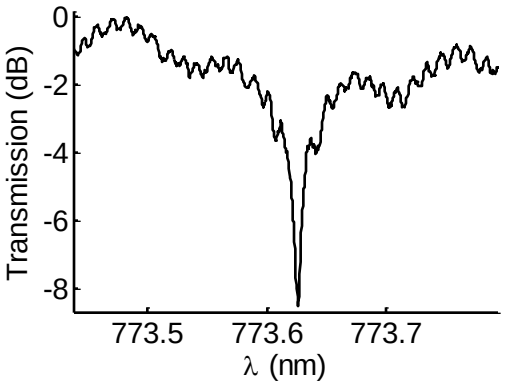


(b)

**Figure 91:** (a) The transmission spectrum of a bus waveguide coupled with a hybrid microring resonator consisting of a single gold nanorod of dimensions $122 \times 56 \times 27\,nm$. The gap between the bus waveguide and the microring resonator is $g = 50\,nm$. (b) The resonance mode at $\lambda_0 = 773.62\,nm$.

From the measurement result in Figure 91(b), the coupling quality factor

is estimated to be $Q_c = 1.4 \times 10^5$. The resulting field enhancement in this hybrid resonator structure is an additional factor of 50, in excess of the plasmonic nanoresonator field enhancement. Also, the transmission extinction indicates that more than 90% of the input power is coupled to the hybrid resonator structure. Since the $Si_3N_4$ microring resonator intrinsic quality factor was measured to be very large ($Q_0 \sim 1.7 \times 10^5$), most of the power coupled to the microring resonator is delivered to the nanoresonator LSPR mode. The brightfield and the darkfield top-view scattering images of the hybrid microresonator structure, excited at the resonance wavelength of $\lambda_0 = 773.62\ nm$ are shown in Figure 92(a) and 92(b), respectively.

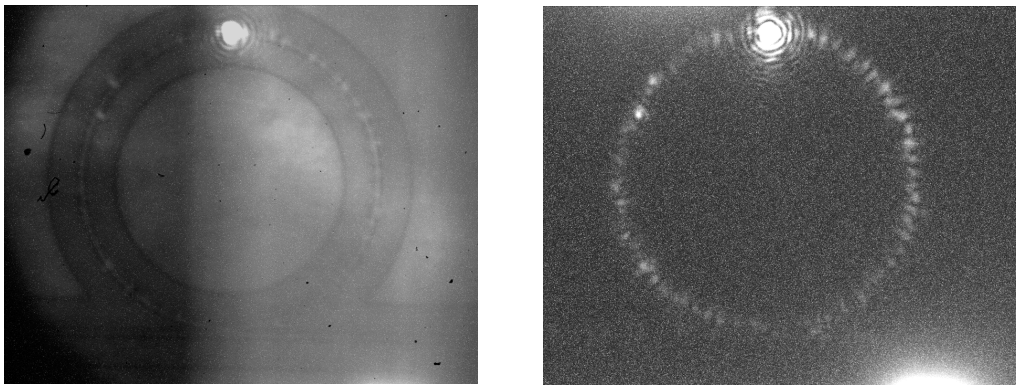

(a) (b)

**Figure 92:** (a) The brightfield and (b) the darkfield top-view scattering images of the hybrid microresonator structure, excited at the resonance wavelength of $\lambda_0 = 773.62\ nm$

It can be seen that the single nanoresonator LSPR mode is efficiently excited, and the intensity of the scattered light is much stronger than the intensity of the light circulating in the microring resonator. By using the introduced hybrid resonator structure, light can be efficiently coupled to a single plasmonic nanoresonator. This way, single nanoresonators can be studied in this platform. Also, the large coupling efficiency, the additional field enhancement, and the robustness of this hybrid structure, make it a suitable candidate for applications in

which strong light-matter interaction is desired on a chip. For example, this hybrid resonator structure can be used for on-chip Raman sensing, where the detection of a very small amount of analyte can be made possible thanks to the small footprint of the device and the large SNR that can be obtained.

# CHAPTER VI

# MICROFLUIDIC SYSTEM INTEGRATION

In this chapter, the fabrication of microfluidic systems and their integration with the hybrid plasmonic-photonic devices introduced in this thesis is discussed. The microfluidic channels are made using Polydimethylsiloxane (PDMS) and SU-8. Different methods have been optimized for sealing of the channels as well as their integration with the plasmonic-photonic devices. In this chapter, we first discuss the microfluidic systems realized in PDMS, and then we will discuss the fluidic systems based on SU-8.

## *6.1 PDMS Microfluidics*

In this section, the fabrication and integration of PDMS microfluidic systems are discussed. Polydimethylsiloxane (PDMS) is a viscoelastic organic silicone polymer. The chemical fomula of PDMS is $CH_3[Si(CH_3)_2O]_nSi(CH_3)_3$, where $n$ is the number of monomers in this polymer. PDMS is optically transparent and it is compatible with most of aqueous samples. It has widely been used to make microfluidic systems [114]. Microfluidic structures are made using PDMS molding. First, a mold is fabricated in SU-8 to cast the PDMS microfluidic structure. SU-8 is a negative epoxy-based photoresist. SU-8 is a highly viscous resist, and has been used to make very thick structures ranging from 0.5 $\mu m$ to 300 $\mu m$. To make the mold, SU-8 is spun on a 100 $mm$ silicon wafer to a thickness of 25 $\mu m$. It is then soft-baked in two steps of 65°$C$ on a hot plate for 1 $min$, and consequently 105°$C$ on another hot plate for 4 $min$. The SU-8 was patterned using photolithography. A photomask was prepared by patterning chromium on quartz with the microfluidic

patterns. The exposure is carried out using i-lile (365 $nm$ wavelength), and a dosage energy of 150 $mJ/cm^2$. Then, in the next step, the exposed SU-8 is post-baked at 105$^\circ C$ on a hot plate for 5 $min$. The exposed resist is then developed in SU-8 developer for 5 $min$, and then rinsed with DI water for 30 $sec$. The development procedure is repeated 4 times with alternate steps of immersion in SU-8 developer and DI water rinse, each for 30 $sec$. A microfluidic pattern consisting of a channel of dimensions 10 $mm \times 25\ \mu m \times 1000\ \mu m$, connected to two 1 $mm$ diameter reservoirs realized in SU-8 on a Si background is shown in Figure 93.

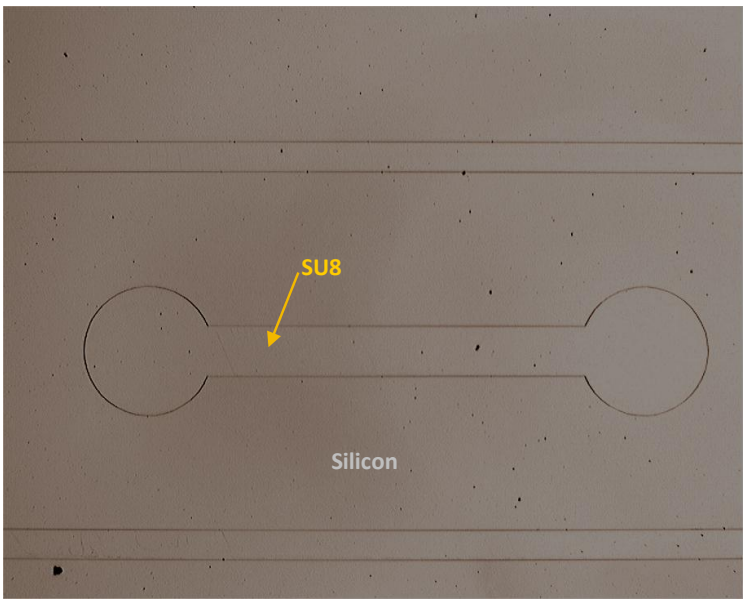


**Figure 93:** Optical micrograph showing a SU-8 mold for PDMS microfluidic channels.

The mold is now ready for casting PDMS. However, to make sure that the PDMS does not stick to the surface of Si background, an anti-stick layer must be used. We have used $OPTOOL^{TM}$ polymer from DAIKIN as the anti-stick layer. It is a fluorine polymer that has strong fouling prevention performance. First, OPTOOL is dissolved in perfluorohexane solvent with a ratio of (1:1000). Then the wafer is dipped in the solution for 1 minute. Since the solution is highly volatile, it is necessary to cover the container. Then, the wafer is thoroughly

rinsed with perfluorohexane and then it was dried using $N_2$. A monolayer of OPTOOL is formed on the mold providing a non-sticking surface. The non-sticking property of the surface is tested by observing the surface hydrophobicity. If the OPTOOL covers the entire surface completely, a very strong non-wettable surface is obtained.

After the mold becomes ready, the PDMS is prepared by mixing the oligomer and the curing agent with a ratio of (10:1). The mold is placed in a 4 inch plastic box, and the mixture is poured on the SU-8 mold. The PDMS is degassed in a desiccator for 12 hours and cured on a hot plate at a temperature of $70°C$ for 5 hours. Once the PDMS is cured, the fluidic channels are formed in PDMS as is shown in Figure 94. The whole PDMS layer is then peeled off, and the channels are cut from the PDMS layer using a rasor blade, and the reservoirs are punched to insert the tubes.

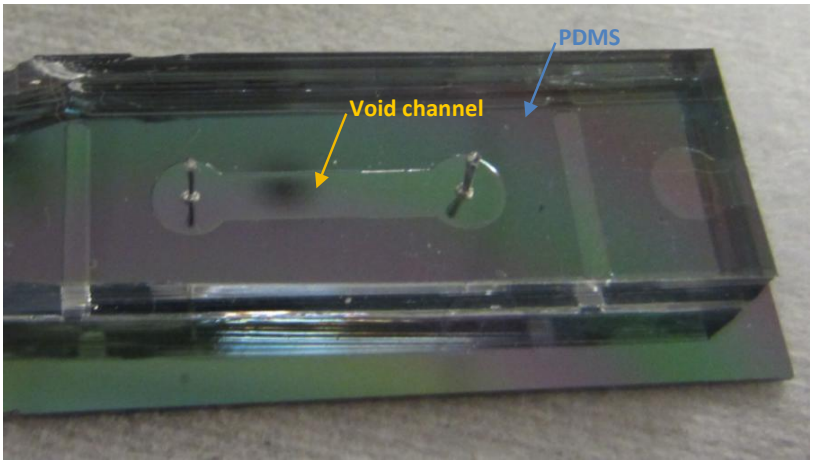


**Figure 94:** Image of a PDMS channel with reservoirs and holes for port insertion.

The next step is to align, and bond the PDMS to the surface of the chip. The bonding of PDMS to the surface of $Si_3N_4$ is carried out through covalent bonding. It is believed that if the surface of PDMS is exposed to oxygen plasma,

silanol ($-OH$) groups are formed on the surface of the PDMS and replace the methyl ($CH_3$) groups [115]. When the surface of $Si_3N_4$ is also exposed to oxygen plasma, hydroxyl groups will form on the surface. When the two surfaces containing silanol groups are brought into physical contact, they react to form $Si-O-Si$ bonds and release water molecules. This bond is very strong and almost irreversible. Therefore, the channels and reservoirs are strongly sealed. Although the above procedure seems very straight forward, functionalization of the PDMS surface requires the appropriate oxygen plasma parameters and is a very sensitive procedure. If the oxygen plasma is very weak, the density of formed hydroxyl groups will be low, and the bonding surface area will be small, resulting in leakage from the channels. On the other hand, if the oxygen plasma is too strong, the polymer chain can be damaged, again resulting in poor bonding. Since the silanol groups are polar in nature, they make the surface hydrophilic. Therefore, the level of the surface hydrophilicity can be used as a measure of the density of silanol groups on the surface. To optimize the oxygen plasma parameters, different PDMS pieces are prepared and each one is treated with oxygen plasma with specific parameters on an Oxford RIE tool. Then the contact angle of a drop of water is measured. The parameters are optimized until a very small contact angle is obtained. In Figure 95, the results of contact angle measurements for three different parameters of oxygen plasma is illustrated. It can be seen that for an untreated PDMS, the contact angle is large ($\theta = 65^\circ$), meaning that the surface is not hydrophilic. For an oxygen plasma with power of $P = 60\ W$ and pressure of $Press. = 100\ mTorr$, run for 30 $Sec$, the contact angle is reduced to ($\theta = 14^\circ$), and there is not enough density of hydroxyl groups on the surface. However, it can be judged from Figure 95(b), that the density of hydroxyl groups on the surface is still low. Many different combinations of the oxygen plasma was tried. It is concluded that a high power and a low pressure can be detrimental to PDMS

surface quality. Also, it was found that a prolonged exposure of PDMS to oxygen plasma can etch the surface of PDMS, degrading the surface quality for bonding. After searching over different plasma parameters, the optimum conditions were found to be $P = 60\ W$, $Press. = 30\ mTorr$, and $t = 12\ Sec$. The contact angle measurements for a PDMS sample treated with oxygen plasma with the aforementioned parameters is shown in Figure 95(c), where it can be seen that the surface is highly hydrophilic.

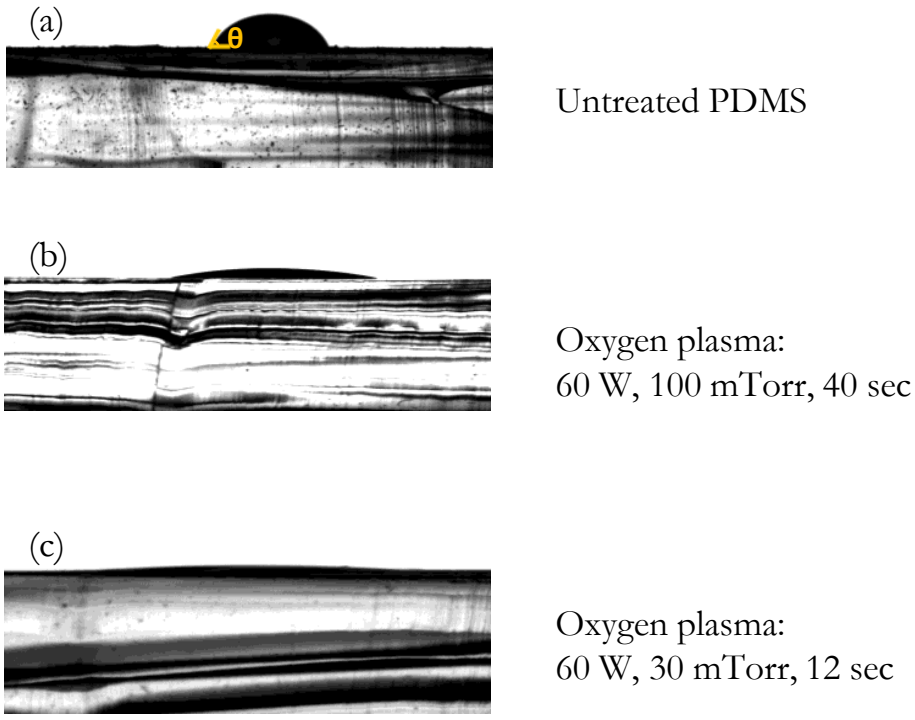


**Figure 95:** Contact angle measurements on oxygen plasma treated PDMS surfaces. (a) The untreated PDMS surface. (b) Oxygen plasma parameters: $P = 60\ W$, $Press. = 100\ mTorr$, and $t = 40\ Sec$. (c) $P = 60\ W$, $Press. = 30\ mTorr$, and $t = 12\ Sec$.

It should be noted that the hydrophilicity of the surface is degraded over time, and to achieve a strong bond, the two surfaces of PDMS and $Si_3N_4$ must be brought into immediate contact after the oxygen plasma treatment.

The PDMS microfluidic channel treated with oxygen plasma is then aligned

with the hybrid waveguides and resonators, and then bonding is carried out under a stereo microscope. The microfluic channel dimensions used in this work are 500 $\mu m \times 25\ \mu m \times 1000\ mm$. The reservoirs are circular with diameters are 1 $mm$. A PDMS microfluidic system integrated with a set of hybrid waveguides and resonators is shown in Figure 96.

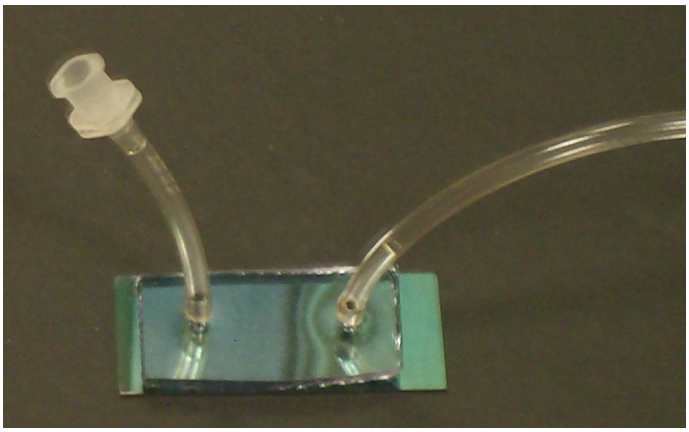

**Figure 96:** Image of a PDMS channel bonded to a $Si_3N_4$ substrate. Two holes are punched into the reservoirs for the insertion of inlet and outlet ports.

Two holes are punched into the reservoirs, and tubes are connected through appropriate ports as can be seen from Figure 96. In most of the measurements carried out in this thesis, the flow of the analyte inside the channel is controlled using a syringe pump, with flow rates in the range of $100 - 400 \mu L/min$. It should be noted that the channels can easily withstand much larger flow rates. However, the speed of the liquid flow inside the channel becomes very large that can damage the optical structures.

## *6.2 SU-8 Microfluidics*

It was discussed in section 6.1 that SU-8 is a negative photoresist that can be used to make a mold for PDMS casting. In this section, we discuss using of SU-8 to realize the microfluidic structures. Although PDMS is a viable option for

making microfluidic channels, it is not compatible with some organic solvents, limiting its use mostly to aqueous analytes. For example, we have tested the compatibility of PDMS with different solvents, and it turned out that ethanol, acetone, and chloroform can attack the PDMS surface, whereas isopropanol (IPA) and tetrahydrofuran (THF) are safe to use. On the other hand, SU-8, when cured, is compatible with most of the organic solvents and chemicals. Therefore, the microfluidic channels realized in SU-8 can be used in sensing applications where such analytes are used.

After the hybrid plasmonic-photonic devices are fabricated, SU-8 is spun on the surface of the chip. The thickness of the SU-8 layer can be controlled in the range of 0.5 $\mu m$ to 30 $\mu m$ by controlling the viscosity and the spinning speed of the SU-8. For example, here the procedure to make 5 $\mu m$-heigh SU-8 channels is discussed. First, SU-8 2005 from Michrochem is dispensed on the surface, and is spun with a speed of 3000 $RPM$ for 34 $sec$ to a thickness of 5 $\mu m$. It is then soft-baked at 105$^{\circ}C$ for 2 $min$. A chromium photomask that was ordered from Photosciences is then used in a Karl Suss MA-6 Mask Aligner photolithography system to expose the SU-8 layer with a dosage of 160 $mJ/cm^2$. The alignment between the hybrid plasmonic-photonic devices and the microfluidic channel patterns is carried out by using two gold cross markers fabricated on the surface of the chip. In the next step, the sample is post-baked on a hot plate at 105$^{\circ}C$ for 3 $min$. Then, the patterns are developed in SU-8 developer for 1 $min$, followed by rinsing the sample with DI water. Then the sample is again immersed in the SU-8 developer for 10 $sec$ and is then rinsed with DI water. This step is repeated until a clear pattern is obtained. It should be noted that there is a trade-off between the adhesion of SU-8 to the $Si_3N_4$ surface, and the clear developing of the patterns. Increasing the temperature and time for the soft-bake step, improves the adhesion of SU-8 to the surface of $Si_3N_4$. However, it results in the partial cross-linking of SU-8, making

the developing of the patterns rather difficult. Figure 97 schematically show the procedure to expose SU-8 channels. It can be seen that the orientation of the SU-8 channels is perpendicular to the lightwave propagation direction in the hybrid waveguide.

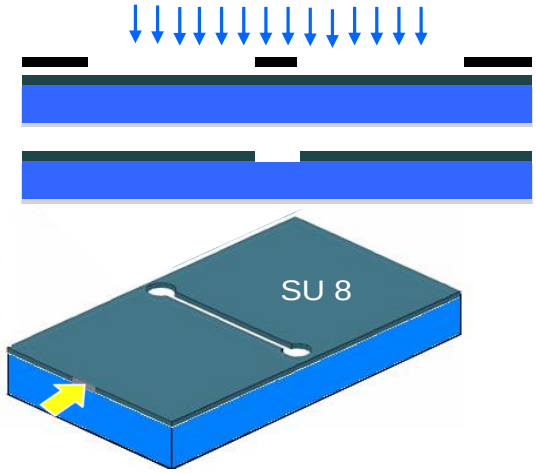


**Figure 97:** Schematic illustration of microfluidic channel fabrication in SU-8.

The optical micrograph of a SU-8 channel integrated with an array of hybrid plasmonic-photonic waveguides is shown in Figure 98, where it can be seen that the microfluidic channel is precisely aligned with the array of waveguides. The small triangular marker indicates the location of the plasmonic gold nanoresonators on the waveguides. The micrograph of the reservoir is also shown in this figure.

In the next step, the microfluidic channels realized in SU-8 need to be capped and sealed. Also, the appropriate connections to the external tubings need to be carried out. Here, two methods for capping of SU-8 channels is developed, and optimized. In the first method, a PDMS cap is used with two holes punched in PDMS and aligned with the SU-8 reservoirs for inlet and outlet connections. It is known that free epoxide groups on the surface of the SU-8 can react with amine groups [116] to form covalent bonds. It has been shown that the surface of PDMS

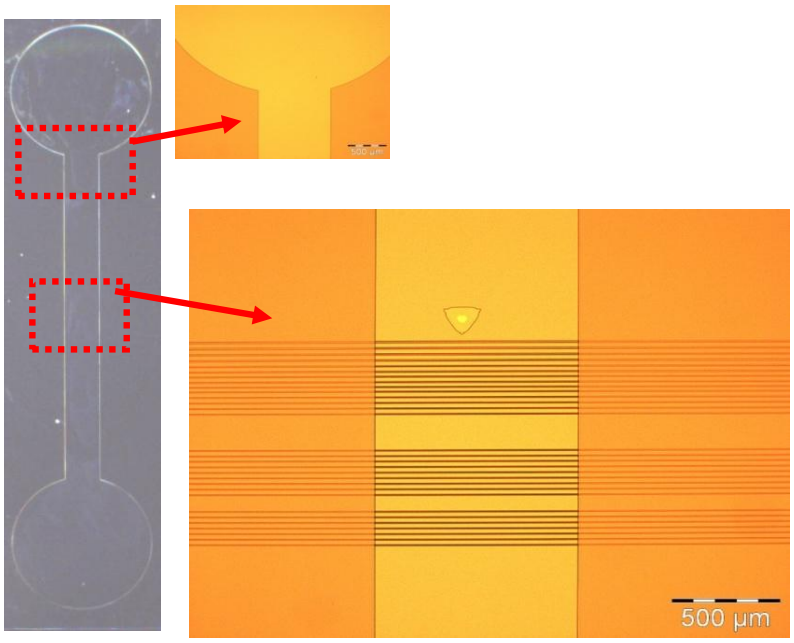


**Figure 98:** The optical micrograph of a SU-8 microfluidic channel integrated with an array of hybrid plasmonic-photonic waveguides.

can be functionalized with amine groups if it is exposed to nitrogen plasma [116], or treated with 3-aminopropyltrimethoxysilane [117]. Here, the surface of the PDMS is first functionalized with hydroxyl groups through an oxygen plasma with the optimized parameters that were discussed in section 99. Then it is immersed in a solution of 5 % (3-Aminopropyl)triethoxysilane (APTES) for 2 hours. The excess APTES is then washed off the surface. This way amine groups will form on the surface of PDMS through silanization.

Then the PDMS cap is brought into close contact with the SU-8 channels, and by applying pressure on a hot plate at 100 $^{\circ}C$ for 20 *min* the bonding is carried out. In this method amine groups on PDMS and epoxide groups on the SU-8 surface react and form covalent bonds. It is found that this method is very sensitive to the surface density of epoxide groups on the SU-8 surface. Since SU-8 is cured, the density of epoxide groups is not high resulting in weak bonding. For the microfluidic channels fabricated using this method, a leakage is usually possible

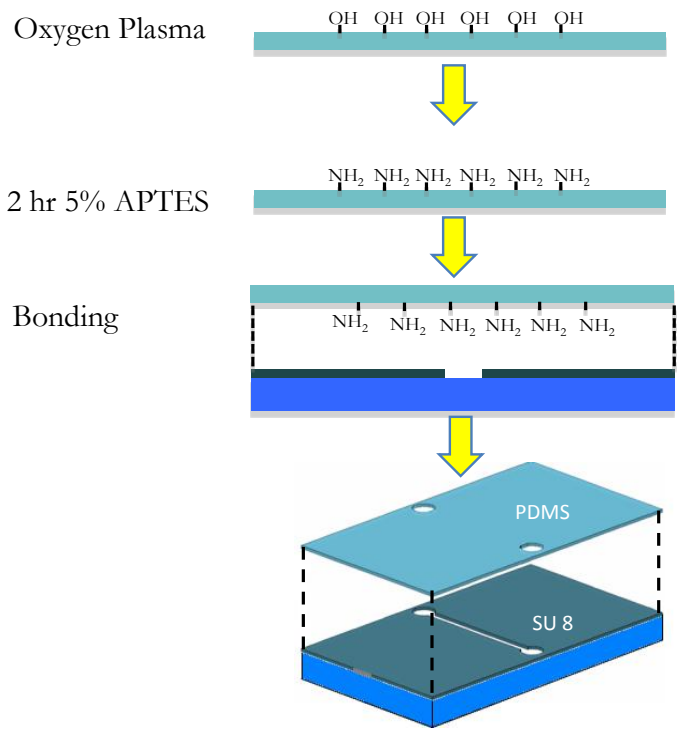


**Figure 99:** The optical micrograph of a SU-8 microfluidic channel integrated with an array of hybrid plasmonic-photonic waveguides.

when the flow rates are increased. It should be noted that the channels capped with PDMS using this method, are not very suitable for high resolution imaging as the PDMS cap, although being transparent, is a little diffusive, thus bluring the image. To overcome these issues and to make a complete chemically compatible channel, another method was tried based on capping the SU-8 channels with quartz. This way an optically clear and mechanically solid cap is used. It was found that the glass surface and the SU-8 cannot be directly bonded even under high temperature and heat. Therefore, the bottom surface of the quartz cap was coated with a thin layer of SU-8. Then the two layers of SU-8 were fused to each other by applying heat and pressure. SU-8 2002 from Microchem is spun on the bottom surface of the quartz cap to a thickness of 2 $\mu m$. Then the two surfaces are brought into close contact. The two parts are aligned with each other, and then they are put into a Karl Suss SB6 substrate bonder tool. In this tool, the bonding can be carried out in

vacuum and under controlled pressure and heat conditions. A recipe is optimized on this tool to obtain a permanent bond and a good seal. It should be noted that, by increasing the temperature, force, and time the bond strength can be increased. However, if the temperature is increased too much, the SU-8 will flow and the channel can be clogged or deformed. Also, if the tool force is increased beyond a certain point, the substrate or the cap will break. Different parameters were tried and the optimum recipe is obtained as follows. The chamber is first pumped down to a pressure of $10^{-5} Torr$. The temperature of the substrate and the cap are then increased to $150^{\circ} C$. In the next step, a tool pressure of $1.1 MPa$ is applied for $1 hour$. Then gradually the tool pressure is decreased to 0 over 30 $min$. The temperature is then decreased to $50^{\circ} C$. The image of a microfluidic channel, with a quartz cap is shown in Figure 100(a). To make ports for the inlet and outlet tubes, through holes are drilled into the substrate in the reservoirs. The inlet and outlet tubes are connected from the back of the substrate, by using the nanoports from IDEX as shown in Figure 100(b).

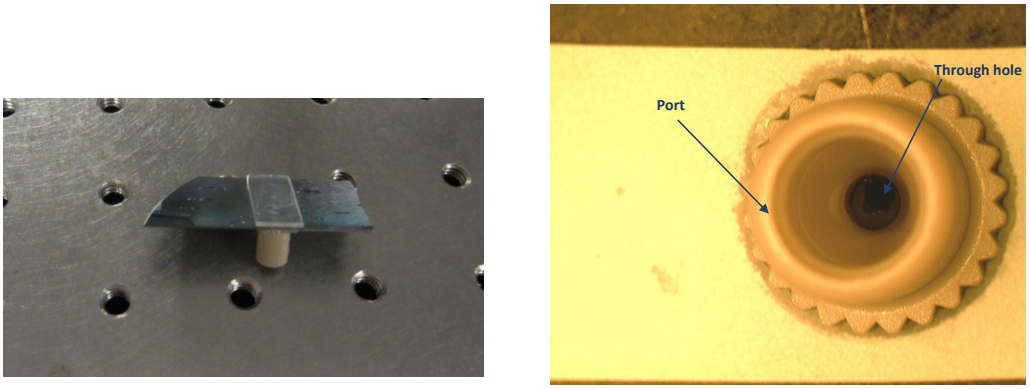


(a) (b)

**Figure 100:** (a) Image of a SU-8 microfluidic channel capped with quartz. (b)Image of the backside of the sample, showing the inlet and outlet ports installed from the backside. The analyte is delivered to the channel through the holes under the ports.

To test the quality of such microfluidic channels, DI water is pumped through these channels at different flow rates using a syringe pump. In Figure 101, an

optical micrograph showing the flow of water in the channel is shown, where a very good seal prevents leakage from the channel.

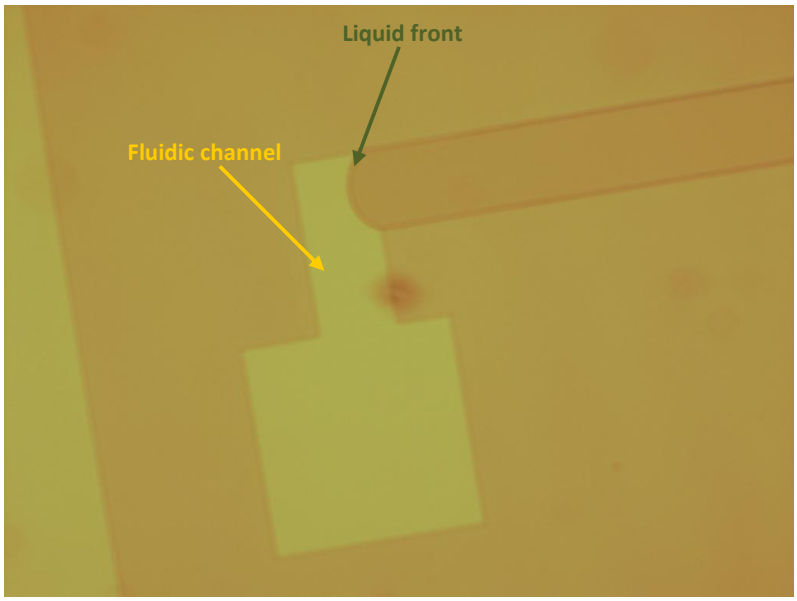


**Figure 101:** The flow of DI water in a SU-8 microfluidic channel capped with a quartz lid.

The different methods for making microfluidic channels and reservoirs discussed in this chapter can be used to integrate microfluidics with on-chip hybrid plasmonic-photonic structures to test different sensing scenarios.

# CHAPTER VII

# FUTURE DIRECTIONS

The integration of plasmonic structures with on-chip photonic structures opens up new potentials for applications in which strong light-matter interaction is necessary. It was shown that by integrating plasmonic nanoresonators with waveguides and microresonators, light can be efficiently coupled to the LSPR modes, resulting in strong light-matter interaction. It was also shown that by integrating plasmonic waveguides and microresonators with photonic waveguides and microresonators, surface plasmon polaritons can be efficiently excited in a hybrid platform. In this thesis, the application of such hybrid plasmonic-photonic structures for on-chip sensing and spectroscopy is discussed. The foreseeable future directions after this research are developing novel hybrid plasmonic-photonic device concepts and new applications. The proposed hybrid devices can be optimized for on-chip nanofocusing of light, on-chip trapping, and on-chip signal processing and communications. The developed hybrid platform provides a means of bringing plasmonics on a functional platform, where light propagation and localization is mainly carried out using low-loss and high-Q photonic guided wave structures, and strong light-matter interaction is carried out using plasmonic structures.

## *7.1 On-chip Nanofocusing and Trapping*

It has been shown that plasmonic tapered structures can localize and concentrate light in very small scales, much less than the wavelength of light [118]. It was shown in section 3.2 that propagating surface plasmon polaritons (SPPs) can be coupled with photonic guided modes. It was shown that when the phase

velocities of the separate SPP and photonic guided modes are the same, they can couple with each other and result in two hybrid modes that have different phase velocities and different field distributions as a result of the splitting of the modes. If there is a buffer layer between the plasmonic and the photonic structure, then the corresponding modes can be weakly coupled with each other, and the input light energy is gradually coupled to the propagating SPP and then coupled back to the photonic guided mode as a result of the mode beating. If the plasmonic waveguide is appropriately tapered, then the light coupled to the SPP mode is completely concentrated at the taper tip. We have designed and implemented hybrid waveguide structures, in which the light propagating in the core of a Silicon or $Si_3N_4$ waveguide is coupled and transferred to a propagating SPP, which is then focused to a very tight spot [119]. The schematic of the device is shown in Figure 102. The field amplitude profile is shown in the inset of Figure 102, where it can be seen that light is concentrated to the apex of the triangle tip.

The input polarization state is TM, with the principal component of the transverse electric field in the $y$ direction. The very intense light at the apex of the triangle taper, and its large gradient results in a very large localized force exerted on any particle in the nearfield of the plasmonic structure. This phenomenon can be combined with a sensing technique to first capture and trap small molecules, and then detect them. Such a combined trap and detect sensing mechanism can be particularly found to be useful in sensing scenarios involving the detection of low-concentration analytes.

## *7.2 Demonstration of Multiplex Multi-analyte Sensing using the Hybrid Integrated Devices and Plasmonic Micro-arrays*

It was shown that hybrid plasmonic-photonic structures provide a robust platform for efficient light-matter interaction. The LSPR sensing to detect different analytes

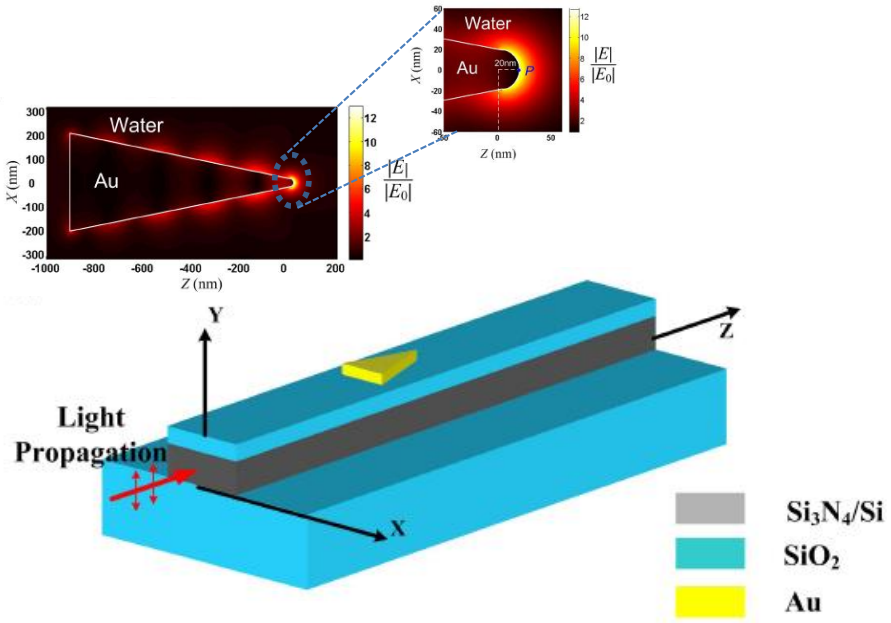


**Figure 102:** Schematic of a hybrid plasmonic-photonic structure for on-chip nanofocusing of light. The inset shows the field amplitude profile of the plasmonic mode, concentrated at the apex of the metal taper.

with large sensitivities were demonstrated in this research. The potential of the hybrid resonator-based devices for on-chip SERS was also demonstrated. Although the discussions and the sensing demonstrations were limited to the detection of only one type of analyte at a time, the same sensing scenario can be extended for the detection of multiple analytes in parallel. Also, the response of an array of sensors can be encoded in spectral domain, so that they can be interrogated simultaneously for a high-throughput sensing scenario. For example, as shown in Figure 103(a), the input power can be divided into multiple parallel hybrid waveguides, each of them functionalized with a specific surface coating to detect a specific target analyte. Also, an array of hybrid resonator structures can be used in series all coupled with a common bus waveguide (Figure 103(b)). These hybrid resonators can be designed so that they have different resonance wavelengths and free spectral ranges (FSRs). This way, they can be used for the

detection of multiple target analytes, simultaneously.

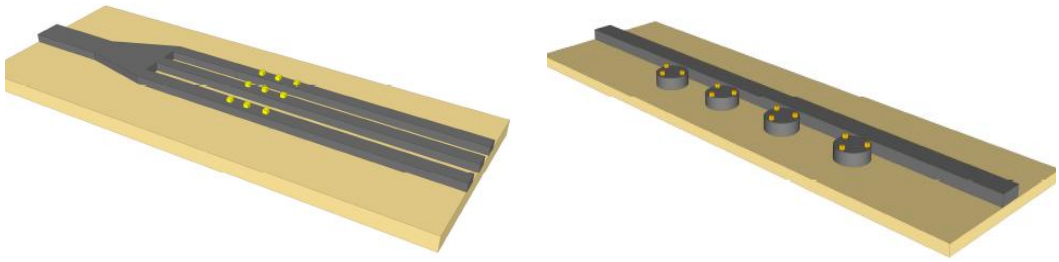

(a) (b)

**Figure 103:** Schematic of (a) parallel hybrid waveguides and (b) series hybrid resonators for multiplex multi-analyte sensing.

It was also demonstrated that plasmonic nanoparticle arrays can be used for high-throughput, efficient LSPR sensing and SERS. In this thesis, LSPR detection of Cholera toxin using GM1 glycan receptors, and also SERS detection of thiophenol were demonstrated. The same idea can be extended to the detection of multiple analytes by functionalizing different plasmonic nanoresonator arrays on the same substrate in the form of a microarray with different receptors to specifically detect different analytes. The developed free-space microabsorption microscope setup, discussed in chapter 2, can then be used to detect multiple analytes in parallel.

## *7.3 Design of Hybrid Plasmonic-photonic Double Resonator Structures using Photonic Standing-wave Resonators*

The hybrid photonic-plasmonic double resonator structures introduced in section 5.1 are designed based on photonic travelling wave resonators such as microrings and microdisks. It was shown that the high quality factor of the photonic travelling wave microresonators can enhance the coupling of lightwave to localized surface plasmon resonance (LSPR) modes of microresonators, and therefore can leverage the field enhancement. The natural extension of this line of research will be

investigating standing-wave microresonators such as Fabry-Perot and nanobeam photonic crystal microresonators. The principle of operation of these resonators is based on the formation of standing waves between two mirrors. It has been shown that photonic crystal resonators can provide ultrasmall mode volumes [98]. However, their quality factors are usually smaller than those of travelling wave microresonators. It has been shown that by nanoassembling of plasmonic nanoresonators on two-dimensional photonic crystal cavities, enhanced light-matter interaction properties can be achieved [65]. The schematics of a Fabry-Perot-based and a nanobeam-based hybrid resonator are shown in Figure 104(a) and Figure 104(b), respectively. The nanobeam photonic crystal cavity can be designed so that the one-dimensional photonic crystal on each side of the plasmonic nanoresonator exhibits a bandgap throughout the resonance of the plasmonic nanoresonator.

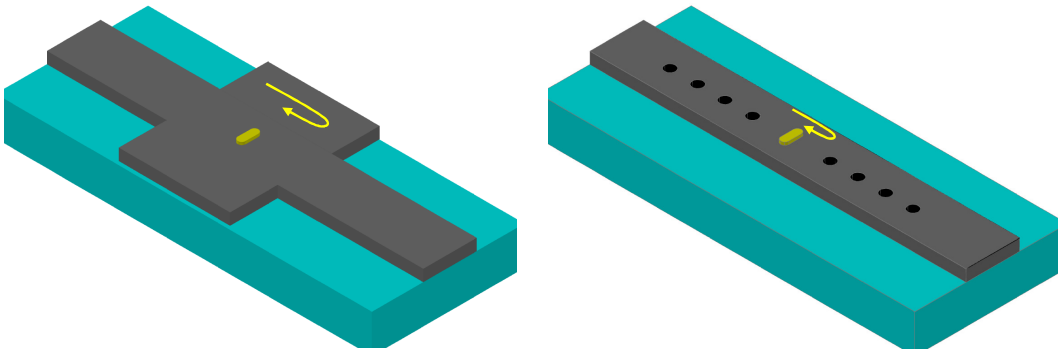

(a) (b)

**Figure 104:** Schematic of hybrid resonators consisting of plasmonic nanoresonators integrated with (a) a Fabry-Perot standing wave microresonator, and (b) a nanobeam photonic crystal microresonator.

Also, the plasmonic nanoresonator arrays can be combined with vertical Fabry-Perot standing wave resonators so that the light trapped in the resonance modes of such resonators can interact more efficiently with the plasmonic nanoresonator array in multiple passes. The concept of such a novel hybrid plasmonic-photonic

resonator structure is illustrated in Figure 105.

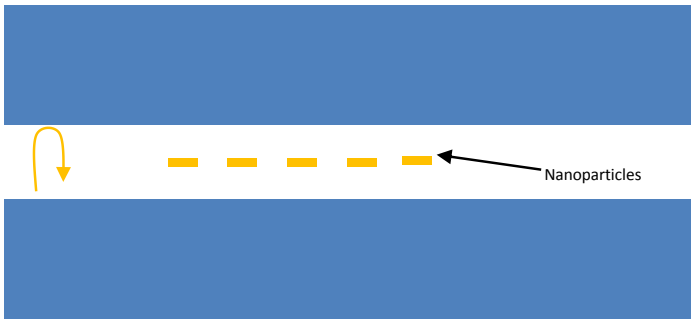


**Figure 105:** Schematic of a hybrid plasmonic-photonic structure consisting of a vertical Fabry-Perot and an array of plasmonic nanoparticles.

It can be shown that if this structure is carefully designed, then LSPR modes can be coupled with Fabry-Perot modes resulting in efficient coupling to plasmonic modes and large field enhancements.

# CHAPTER VIII

# CONCLUSION

The main focus of this research has been on the design, fabrication, and demonstration of hybrid plasmonic-photonic structures for biochemical sensing applications. In the first step, semi-analytical models have been developed and appropriate simulation tools are employed to design and analyze plasmonic nanostructures, integrated photonic structures, and hybrid photonic-plasmonic devices. Finite element method (FEM) is employed for obtaining photonic and plasmonic modes, and finite difference time domain (FDTD) is used for the analysis of lightwave propagation in the hybrid structures. I have shown that by integrating plasmonic nanoresonators with photonic microresonators, ultra-high field enhancements and very large coupling efficiencies can be achieved. It has also been shown that by integrating plasmonic nanoresonators with on-chip waveguides, individual plasmonic nanoresonators can be interrogated over their entire resonance bandwidth. It is also shown that coupling of surface plasmon polaritons and guided wave photonic modes can result in hybrid plasmonic-photonic modes that have high sensitivities of plasmonic modes as well as the high quality factors achieved from photonic modes.

The next course of action has been to develop appropriate fabrication processes to realize the hybrid photonic-plasmonic structures. A two-step electron beam lithography (EBL) is used to define the plasmonic layer and the photonic layer patterns, where precise alignment between the two steps of lithography has been achieved. The metal evaporation, lift-off, and etching processes have been optimized for the efficient realization of hybrid plasmonic-photonic structures.

Novel hollow-core nanoparticles such as gold nanocages (AuNCs) fabricated using chemical synthesis methods are also used in this research. To experimentally test the performance of the developed hybrid structures, three optical characterization setups have been designed and implemented. The first is an in-plane characterization setup that is equipped with a broadband supercontinuum source and a spectrometer as the detector. This optical setup has been used to characterize waveguide-based hybrid structures , where it was shown that a few number of plasmonic nanoresonators integrated with photonic waveguides can be interrogated with a very large signal-to-noise ratio (SNR) exceeding 24 $dB$ over a wide bandwidth covering the entire LSPR spectrum. The second optical setup is an in-plane characterization setup that has a tunable laser source and a photodetector synchronized with each other. It has been used to characterize hybrid resonator-based structures, where very narrow resonance features need to be measured. We have shown that interrogation of single plasmonic nanoparticles is possible in this platform with very large efficiency, without the need to use ultra-sensitive cooled detectors or long integration times. The third optical characterization setup is a microabsorption characterization setup with polarization control to characterize the extinction properties of different designed plasmonic nanoparticle arrays. This characterization setup was also used to carry out LSPR sensing. In the next step, microfluidic channels has been implemented in PDMS and SU-8 to be integrated with the plasmonic and photonic structures to deliver the analyte of interest efficiently.

The application of the introduced devices for on-chip sensing has been demonstrated by measuring the LSPR shift of the hybrid plasmonic-photonic waveguide structures for different concentrations of dextrose, where a large sensitivity of $\sim 250\ nm/RIU$ is achieved. The Raman emission spectrum of a Benzene-based chemical has also been measured using the different nanoplasmonic structures

introduced in this thesis.

The plasmonic and photonic structures developed in this research can provide advanced on-chip functionalities and can be used in different applications such as point-of-care diagnostics, therapeutics, chemical sensing, on-chip optical trapping, and even optical interconnects and signal processing.

A brief summary of the main contributions of this research:

- I developed semi-analytic models and simulation methods to analyze and design hybrid plasmonic-photonic structures, including a hybrid waveguide structure consisting of a plasmonic nanoresonator and a photonic waveguide, a hybrid waveguide structure consisting of a plasmonic and a photonic waveguide, a hybrid resonator structure consisting of a plasmonic nanoresonator and a photonic microresonator, and a hybrid waveguide structure consisting of a plasmonic and a photonic microresonator.

- I designed plasmonic nanoresonator arrays for different wavelength ranges and with different sensitivities.

- I developed nanofabrication processes to realize plasmonic and photonic structures. These fabrication processes include electron beam lithography, material deposition and etching, and lift-off processes.

- I characterized the fabricated structures using common metrology tools such as SEM, AFM, EDX, XPS, microscopes, and profilers.

- I designed and implemented three optical setups to characterize the implemented devices. Two of the optical setups are in-plane setups working with supercontinuum broadband lasers, tunable lasers, photodetectors and spectrometers. This optical setup is a free-space absorption microscope, equipped with a spectrometer.

- I experimentally demonstrated the interrogation of single plasmonic nanoparticles with large coupling efficiencies in a robust alignment-insenstive platform, and with a very large signal-to-noise ratio (SNR).
- I experimentally demonstrated the integration of hybrid plasmonic and photonic structures with microfluidic systems for efficient delivery of analytes of interest to the sensing sites.
- I experimentally demonstrated the application of the plasmonic and photonic structures for on-chip sensing and spectroscopy.

# APPENDIX A

# POST PROCESSING OF THE MEASURED DATA

The post processing and analysis of the experimental data is very critical to extract meaningful results. In each measurement, there are different sources of noise such as the signal and background shot noise, detector dark noise, and flicker noise. All these noise sources result in random variations of the detected signal. To reduce the effect of noise, the signal of interest is measured many times and the average of all the measurements is used. Also, by smoothing the measured signals, rapid variations due to noise are removed. It was seen in chapter 4 that to characterize the hybrid waveguide structures, the chip is cleaved and the light is coupled through an input lens to the input facet of the chip and the output is collected through an output lens. The change of the medium from air to the chip and from the chip to the air results in reflections and a Fabry-Perot resonator is formed between the two facets of the chip. Any other reflections in the system, for example, the reflection from the lens surface, can also result in the formation of a Fabry-Perot. The resonance wavelength of each mode of a Fabry-Perot in a simplified case, where there is no phase shift at the interfaces can be obtained as

$$\lambda_0 = \frac{2Ln_{eff}}{m}, \tag{28}$$

where $m$ is the longitudinal mode number, and $n_{eff}$ is the effective index of the propagating mode in the medium. The length of the formed Fabry-Perot cavity is $L$. Fabry-Perot modes are spaced with a free-spectral range (FSR) of

$$\Delta\lambda = \frac{{\lambda_0}^2}{2Ln_{eff}}, \tag{29}$$

Fabry-Perot fringes can modulate the output desired signal and can result in ambiguities in the interpretation of data. Since Fabry-Perot modes are spaced in an almost periodic way, they will be localized in the Fourier domain. Therefore, to remove the Fabry-Perot effect without distorting the main useful data in the measured signal, the signal can be low-pass filtered with an appropriate Gaussian filter. To design the appropriate Gaussian filter, the Fourier transform of the measured spectrum is obtained. It should be noted that with the Fourier transform, the signal is transformed from the wavelength domain to a spectral domain that represents the spectral components of the wavelength domain signal.

The raw measured extinction spectrum for a hybrid waveguide structure consisting of a 900 $nm \times 200$ $nm$ $Si_3N_4$ waveguide integrated with an array of plasmonic gold nanorods of dimensions $96 \times 57 \times 27$ $nm$ is plotted in Figure 106. The offset of baseline from 0 $dB$ is because of the large variation of the baseline, due to noise and other unwanted effects such as Fabry-Perot.

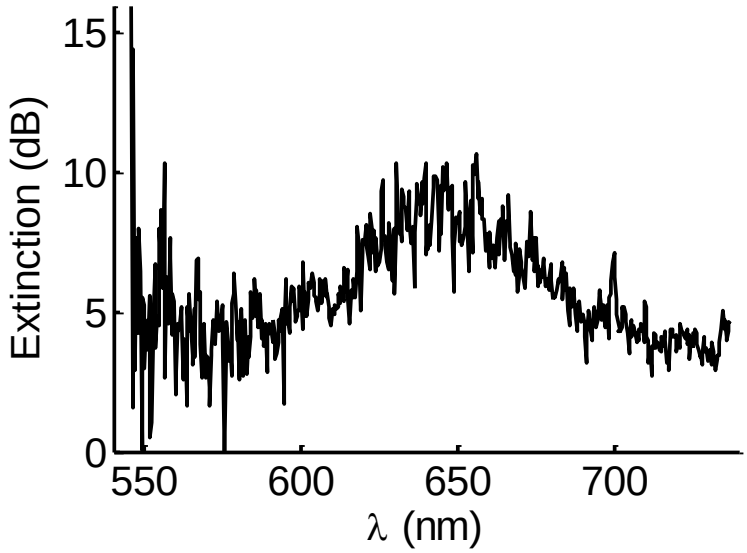


**Figure 106:** The raw measured extinction spectrum for a hybrid waveguide structure consisting of a 900 $nm \times 200$ $nm$ $Si_3N_4$ waveguide integrated with an array of plasmonic gold nanorods of dimensions $96 \times 57 \times 27$ $nm$.

Noise and the Fabry-Perot resonances have modulated the extinction. To

remove the Fabry-Perot features, the Fourier transform of the signal is obtained as shown in Figure 107. The Gaussian filter response is also shown on the same figure.

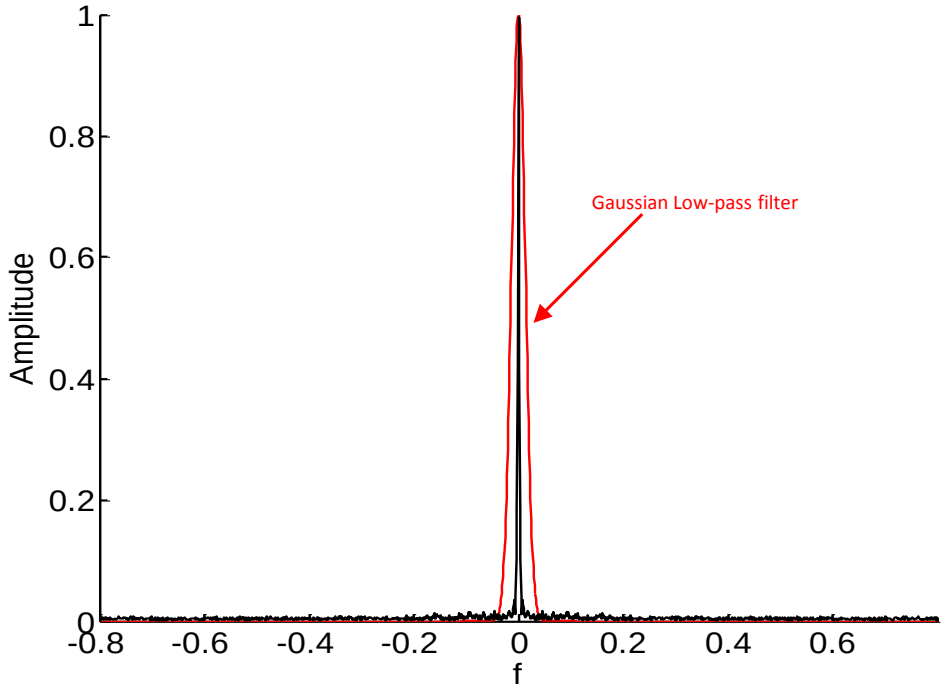


**Figure 107:** The Fourier transform of the measured extinction spectrum for a hybrid waveguide structure consisting of a 900 $nm \times 200$ $nm$ $Si_3N_4$ waveguide integrated with an array of plasmonic gold nanorods of dimensions $96 \times 57 \times 27$ $nm$. The Gaussian low-pass filter is also shown on this figure. The unwanted spectral features can be filtered out.

The frequency ($f$) in Figure 107 represents the inverse of the sampling wavelength. It should be noted that the extinction of the plasmonic nanoresonator is a low-frequency spectral feature, whereas the noise and the Fabry-Perot resonances are high-frequency features. Therefore, they can be separated from each other in the spectral domain. The low-pass Gaussian filter retains the low-frequency features and removes the high-frequency variations from the signal. The filtered extinction spectrum is shown in Figure 108.

It should be noted that for each measured signal, an appropriate filter must be

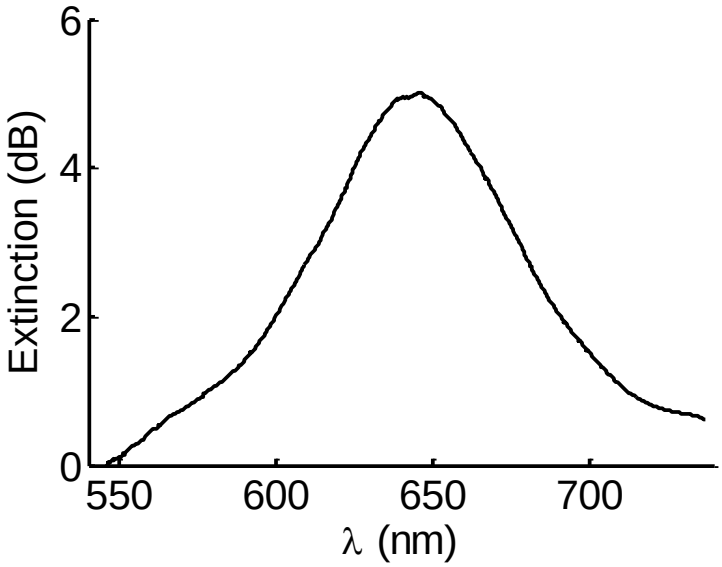


**Figure 108:** The filtered extinction spectrum for a hybrid waveguide structure consisting of a 900 $nm \times 200\ nm$ $Si_3N_4$ waveguide integrated with an array of plasmonic gold nanorods of dimensions $96 \times 57 \times 27\ nm$.

used so that the unwanted features are removed and at the same time, the useful information content of the signal is retained. This method of spectral filtering of the signal is useful, specially when the unwanted features and the desired signal features are well-separated in the spectral domain.

# APPENDIX B

## PERMITTIVITY OF GOLD FOR SIMULATIONS

Nobel metals have strong dispersion in the visible and the near infrared ranges of the spectrum. The optical constant of these metals can be modeled using models such as the Drude model [120]. However, a more accurate way is to use empirical data measured under certain conditions. The measured optical constants of nobel metals have been summarized in a seminal paper by Johnson and Christy [101].

The permittivity of the nobel metals can be calculated from the square of the optical constant and the extinction coefficient as

$$\epsilon = (n - jk)^2. \tag{30}$$

The real part and the imaginary part of the permittivity of gold is plotted in Figure 109 and Figure 110, respectively based on the empirical data presented in [101].

It can be seen that the real part of the permittivity is negative and monotonically decrease as the wavelength increases. The measured data is fitted to a 4th order polynomial, so that

$$\epsilon_r = 9.4 \times 10^{-12}\lambda^4 - 5.4 \times 10^{-8}\lambda^3 + 5.2 \times 10^{-5}\lambda^2 - 0.0794\lambda + 29.96, \tag{31}$$

and

$$\epsilon_i = 2.7 \times 10^{-11}\lambda^4 + 1.29 \times 10^{-7}\lambda^3 - 0.00023\lambda^2 + 0.17\lambda - 47.8. \tag{32}$$

These equations can be used in FEM simulations in a closed form. In each

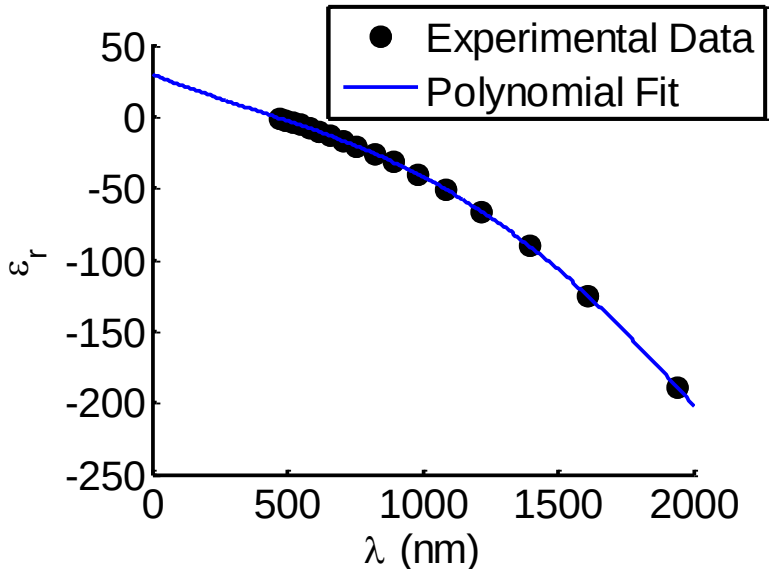


**Figure 109:** The real part of gold permittivity obtained from the empirical data in [101]

.

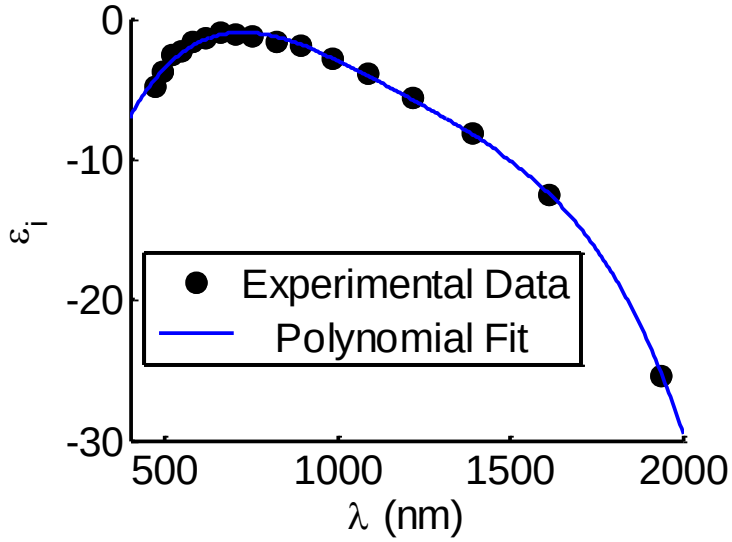


**Figure 110:** The imaginary part of gold permittivity obtained from the empirical data in [101]

.

iteration of solving the structure, the permittivity is evaluated at the appropriate wavelength, and the structure is then solved. This way, the dispersion of gold is considered in the simulations. The results of Johnson and Christy are also used in

the FDTD simulations.

Similar closed form formulae can be extracted for other metals based on the measured optical constants. It should be noted that such closed form formulas are only valid within the range of the measured data.

# APPENDIX C

# SCHOLARLY ACHIEVEMENTS

## Journal Publications:

M. A. Mahmoud; M. Chamanzar, A. Adibi, M. El-Sayed, ”Effect of the Dielectric Constant of the Surrounding Medium and the Substrate on the Surface Plasmon Resonance Spectrum and Sensitivity Factor of Highly Symmetric Systems; Silver Nanocubes,” J. Am. Chem. Soc (JACS) 134, 6434-6442 (2012).

M. Chamanzar and A. Adibi, ”Hybrid Nanoplasmonic-Photonic Resonators for Efficient Coupling of Light to Single Plasmonic Nanoresonators,” Opt. Exp. 19, invited for Focus Issue: Collective Phenomena, 22292-22304 (2011).

Z. Xia, A. A. Eftekhar, M. Soltani, B. Momeni, Q. Li, M. Chamanzar, S. Yegnanarayanan, and A. Adibi, ”High resolution on-chip spectroscopy based on miniaturized microdonut resonators,” Opt. Exp. 19, 12356-12364 (2011).

M. Chamanzar, M. Soltani, B. Momeni, S. Yegnanarayanan, A. Adibi, "Hybrid photonic surface-plasmon-polariton ring resonators for sensing applications," Appl. Phys. B 101, 263-271 (2010).

M. Chamanzar, B. Momeni, and A. Adibi, "Compact on-chip interferometers with high spectral sensitivity," Optics Letters 34, 220 (2009).

B. Momeni, M. Chamanzar, E. Shah Hosseini, M. Askari, M. Soltani, and A. Adibi, "Strong angular dispersion using higher bands of planar silicon photonic crystals," Optics Express 16, 14213 (2008).

M. Chamanzar, S. Yegnanarayanan, Z. Xia, A. Adibi, "Hybrid Integrated Plasmonic-photonic Waveguides for On-chip localized Surface Plasmon Resonance (LSPR) Sensing," Submitted.

Y. Luo, M. Chamanzar and A. Adibi, ”Ultra-compact On-Chip Plasmonic Light Concentrator,” Submitted.

M. Chamanzar, M. A Mahmoud, M. El-Sayed, and A. Adibi, "Combined nanofabrication and chemical synthesis for precise implementation of high quality hollow-core gold nanoparticles," under preparation.

## Selected Conference Papers:

Maysamreza Chamanzar, Zhixuan Xia, Ehsan Shah Hosseini, Siva Yegnanarayanan, and Ali Adibi., "On-chip Localized Surface Plasmon Resonance (LSPR) Sensing using Hybrid Plasmonicphotonic-fluidic Structures," CLEO, San Jose, CA (2012).

Maysamreza Chamanzar, Ehsan Shah Hosseini, Siva Yegnanarayanan, and Ali Adibi, "Efficient coupling to plasmonic nanoresonators using on-chip Silicon Nitride integrated photonic structures," Photonics West, San Francisco, CA, Jan. 22-27, (2011).

Maysamreza Chamanzar, Ehsan Shah Hosseini, Siva Yegnanarayanan, and Ali Adibi, "Integration of plasmonic resonant nanoantennas with on-chip silicon nitride photonic waveguides and microresonators for sensing and spectroscopy," MRS fall meeting, Boston, MA, Nov. 30-Dec. 02, (2010).

Maysamreza Chamanzar, Siva Yegnanarayanan, and Ali Adibi, "Resonanceenhanced efficient excitation of single plasmonic nanoparticles using on-chip microresonators," IEEE LEOS, Denver, CO, Nov. 7-11, (2010).

Maysamreza Chamanzar, Ehsan Shah Hosseini, Siva Yegnanarayanan, and Ali Adibi, "Excitation of Individual Gold Plasmonic Nanoparticles in an Integrated Hybrid Photonic-Plasmonic Platform," Frontiers in Optics, San Jose, CA, Oct. 24-28, (2010).

Maysamreza Chamanzar, Ehsan Shah Hosseini, Siva Yegnanarayanan, and Ali Adibi, "Evanescent Excitation of Plasmonic Nanodisks using Hybrid Guided Wave Silicon Nitride Structures," CLEO/QELS, May 16-21, (2010).

Maysamreza Chamanzar, Mohammad Soltani, Siva Yegnanarayanan, Babak Momeni, and Ali Adibi, "Strong Mode Coupling in Hybrid Plasmonic- Photonic Microresonators using Momentum Matching," Frontiers in Optics 2009/Laser Science XXV.

M. Chamanzar, B. Momeni, A. Adibi, "Compact on-chip interferometers with High

Sensitivity," IPRNA 2008, Boston, MA, 2008.

# Patents:

Plasmonic And Photonic Resonator Structures And Methods For Large Electromagnetic Field Enhancements, US Patent Application # 13/271,737, Oct. (2011).

Photonic Crystal Interferometers, provisional patent submitted (2008).

# REFERENCES


[1] X. Fan, I. White, S. Shopova, H. Zhu, J. Suter, and Y. Sun, "Sensitive optical biosensors for unlabeled targets: a review," Analytica chimica acta **620**, 8–26 (2008).

[2] R. Bukasov and J. Shumaker-Parry, "Silver nanocrescents with infrared plasmonic properties as tunable substrates for surface enhanced infrared absorption spectroscopy," Analytical chemistry **81**, 4531–4535 (2009).

[3] P. Stiles, J. Dieringer, N. Shah, and R. Van Duyne, "Surface-enhanced Raman spectroscopy," Annu. Rev. Anal. Chem. **1**, 601–626 (2008).

[4] J. Lakowicz and B. Masters, "Principles of fluorescence spectroscopy," Journal of Biomedical Optics **13**, 029901 (2008).

[5] C. Ahn, J. Choi, G. Beaucage, J. Nevin, J. Lee, A. Puntambekar, and J. Lee, "Disposable smart lab on a chip for point-of-care clinical diagnostics," Proceedings of the IEEE **92**, 154–173 (2004).

[6] A. Lin, N. Lewinski, J. West, N. Halas, and R. Drezek, "Optically tunable nanoparticle contrast agents for early cancer detection: model-based analysis of gold nanoshells," Journal of Biomedical Optics **10**, 064035 (2005).

[7] P. Dittrich and A. Manz, "Lab-on-a-chip: microfluidics in drug discovery," Nature Reviews Drug Discovery **5**, 210–218 (2006).

[8] S. Lee, J. Lee, J. Seo, I. Jeong, S. Lee, and J. Jung, "Optical sensor based on nanomaterial for the selective detection of toxic metal ions," Advanced Functional Materials **17**, 3441–3446 (2007).

[9] F. Hayes, H. Halsall, and W. Heineman, "Simultaneous immunoassay using electrochemical detection of metal ion labels," Analytical chemistry **66**, 1860–1865 (1994).

[10] J. Butler, "Enzyme-linked immunosorbent assay." Journal of immunoassay **21**, 165 (2000).

[11] J. Vuori, S. Rasi, T. Takala, and K. Vaananen, "Dual-label time-resolved fluoroimmunoassay for simultaneous detection of myoglobin and carbonic anhydrase III in serum," Clinical chemistry **37**, 2087 (1991).

[12] Y. Xu, K. Pettersson, K. Blomberg, I. Hemmila, H. Mikola, and T. Lovgren, "Simultaneous quadruple-label fluorometric immunoassay of thyroid-stimulating hormone, 17 alpha-hydroxyprogesterone, immunoreactive

trypsin, and creatine kinase MM isoenzyme in dried blood spots," Clinical chemistry **38**, 2038 (1992).

[13] C. Brown, K. Higgins, K. Frazer, L. Schoelz, J. Dyminski, V. Marinkovich, S. Miller, and J. Burd, "Simultaneous determination of total IgE and allergen-specific IgE in serum by the MAST chemiluminescent assay system," Clinical chemistry **31**, 1500 (1985).

[14] W. Chan and S. Nie, "Quantum dot bioconjugates for ultrasensitive nonisotopic detection," Science **281**, 2016 (1998).

[15] W. Liang, Y. Huang, Y. Xu, R. Lee, and A. Yariv, "Highly sensitive fiber Bragg grating refractive index sensors," Applied Physics Letters **86**, 151122 (2005).

[16] J. Homola, *Surface plasmon resonance based sensors* (Springer Verlag, 2006).

[17] A. Densmore, D. Xu, P. Waldron, S. Janz, P. Cheben, J. Lapointe, A. Delâge, B. Lamontagne, J. Schmid, and E. Post, "A silicon-on-insulator photonic wire based evanescent field sensor," Photonics Technology Letters, IEEE **18**, 2520–2522 (2006).

[18] R. Philip-Chandy, P. Scully, P. Eldridge, H. Kadim, M. Grapin, M. Jonca, M. D'Ambrosio, and F. Colin, "An optical fiber sensor for biofilm measurement using intensity modulation and image analysis," Selected Topics in Quantum Electronics, IEEE Journal of **6**, 764–772 (2000).

[19] K. De Vos, I. Bartolozzi, E. Schacht, P. Bienstman, and R. Baets, "Silicon-on-Insulator microring resonator for sensitive and label-free biosensing," IEEE J. Sel. Top. Quantum Electron **12**, 134–142 (2006).

[20] A. Armani, R. Kulkarni, S. Fraser, R. Flagan, and K. Vahala, "Label-free, single-molecule detection with optical microcavities," Science **317**, 783 (2007).

[21] E. Chow, A. Grot, L. Mirkarimi, M. Sigalas, and G. Girolami, "Ultracompact biochemical sensor built with two-dimensional photonic crystal microcavity," Optics letters **29**, 1093–1095 (2004).

[22] B. Liedberg, C. Nylander, and I. Lunstrom, "Surface plasmon resonance for gas detection and biosensing," Sensors and Actuators **4**, 299–304 (1983).

[23] R. Harris and J. Wilkinson, "Waveguide surface plasmon resonance sensors," Sensors and Actuators B: Chemical **29**, 261–267 (1995).

[24] R. Slavík, J. Homola *et al.*, "Novel spectral fiber optic sensor based on surface plasmon resonance," Sensors and Actuators B: Chemical **74**, 106–111 (2001).

[25] Z. Qi, I. Honma, and H. Zhou, "Nanoporous leaky waveguide based chemical and biological sensors with broadband spectroscopy," Applied physics letters **90**, 011102 (2007).

[26] X. Qian, X. Peng, D. Ansari, Q. Yin-Goen, G. Chen, D. Shin, L. Yang, A. Young, M. Wang, and S. Nie, "In vivo tumor targeting and spectroscopic detection with surface-enhanced Raman nanoparticle tags," Nature biotechnology **26**, 83–90 (2007).

[27] R. Tripp, R. Dluhy, and Y. Zhao, "Novel nanostructures for SERS biosensing," Nano Today **3**, 31–37 (2008).

[28] I. Chou, M. Benford, H. Beier, G. Coté, M. Wang, N. Jing, J. Kameoka, and T. Good, "Nanofluidic biosensing for $\beta$-amyloid detection using surface enhanced raman spectroscopy," Nano letters **8**, 1729–1735 (2008).

[29] I. El-Sayed, X. Huang, and M. El-Sayed, "Surface plasmon resonance scattering and absorption of anti-EGFR antibody conjugated gold nanoparticles in cancer diagnostics: applications in oral cancer," Nano Letters **5**, 829–834 (2005).

[30] M. Moskovits, "Surface-enhanced spectroscopy," Reviews of Modern Physics **57**, 783 (1985).

[31] K. Nakanishi and P. Solomon, *Infrared absorption spectroscopy*, vol. 89 (Holden-Day San Francisco, 1977).

[32] R. Service, "LABS ON A CHIP: Coming Soon: The Pocket DNA Sequencer," Science **282**, 399–401 (1998).

[33] P. Waggoner and H. Craighead, "Micro-and nanomechanical sensors for environmental, chemical, and biological detection," Lab on a Chip **7**, 1238 (2007).

[34] D. Figeys and D. Pinto, "Lab-on-a-Chip: A Revolution in Biological and Medical Sciences." Analytical Chemistry **72**, 330–335 (2000).

[35] F. Myers and L. Lee, "Innovations in optical microfluidic technologies for point-of-care diagnostics," Lab on a Chip **8**, 2015–2031 (2008).

[36] J. Dostalek, H. Vaisocherova, and J. Homola, "Multichannel surface plasmon resonance biosensor with wavelength division multiplexing," Sensors and Actuators B: Chemical **108**, 758–764 (2005).

[37] R. Ritchie, "Plasma losses by fast electrons in thin films," Physical Review **106**, 874 (1957).

[38] E. Ozbay, "Plasmonics: merging photonics and electronics at nanoscale dimensions," Science **311**, 189 (2006).

[39] R. Zia, J. Schuller, A. Chandran, and M. Brongersma, "Plasmonics: the next chip-scale technology," Materials today **9**, 20–27 (2006).

[40] L. Yin, V. Vlasko-Vlasov, J. Pearson, J. Hiller, J. Hua, U. Welp, D. Brown, and C. Kimball, "Subwavelength focusing and guiding of surface plasmons," Nano letters **5**, 1399–1402 (2005).

[41] G. Veronis and S. Fan, "Modes of subwavelength plasmonic slot waveguides," Journal of Lightwave Technology **25**, 2511–2521 (2007).

[42] S. Bozhevolnyi, V. Volkov, E. Devaux, J. Laluet, and T. Ebbesen, "Channel plasmon subwavelength waveguide components including interferometers and ring resonators," Nature **440**, 508–511 (2006).

[43] T. Holmgaard, Z. Chen, S. Bozhevolnyi, L. Markey, and A. Dereux, "Dielectric-loaded plasmonic waveguide-ring resonators," Optics Express **17**, 2968–2975 (2009).

[44] K. Leosson, T. Nikolajsen, A. Boltasseva, and S. Bozhevolnyi, "Long-range surface plasmon polariton nanowire waveguides for device applications," Optics Express **14**, 314–319 (2006).

[45] K. Kelly, E. Coronado, L. Zhao, and G. Schatz, "The optical properties of metal nanoparticles: the influence of size, shape, and dielectric environment," The Journal of Physical Chemistry B **107**, 668–677 (2003).

[46] S. Eustis and M. El-Sayed, "Why gold nanoparticles are more precious than pretty gold: Noble metal surface plasmon resonance and its enhancement of the radiative and nonradiative properties of nanocrystals of different shapes," Chemical Society Reviews **35**, 209–217 (2006).

[47] S. Nie and S. Emory, "Probing single molecules and single nanoparticles by surface-enhanced Raman scattering," Science **275**, 1102 (1997).

[48] X. Huang, I. El-Sayed, W. Qian, and M. El-Sayed, "Cancer cell imaging and photothermal therapy in the near-infrared region by using gold nanorods," Journal of the American Chemical Society **128**, 2115–2120 (2006).

[49] S. Maier and H. Atwater, "Plasmonics: Localization and guiding of electromagnetic energy in metal/dielectric structures," Journal of Applied Physics **98**, 011101 (2005).

[50] N. Lindquist, P. Nagpal, A. Lesuffleur, D. Norris, and S. Oh, "Three-dimensional plasmonic nanofocusing," Nano letters **10**, 1369–1373 (2010).

[51] N. Rosi and C. Mirkin, "Nanostructures in biodiagnostics," Chemical reviews **105**, 1547–1562 (2005).

[52] D. Marcuse, *Theory of dielectric optical waveguides* (1974).

[53] K. Vahala, "Optical microcavities," Nature **424**, 839–846 (2003).

[54] P. Yeh, *Optical waves in layered media*, vol. 95 (Wiley Online Library, 1988).

[55] B. Momeni, M. Chamanzar, E. Shah Hosseini, M. Askari, M. Soltani, and A. Adibi, "Strong angular dispersion using higher bands of planar silicon photonic crystals," Optics Express **16**, 14213–14220 (2008).

[56] T. Fukazawa, F. Ohno, and T. Baba, "Very compact arrayed-waveguide-grating demultiplexer using Si photonic wire waveguides," Jpn. J. Appl. Phys **43**, 673–675 (2004).

[57] B. Momeni, J. Huang, M. Soltani, M. Askari, S. Mohammadi, M. Rakhshandehroo, and A. Adibi, "Compact wavelength demultiplexing using focusing negative index photonic crystal superprisms," Optics Express **14**, 2413–2422 (2006).

[58] M. Chamanzar, B. Momeni, and A. Adibi, "Compact on-chip interferometers with high spectral sensitivity," Optics letters **34**, 220–222 (2009).

[59] B. Momeni, E. Hosseini, and A. Adibi, "Planar photonic crystal microspectrometers in silicon-nitride for the visible range," Optics Express **17**, 17060–17069 (2009).

[60] E. Shah Hosseini, S. Yegnanarayanan, A. Atabaki, M. Soltani, and A. Adibi, "High quality planar silicon nitride microdisk resonators for integrated photonics in the visible wavelength range," Optics Express **17**, 14543–14551 (2009).

[61] A. Atabaki, B. Momeni, A. Eftekhar, E. Hosseini, S. Yegnanarayanan, and A. Adibi, "Tuning of resonance-spacing in a traveling-wave resonator device," Optics Express **18**, 9447–9455 (2010).

[62] V. Almeida, C. Barrios, R. Panepucci, and M. Lipson, "All-optical control of light on a silicon chip," Nature **431**, 1081–1084 (2004).

[63] I. White, H. Oveys, and X. Fan, "Increasing the Enhancement of SERS with Dielectric Microsphere Resonators," SPECTROSCOPY-SPRINGFIELD THEN EUGENE THEN DULUTH- **21**, 36 (2006).

[64] F. De Angelis, M. Patrini, G. Das, I. Maksymov, M. Galli, L. Businaro, L. Andreani, and E. Di Fabrizio, "A Hybrid Plasmonic- Photonic Nanodevice for Label-Free Detection of a Few Molecules," Nano letters **8**, 2321–2327 (2008).

[65] M. Barth, S. Schietinger, S. Fischer, J. Becker, N. Nusse, T. Aichele, B. Lochel, C. Sonnichsen, and O. Benson, "Nanoassembled plasmonic-photonic hybrid cavity for tailored light-matter coupling," Nano letters **10**, 891–895 (2010).

[66] G. Mie, "Beiträge zur optik trüber medien, speziell kolloidaler metallösungen," Annalen der Physik **330**, 377–445 (1908).

[67] J. Zhao, A. Pinchuk, J. McMahon, S. Li, L. Ausman, A. Atkinson, and G. Schatz, "Methods for describing the electromagnetic properties of silver and gold nanoparticles," Accounts of chemical research **41**, 1710–1720 (2008).

[68] B. Draine and P. Flatau, "Discrete-dipole approximation for scattering calculations," JOSA A **11**, 1491–1499 (1994).

[69] A. Taflove, S. Hagness *et al.*, *Computational electrodynamics: the finite-difference time-domain method*, vol. 347 (Artech House Boston;, 1995).

[70] M. Mahmoud and M. El-Sayed, "Gold nanoframes: Very high surface plasmon fields and excellent near-infrared sensors," Journal of the American Chemical Society (2010).

[71] J. Schuller, E. Barnard, W. Cai, Y. Jun, J. White, and M. Brongersma, "Plasmonics for extreme light concentration and manipulation," Nature materials **9**, 193–204 (2010).

[72] M. Mahmoud, C. Tabor, and M. El-Sayed, "Surface-enhanced raman scattering enhancement by aggregated silver nanocube monolayers assembled by the langmuir- blodgett technique at different surface pressures," The Journal of Physical Chemistry C **113**, 5493–5501 (2009).

[73] C. Raman and K. Krishnan, "A new type of secondary radiation," Nature **121**, 501–502 (1928).

[74] D. Jeanmaire and R. Van Duyne, "Surface raman spectroelectrochemistry: Part i. heterocyclic, aromatic, and aliphatic amines adsorbed on the anodized silver electrode," Journal of Electroanalytical Chemistry and Interfacial Electrochemistry **84**, 1–20 (1977).

[75] P. Aravind, A. Nitzan, and H. Metiu, "The interaction between electromagnetic resonances and its role in spectroscopic studies of molecules adsorbed on colloidal particles or metal spheres," Surface Science **110**, 189–204 (1981).

[76] E. Le Ru, E. Blackie, M. Meyer, and P. Etchegoin, "Surface enhanced raman scattering enhancement factors: a comprehensive study," The Journal of Physical Chemistry C **111**, 13794–13803 (2007).

[77] H. Jung, Y. Park, S. Park, and S. Kim, "Surface enhanced raman scattering from layered assemblies of close-packed gold nanoparticles," analytica chimica acta **602**, 236–243 (2007).

[78] A. Varki, *Essentials of glycobiology* (Cold Spring Harbor Laboratory Pr, 1999).

[79] A. Kulkarni, A. Weiss, and S. Iyer, "Glycan-based high-affinity ligands for toxins and pathogen receptors," Medicinal Research Reviews **30**, 327–393 (2010).

[80] Y. Yu, S. Chang, C. Lee, and C. Wang, "Gold nanorods: electrochemical synthesis and optical properties," The Journal of Physical Chemistry B **101**, 6661–6664 (1997).

[81] Y. Xu, Y. Li, R. Lee, and A. Yariv, "Scattering-theory analysis of waveguide-resonator coupling," Physical Review E **62**, 7389 (2000).

[82] E. Kretschmann and H. Raether, "Radiative decay of non radiative surface plasmons excited by light(Surface plasma waves excitation by light and decay into photons applied to nonradiative modes)," ZEITSCHRIFT FUER NATURFORSCHUNG, TEIL A **23**, 2135 (1968).

[83] A. Otto, "Excitation of nonradiative surface plasma waves in silver by the method of frustrated total reflection," Zeitschrift f
"ur Physik A Hadrons and Nuclei **216**, 398–410 (1968).

[84] J. Jin, J. Jin, and J. Jin, *The finite element method in electromagnetics* (Wiley New York, 1993).

[85] P. Zijlstra, P. Paulo, and M. Orrit, "Optical detection of single non-absorbing molecules using the surface plasmon resonance of a gold nanorod," Nature Nanotechnology **7**, 379–382 (2012).

[86] K. Mayer and J. Hafner, "Localized surface plasmon resonance sensors." Chemical reviews **111**, 3828 (2011).

[87] K. Willets and R. Van Duyne, "Localized surface plasmon resonance spectroscopy and sensing," Annu. Rev. Phys. Chem. **58**, 267–297 (2007).

[88] M. Mahmoud, M. Chamanzar, A. Adibi, and M. El-Sayed, "Effect of the dielectric constant of the surrounding medium and the substrate on the surface plasmon resonance spectrum and sensitivity factors of highly symmetric systems; silver nanocubes," (2012).

[89] J. Anker, W. Hall, O. Lyandres, N. Shah, J. Zhao, and R. Van Duyne, "Biosensing with plasmonic nanosensors," Nature materials **7**, 442–453 (2008).

[90] A. McFarland and R. Van Duyne, "Single silver nanoparticles as real-time optical sensors with zeptomole sensitivity," Nano letters **3**, 1057–1062 (2003).

[91] G. Raschke, S. Kowarik, T. Franzl, C. Sönnichsen, T. Klar, J. Feldmann, A. Nichtl, and K. Kürzinger, "Biomolecular recognition based on single gold nanoparticle light scattering," Nano letters **3**, 935–938 (2003).

[92] S. Stranahan and K. Willets, "Super-resolution optical imaging of single-molecule sers hot spots," Nano letters (2010).

[93] F. Rolland, J. Winderickx, and J. Thevelein, "Glucose-sensing mechanisms in eukaryotic cells," Trends in biochemical sciences **26**, 310–317 (2001).

[94] J. Feng, V. Siu, A. Roelke, V. Mehta, S. Rhieu, G. Palmore, and D. Pacifici, "Nanoscale plasmonic interferometers for multi-spectral, high-throughput biochemical sensing," Nano Letters (2012).

[95] T. Shoji, T. Tsuchizawa, T. Watanabe, K. Yamada, and H. Morita, "Low loss mode size converter from 0.3 $\mu$m square si wire waveguides to singlemode fibres," Electronics Letters **38**, 1669–1670 (2002).

[96] M. Chamanzar and A. Adibi, "Hybrid nanoplasmonic-photonic resonators for efficient coupling of light to single plasmonic nanoresonators," Optics Express **19**, 22292–22304 (2011).

[97] M. Berry, E. Wolf, and N. Bloembergen, *Progress in Optics* (Elsevier Science Ltd, 2007).

[98] P. Deotare, M. McCutcheon, I. Frank, M. Khan, and M. Lončar, "High quality factor photonic crystal nanobeam cavities," Applied Physics Letters **94**, 121106 (2009).

[99] B. Min, E. Ostby, V. Sorger, E. Ulin-Avila, L. Yang, X. Zhang, and K. Vahala, "High-Q surface-plasmon-polariton whispering-gallery microcavity," Nature **457**, 455–458 (2009).

[100] M. Soltani, "Novel integrated silicon nanophotonic structures using ultra-high Q resonators," Ph.D. thesis (2009).

[101] P. Johnson and R. Christy, "Optical constants of the noble metals," Physical Review B **6**, 4370 (1972).

[102] A. Koutsioubas, N. Spiliopoulos, D. Anastassopoulos, A. Vradis, and G. Priftis, "On the implementation of nano-structured materials in surface plasmon resonance sensors," Materials Science and Engineering: B **165**, 270–273 (2009).

[103] A. Koutsioubas, N. Spiliopoulos, D. Anastassopoulos, A. Vradis, and G. Priftis, "Nanoporous alumina enhanced surface plasmon resonance sensors," Journal of Applied Physics **103**, 094521 (2008).

[104] F. Ligler, *Optical biosensors: today and tomorrow* (Elsevier Science, 2008).

[105] J. Spanier and I. Herman, "Use of hybrid phenomenological and statistical effective-medium theories of dielectric functions to model the infrared reflectance of porous SiC films," Physical Review B **61**, 10437 (2000).

[106] A. Yariv, "Universal relations for coupling of optical power between microresonators and dielectric waveguides," Electronics Letters **36**, 321–322 (2000).

[107] M. Chamanzar, M. Soltani, B. Momeni, S. Yegnanarayanan, and A. Adibi, "Hybrid photonic surface-plasmon-polariton ring resonators for sensing applications," Applied Physics B: Lasers and Optics pp. 1–9 (2010).

[108] I. White and X. Fan, "On the performance quantification of resonant refractive index sensors," IEEE J. Sel. Top. Quantum Electron **12**, 134–142 (2006).

[109] L. Sherry, R. Jin, C. Mirkin, G. Schatz, and R. Van Duyne, "Localized surface plasmon resonance spectroscopy of single silver triangular nanoprisms," Nano letters **6**, 2060–2065 (2006).

[110] T. Squires, R. Messinger, and S. Manalis, "Making it stick: convection, reaction and diffusion in surface-based biosensors," Nature biotechnology **26**, 417–426 (2008).

[111] E. Krioukov, D. Klunder, A. Driessen, J. Greve, and C. Otto, "Integrated optical microcavities for enhanced evanescent-wave spectroscopy," Optics letters **27**, 1504–1506 (2002).

[112] A. Yalcin, K. Popat, J. Aldridge, T. Desai, J. Hryniewicz, N. Chbouki, B. Little, O. King, V. Van, S. Chu *et al.*, "Optical sensing of biomolecules using microring resonators," Selected Topics in Quantum Electronics, IEEE Journal of **12**, 148–155 (2006).

[113] F. Vollmer and S. Arnold, "Whispering-gallery-mode biosensing: label-free detection down to single molecules," Nature Methods **5**, 591–596 (2008).

[114] J. Anderson, D. Chiu, H. Wu, O. Schueller, and G. Whitesides, "Fabrication of microfluidic systems in poly (dimethylsiloxane)," Electrophoresis **21**, 27–40 (2000).

[115] S. Bhattacharya, A. Datta, J. Berg, and S. Gangopadhyay, "Studies on surface wettability of poly (dimethyl) siloxane (pdms) and glass under oxygen-plasma treatment and correlation with bond strength," Microelectromechanical Systems, Journal of **14**, 590–597 (2005).

[116] Z. Zhang, P. Zhao, G. Xiao, B. Watts, and C. Xu, "Sealing su-8 microfluidic channels using pdms," Biomicrofluidics **5**, 046503 (2011).

[117] Z. Zhang, P. Zhao, and G. Xiao, "The fabrication of polymer microfluidic devices using a solid-to-solid interfacial polyaddition," Polymer **50**, 5358–5361 (2009).

[118] M. Stockman, "Nanofocusing of optical energy in tapered plasmonic waveguides," Physical review letters **93**, 137404 (2004).

[119] Y. Luo, M. Chamanzar, and A. Adibi, "Ultra-compact on-chip plasmonic light concentrator," Arxiv preprint arXiv:1204.3975 (2012).

[120] P. Drude, "Zur elektronentheorie der metalle," Annalen der Physik **306**, 566–613 (1900).

# VITA

Maysamreza Chamanzar was born in Tehran, Iran. He received his B.Sc. from Tehran Polytechnique (AmirKabir University) and M.Sc. from the Sharif University in Electrical Engineering in 2003 and 2005, respectively. He also received a Masters from Georgia Tech in Microelectronics in 2008. His current research interests are the applications of optics, plasmonics, and nanotechnology to biology and chemical analysis. When he is not working in the lab, Mr. Chamanzar enjoys reading, running, and taking care of his plants.